SLAC-R-578
UC-414

B Decay Charm Counting Via Topological Vertexing*

Aaron S. Chou

Stanford Linear Accelerator Center
Stanford University
Stanford, CA 94309

SLAC-Report-578
October 2001

Prepared for the Department of Energy
under contract number DE-AC03-76SF00515

Printed in the United States of America. Available from the National Technical Information Service, U.S. Department of Commerce, 5285 Port Royal Road, Springfield, VA 22161.

*Ph.D. thesis, Stanford University, Stanford, CA 94309.

Abstract

We present a new and unique measurement of the branching fractions of b hadrons to states with 0, 1, and 2 open charm hadrons, using a sample of 350,000 hadronic Z^0 decays collected during the SLD/SLC 97-98 run. The method takes advantage of the excellent vertexing resolution of the VXD3, a pixel-based CCD vertex detector, which allows the separation of B and cascade D decay vertices. A fit of the vertex count and the decay length distributions to distribution shapes predicted by Monte Carlo simulation allows the extraction of the inclusive branching fractions. We measure:

$$BR(B \to (0D)X) = (3.7 \pm 1.1(\text{stat}) \pm 2.1(\text{syst}))\% \quad (1)$$

$$BR(B \to (2D)X) = (17.9 \pm 1.4(\text{stat}) \pm 3.3(\text{syst}))\% \quad (2)$$

where B and D represent mixtures of open b and open c hadrons. The corresponding charm count, $N_c = 1.188 \pm 0.010 \pm 0.040 \pm 0.006$ is consistent with previous measurement averages but slightly closer to theoretical expectations.

Preface

This work is the culmination of many long years of work. It would not have been possible without the large contributions of many people. First to be recognized should be my adviser Marty Breidenbach, who has ably led the SLD collaboration through both good times and tough times. Despite his often busy schedule, Marty always has had time to discuss anything which happened to be troubling me, and his often insightful advice has been invaluable.

I would also like to profusely thank John Jaros for the many productive brainstorming sessions we had in his office. Without his keen intuition (and patience), I would no doubt still be trying to make the data analysis work, instead of writing this preface! I have learned much from John, and for that I will always be grateful.

Many thanks also to Su Dong, who has always been one of the major players in SLD. His contributions to the experiment are numerous, and include not only detector alignment, MC detector modelling, and data analysis, but also miraculously locating the broken drift chamber wire when the rest of us had all but given up. As the local heavy flavor physics guru, Su Dong's comments have always been useful, and well-received.

Thanks to the professors who generously agreed to be on my reading committee. I could always count on Helmut Wiedemann to offer kind advice, and I have learned much from taking JoAnne Hewett's class on collider physics. Other professors to whom I am indebted include Renata Kallosh, for showing me what wonders may lie just beyond the experimental horizon; and Steve Kerckhoff, for training me to think logically and consistently.

The group of SLD people I would like to acknowledge is too big to list here, but special thanks go to my office-mate Danning Dong, for many useful discussions both personal and work-related; to Tom Wright, for showing me how to do things correctly and for being a endless fount of knowledge; to Tom Junk and Homer Neal, for inspiration; and to Peter Kim, who while technically not a SLD person, did help me immensely in tuning the CLEO B decay model. To these people and to the others: thank you for making SLAC a nice place to work.

And I would most like to thank my parents, Hsin-hsin and Julia Chou for always believing in me, and my wife Hyejoo Kang for her constant support.

This document is loosely organized as follows. First, in chapter 1, the idea of charm counting is motivated from theoretical considerations and an experimental plan of attack is then drawn up. In chapters 2, 3, and 5, an discussion of the SLC collider and SLD detector shows how the experimental facilities are uniquely suited for the desired measurement. The reconstruction of the B decay vertex topology is the subject of chapters 4, 6, and 7. The analysis procedure is explained in detail and the results of the measurement are presented in chapter 8. Systematic uncertainties are discussed in chapter 9. Several appendices give more necessary details.

Experimental particle physics is a hugely collaborative effort, involving hundreds of workers. It is often difficult to isolate the contributions of any individual worker, but when possible, acknowledgements are made in the text. The results presented in this thesis on which the author worked (often collaboratively) include: drift chamber pattern recognition, beam position measurement, vertex detector alignment, vertex

detector simulation, Monte Carlo B decay modelling, and of course the analysis being presented.

Several conventions are used throughout. Distances are measured in centimeters unless otherwise specified. Cylindrical coordinate systems are often used in which the z direction is sometimes the beam direction for the barrel detector coordinate system, and sometimes a particle flight direction. The transverse and longitudinal directions are defined with respect to these cylindrical coordinates. The letters θ and ϕ are reserved to describe the polar and azimuthal angles in the detector coordinate system. The letter λ denotes the polar angle measured instead from the transverse plane. The hadron names B and D refer to any b-type or c-type hadron with weak interaction scale lifetimes, including baryons. Λ_b and Λ_c refer to b and c baryons in general and $(c\bar{c})$ refer to all charmonia resonances. Abbreviations include MC for Monte Carlo simulation, IP for interaction point, POCA for point of closest approach, and DOCA for distance of closest approach. For perturbative theoretical calculations, LO, NLO, and NNLO are shorthand for leading-order, next-to-leading-order, and next-to-next-to-leading-order.

Contents

Chapter 1

Theoretical Motivation

The problem at hand concerns a long standing discrepancy between the measured values of the B semileptonic decay branching ratio BR_{SL} and the naive theoretical expectation.[1] In a semileptonic decay (see figure 1.3), the B hadron decays via a virtual $W^{\pm}$ emission, and the $W^{\pm}$ produces a lepton and a neutrino. The branching ratio may be defined as the ratio of the partial width $\Gamma_{SL} \equiv \Gamma(B \to e\ \bar{\nu}_e\ X)$ to the total decay width Γ_{tot}.

$$\begin{aligned} BR_{SL} &= \frac{\Gamma_{SL}}{\Gamma_{tot}} \\ &= \frac{\Gamma_{SL}}{2.22\ \Gamma_{SL} + \Gamma_{had}} \\ &= \frac{1}{2.22 + r_{had}} \end{aligned} \tag{1.1}$$

[1] Background information about the Standard Model and uncertainties in heavy quark calculations may be found in appendix A.

where $\Gamma_{had} = \Gamma_{\bar{u}d} + \Gamma_{\bar{c}s} + \Gamma_{rare}$ is the hadronic width and the ratios of hadronic rates to semileptonic rates may be defined as:

$$r_{had} \equiv \Gamma_{had}/\Gamma_{SL} = r_{\bar{u}d} + r_{\bar{c}s} + r_{rare}. \tag{1.2}$$

$\bar{u}d$, $\bar{c}s$ refer to the quarks produced by the mediating W^- and 'rare' refers to all other hadronic processes.[2] Examples of contributing processes are shown in figure 1.3(right) for $\Gamma_{\bar{u}d}$, figures 1.5, 1.6, and 1.7 for $\Gamma_{\bar{c}s}$, and figure 1.4 for Γ_{rare}.

The leptons in the total semileptonic rate come from decays of the mediating $W^{\pm}$. The factor of 2.22 comes from a contribution of 1 from $W \to e\ \nu_e$, 1 from $W \to \mu\ \nu_\mu$, and 0.22 from the phase-space suppressed $W \to \tau\nu_\tau$ [1].

Naively, since there are 3 colors for each quark, one would expect $r_{\bar{u}d} \sim 3$. Assuming $r_{\bar{c}s}$ is phase space suppressed by a factor of $\sim$ 5-10 [2] and

$$r_{rare} \approx 0.25 \pm 0.10 \text{ [3]}, \tag{1.3}$$

BR_{SL} is expected to be $1/(2.22 + r_{\bar{u}d} + r_{\bar{c}s} + r_{rare}) \approx (15 \pm 1)\%$ at the parton level [4]. This expectation is much larger than the measured values of 0.1049 ± 0.0046 from CLEO [5] for a low energy mixture of B_u and B_d mesons, and 0.1056 ± 0.0021 from LEP [6] for the mixture of B hadrons ($\sim$ 40% B_u, 40% B_d, 10% B_s, 10% b baryons) produced in Z^0 decays.

[2]There is some sloppiness in these definitions due to contributions to the decay widths from fully leptonic decays $B \to l\ \bar{\nu}_l$ and semileptonic rare decays like $b \to u\ l\ \bar{\nu}_l$. These processes are assumed to be sufficiently rare that, for the argument presented in this section, their effects can be safely ignored. Production of CKM suppressed quark/antiquark combinations by the W is also assumed to be negligible.

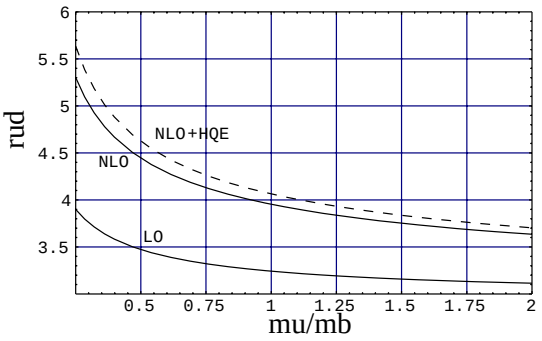

Figure 1.1: LO, NLO, and NLO + non-perturbative calculations of $r_{\bar{u}d} \equiv \Gamma_{\bar{u}d}/\Gamma_{SL}$ for different values of the renormalization scale μ/m_b. A value of $m_b = 4.5$ GeV is used.

Calculation of the semileptonic rate Γ_{SL} is fairly straightforward since the only QCD contributions involve the spectator quark and are thus suppressed by powers of Λ_{QCD}/m_b. The spectator corrections have been estimated to give $\Delta BR_{SL} < 0.01$ at tree level [4] [7]. Since Γ_{SL} is more or less fixed, reduction of the predicted semileptonic branching ratio can only be accomplished by increasing the partial width from non-semileptonic decays, thus increasing the total B width.

It was recognized early on that NLO corrections could enhance the hadronic rate and reduce the parton level prediction for BR_{SL}. Indeed, a NLO calculation [8] [9] shown in figure 1.1 gives an increased $r_{\bar{u}d} = 4.0 \pm 0.4$. Recent NLO calculations [8] also increase the rate $\Gamma_{\bar{c}s}$ by about 30%, thus accomodating values of BR_{SL} as low as $\sim 12\%$.

However, charm counting measurements restrict further enhancements of Γ_{cs}, since

increasing $r_{\bar{c}s}$ also increases N_c, the average number of charm quarks per B decay:

$$\begin{aligned} N_c &= 1 + BR_{\bar{c}s} - BR_{rare} \\ &= 1 + \frac{r_{\bar{c}s} - r_{rare}}{2.22 + r_{had}}. \end{aligned} \tag{1.4}$$

The current experimental averages[3] for N_c are 1.130 ± 0.061 (CLEO) and 1.156 ± 0.039 (LEP) whereas the naive theoretical prediction based on the measured BR_{SL}, $N_c = 1.30 \pm 0.06$ [10] is already too high.

Although these measurements have employed a variety of techniques including direct charm counting via exclusive reconstruction of D mesons and of various charmonia species, counting of 'wrong-sign' D's in flavor-tagged B decays, and fits to impact parameter distributions, their results are expected to have fairly correlated errors. For example, measurements based on exclusive D reconstruction have common systematic uncertainties coming from the uncertainty in the branching fraction to the decay mode used. The necessity of supplementing the D count with a charmonia branching ratio of $BR_{(c\bar{c})} \approx 0.023 \pm 0.003$ estimated from measurements and theoretical calculations [11] yields another explicit correlation. Despite the correlations, individual measurements used in the averages are not all consistent with one another, and so the experimental picture is not completely clear. The measurements of N_c are discussed further in chapter 10.

An enhanced rare B decay rate is another possible solution. Equations 1.4 and

[3]These averages are taken from reference [10] and updated with the new estimates for $\Sigma_c^{0,+}$ and charmonium production given in reference [11]. The wrong-sign D measurements are not used for reasons discussed in chapter 10.

1.1 may be used to eliminate $r_{\bar{c}s}$ to get:

$$N_c = 2 - (2.22 + r_{\bar{u}d} + 2 \cdot r_{rare}) \cdot BR_{SL}. \tag{1.5}$$

Alternatively, equation 1.4 can be written as:

$$N_c = 1 + (r_{\bar{c}s} - r_{rare}) \cdot BR_{SL}. \tag{1.6}$$

In either case, r_{rare} must be increased in order to bring the theoretical predictions simultaneously into agreement with the measured values of both N_c and BR_{SL}. In the standard model, rare decays are dominated by $b \to u$ and $b \to sg$ processes. Possible enhancements of the $b \to sg$ rate due to 'penguin' diagrams have been investigated by Kagan [12]. On the experimental front many exclusive modes have been seen or measured, but measurements of the inclusive rate are still elusive and potentially very interesting. A determination of the CKM matrix element V_{ub} may be extracted from a measurement of $b \to u\ l\ \nu$, for example. A recent measurement by DELPHI [13] based on impact parameter distributions gives $BR_{rare} = 0.007 \pm 0.021$, consistent with the theoretical expectation given in equation 1.3. Other measurements are discussed in [14]. No surprises have yet been found.

A more modern theoretical calculation which more easily accomodates the measured values of BR_{SL} and N_c is presented by Neubert and Sachrajda [7]. Their results, along with the experimental values[4], are shown in figure 1.2. The new theoretical pre-

[4]To make a fair comparison of Γ_{SL}, the LEP measurement of BR_{SL} has been multiplied by a factor of $1/2 \cdot (\tau_{B^0} + \tau_{B^\pm})/\tau_b = 1.023 \pm 0.021$ in order to account for the differences in average total decay widths between the mixture of b hadrons at the $\Upsilon(4s)$ and at the Z^0. τ_b represents the

diction depends on the renormalization scale μ and on the mass ratio m_c/m_b. Since the strong force is asymptotically free, decreasing μ causes α_s to increase. This increase effectively scales up the NLO perturbative matrix elements for multi-hadronic processes, resulting in a larger non-semileptonic width. Since the single and double charm pure hadronic processes are scaled up by similar amounts, N_c is only modestly affected. The dependence of the plot on m_c/m_b is just a phase space effect. Increasing the charm quark mass relative to the bottom quark mass reduces the amount of available phase space to produce charm, and lowers N_c. The total decay width is then reduced causing BR_{SL} to become larger. The allowed values of m_c/m_b are constrained by heavy quark spectroscopy. Agreement with the data is achieved only by picking a large value for m_c to match the charm count and going to very low renormalization scales $\mu/m_b \approx 0.25$ to match the semileptonic branching fraction.

In addition to the purely theoretical motivation of testing the consistency of the B hadron decay model, another practical motivation for charm counting is to reduce systematic uncertainties in other heavy flavor analyses. For example, the sensitivity of B mixing measurements scales linearly with the purity of the final state tag. This tag, which determines whether the meson decays as a B or a $\bar{B}$, is often performed using charge information from both the B vertex and the cascade D vertex or vertices. A decay producing two charmed hadrons will produce both a D and a $\bar{D}$. The extra 'wrong sign' charmed hadron dilutes the information that may be obtained from the tag. The amount of this dilution can only be correctly modelled by using data from

average lifetime of b hadrons produced at the Z^0. The world averages (SLD+CDF+LEP) [11] for the lifetimes are used.

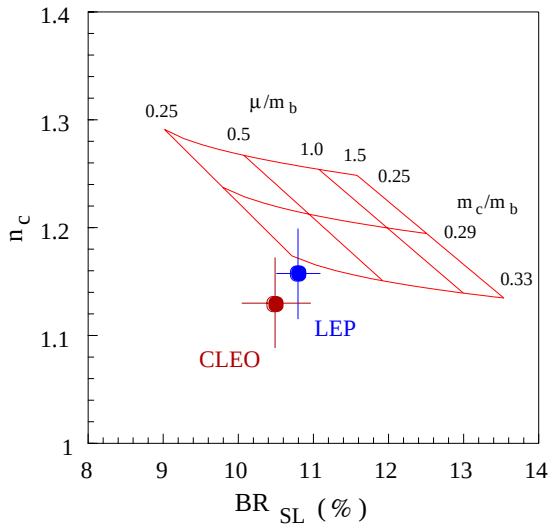

Figure 1.2: Measurements of the B semileptonic branching fraction and N_c by LEP and CLEO compared with theoretical expectations.

charm counting measurements.

1.1 A topological classification

The present analysis extracts N_c by exploiting the rough correspondence between the charm count and the B decay vertex topology. B decays can be categorized as $0D$, $1D$, and $2D$, where 'D' refers to an 'open charm' hadron, (any charmed hadron with an weak interaction scale lifetime such as D^0, $D^{\pm}$, D_s or the various charmed baryons). At typical Z^0 decay energies, weakly decaying heavy flavor hadrons typically decay within a couple of milllimeters of their production point, well within the the tracking chambers. The tracks formed by the charged daughter particles may then be intersected to reconstruct the position of the decay. Apart from the primary

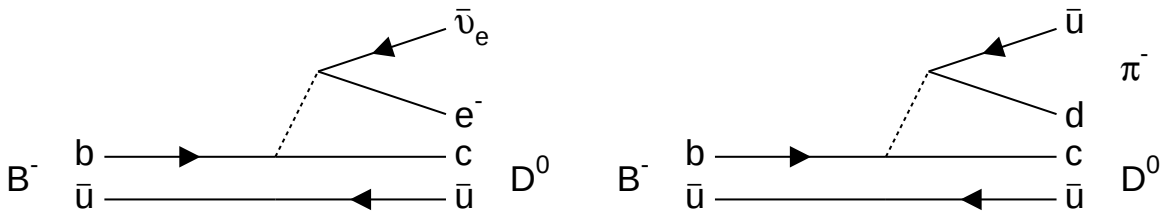

Figure 1.3: Single-charm processes producing only one open charm hadron. Left: a semileptonic decay. Right: a purely hadronic decay.

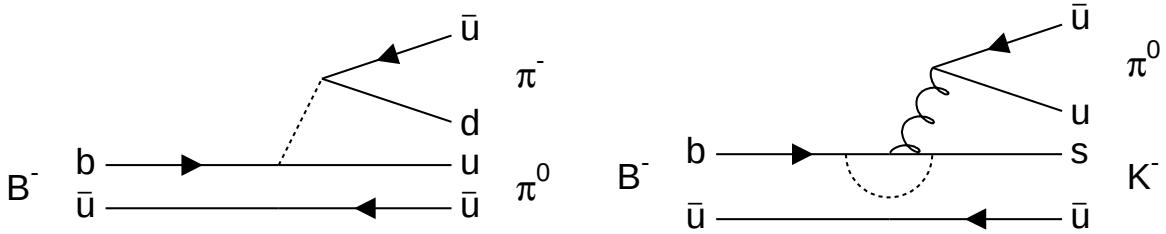

Figure 1.4: Rare B decay processes with no charm produced.

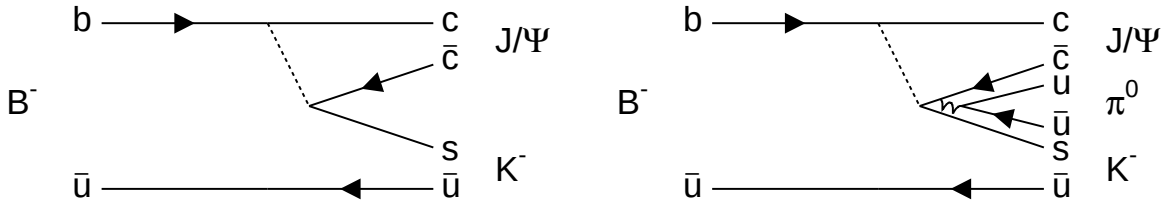

Figure 1.5: Double-charm processes producing charmonium.

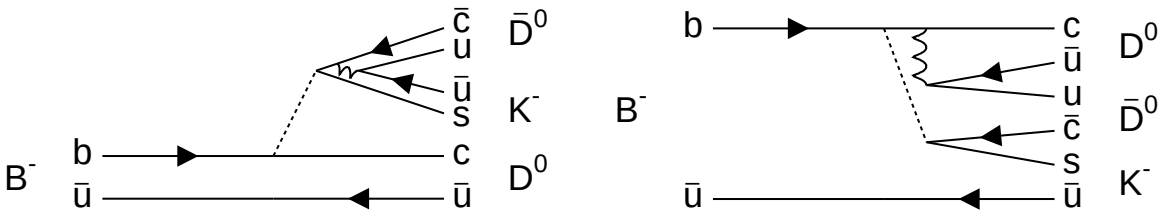

Figure 1.6: Primary and color suppressed double-open-charm producing processes.

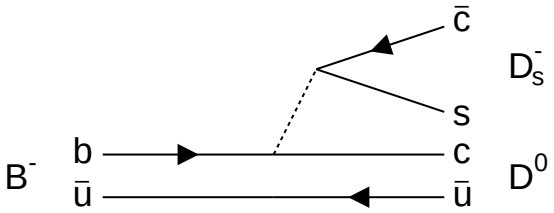

Figure 1.7: Double-open-charm process producing D_s.

Z^0 decay position which defines an origin of coordinates, such vertices are usually only formed at the positions of B and D hadron decays. B and D here refer to any weakly decaying b or c hadrons. The much shorter lifetimes typical of strong or electromagnetic decays are not resolvable by a finite resolution tracking chamber, and the much longer lifetimes in weak decays of lighter hadrons render these particles effectively stable at the millimeter scale. Therefore, it is useful to categorize decays based on the number of true D-type vertices, [n]D which are produced in addition to the B vertex.

The $0D$ category includes B's decaying to charmonia resonances as well as the rare decay processes $b \to u$, $b \to s\ \gamma$, $b \to s\ g$, etc. Examples of these processes

are shown in figures 1.5 and 1.4.[5] Charmonia ($c\bar{c}$) resonances are considered to be 'hidden charm' because these $c\bar{c}$ bound states decay much more quickly via strong or electromagnetic annihilation processes than the weakly decay 'open charm' D's and so separate hidden charm vertices are not resolvable from the B vertex. Since none of the other particles involved in any of these decay types have weak scale lifetimes, $0D$ decays are characterized by having only a single millimeter scale B decay vertex. The $0D$ branching ratio may be written as:

$$BR_{0D} = BR_{rare} + BR_{(c\bar{c})} \tag{1.7}$$

BR_{0D} is expected to be relatively small because it is composed of these CKM suppressed, loop suppressed, and/or color suppressed processes.

The $1D$ category has the largest branching fraction and it includes most of the semileptonic decays. The D is produced in the typical $b \to c$ transition while the mediating W produces only $l\bar{\nu}_l$ or $\bar{u}d$. Examples are shown in figure 1.3. These decays typically have two secondary vertices, one from the B and one from the D, and this property may be used to distinguish these decays from the $0D$ category. Low charged track multiplicities and short decay lengths may sometimes complicate the observability of these vertices however. The $1D$ branching ratio may be written as:

$$BR_{1D} = BR_{SL} + BR_{\bar{u}d} \tag{1.8}$$

[5]The diagrams shown in this section are all for B^- decays with a $\bar{u}$ spectator quark. Assuming local quark-hadron duality, the b quark decay is largely independent of the spectator quark(s) and so analogous diagrams may be drawn for all B hadron species.

BR_{1D} is expected to be the largest branching ratio because it contains many non-suppressed processes and a larger available kinematic phase space in the W decay.

The $2D$ category contains decays with two open charm hadrons, one of which comes from $W \to \bar{c}s$. Examples of processes leading to a double-open-charm final state are shown in figures 1.6 and 1.7. The $2D$ branching ratio may be written as:

$$BR_{2D} = BR_{\bar{c}s} - BR_{(c\bar{c})}. \tag{1.9}$$

BR_{2D} is expected to be smaller than BR_{1D} because of phase space suppression due to the large mass of the extra D meson. Measurements of inclusive and exclusive rates for these decays by CLEO and LEP are included in the N_c averages shown in figure 1.2.

The $2D$ decays are the hardest to measure using vertexing techniques. Low charged particle multiplicity problems are compounded by having two D's in the decay. Often, because the average charged particle multiplicity from D's is low and few charged particles are expected from the B vertex, one or more of the vertices will yield no charged particles. It can be estimated based on measured exclusive decays modes that all three vertices are potentially visible in only about 50% of the decays.

1.2 A Monte Carlo study of decay topology

The topological classification above is only useful if the decay vertices can actually be resolved by the detector. In this section, the required detector resolution is estimated

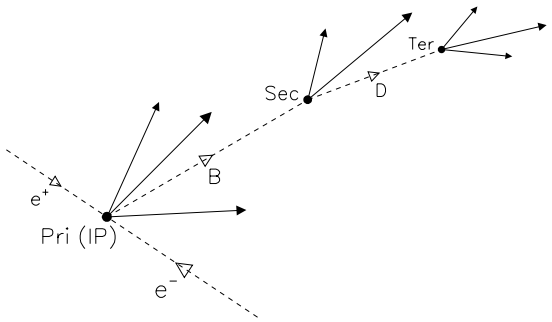

Figure 1.8: $1D$ decay topology with a primary Z^0 decay vertex at the interaction point (IP), a secondary B decay vertex, and a tertiary D decay vertex.

using MC studies.

In $0D$ decays, only the B vertex is produced with a millimeter scale decay length. The charmonia decay 'instantly' through strong and electromagnetic interactions and so their decay points coincide with the B decay point within the detector resolution. Non-heavy decay vertices such as K_s, Λ, and gamma conversion vertices occur at the centimeter scale and may be removed using cuts on vertex distance, mass, charge, and opening angle. The only remaining millimeter scale vertex is therefore the B decay vertex which is on average about 3 mm away from the IP for typical B boosts in Z^0 decays. This decay length distribution and the distributions described below are shown in figure 1.9. It is worth noting that although $Z^0 \to c\bar{c}$ decays have a similar topology, they can most often be rejected based on kinematic considerations used in a B-tag (see chapter 7). In the charm events which mistakenly get tagged as B events, vertex finding is suppressed by the low D decay multiplicity and the shorter average decay length $\sim$1.5 mm.

In $1D$ decays, there is an additional D decay point on average 1 mm away from

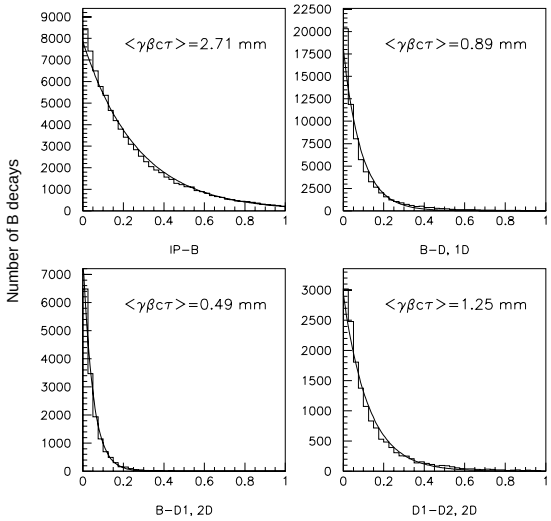

Figure 1.9: MC predicted true vertex separations (cm) averaged over B and D types in the standard SLD MC. Also shown is the exponential fit to each distribution.

the B decay point. The decay topology is shown in figure 1.8. The scale is primarily set again by the B boost distribution but is also affected by the D boost distribution in $B \rightarrow D$ decays. Also, although the various charm hadron species have widely varying lifetimes as can be seen from figure 1.10, recent measurements by CLEO have shown that charm production in B meson decays is dominated by production of neutral D^0's: $BR(B \rightarrow (D^0 \text{ or } \bar{D}^0)X) = 0.636 \pm 0.030$, $BR(B \rightarrow D^{\pm}X) = 0.235 \pm 0.027$ [15]. Furthermore, D_s mesons produced in B decays are expected to have a similar decay length as D^0 mesons due to their similar lifetimes. Therefore small variations in the assumed charm species fractions do not drastically change the prediction of the average decay length. $1D$ decays may be distinguished from $0D$ decays by the detection of an additional vertex.

In $2D$ decays, there are two D decay points. Since the lab frame kinematics are

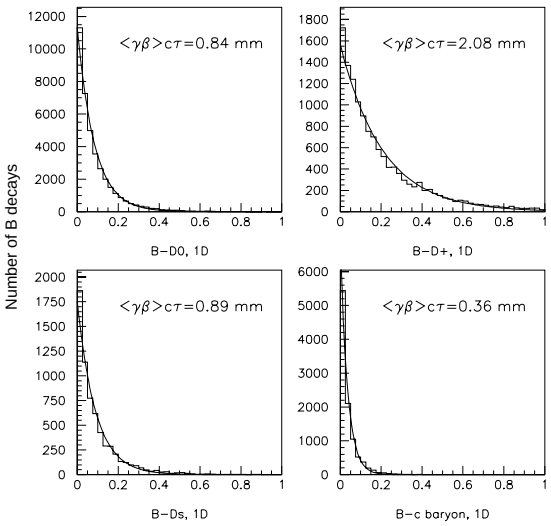

Figure 1.10: MC predicted true vertex separations for various D types in $1D$ decays, averaged over B types. Also shown is the exponential fit to each distribution.

dominated by the B boost, each of these vertices is again on average 1 mm away from the B decay, just as in the $1D$ case. However, if we do not distinguish between the two D vertices, then for any given proper time, there are two chances for a D to decay. The effective lifetime for the first D to decay is therefore halved. Since the lifetime distribution is an exponential, the remaining undecayed D then decays approximately one lifetime later. So, the average B-D separations are actually 1/2 and 3/2 times the typical D decay length. These separation scales, shown in the lower two plots in figure 1.9, are modified somewhat by the differences in lifetimes between the various D species and the differences in their boost spectra. The modelling of the $2D$ decays is described in appendix B.

These MC studies indicate that the 0.5-1.0 mm scale separation of b and D vertices is the critical scale which must be resolvable in order to give a sufficiently high

efficiency to separate and count vertices. The tracking resolution of the SLD and the resulting vertexing resolution are discussed in chapters 2 and 5, respectively. The effective 3 σ vertexing resolution is shown to be about 0.5 mm which is sufficient to resolve a good fraction of the vertices in the decay chain.

1.3 The Goal

Simply stated, the goal of the analysis is to measure the inclusive branching fractions $BR(B \to (0D)X)$ and $BR(B \to (2D)X)$ and therefore also determine

$$BR(B \to (1D)X) = 1 - BR(B \to (0D)X) - BR(B \to (2D)X). \tag{1.10}$$

The basic method is to fit the measured vertex count and vertex separation distributions to a set of distributions predicted by the MC for each of the $BR_{[n]D}$ topologies as well as for the *udsc* background. From these measurements, the average number of charm particles per B decay may be computed using:

$$\begin{aligned} n_c &= 1 \times BR_{1D} + 2 \times BR_{2D} + 2 \times BR_{(c\bar{c})} \\ &= 1 - BR_{0D} + BR_{2D} + 2 \times BR_{(c\bar{c})} \end{aligned} \tag{1.11}$$

where $BR_{(c\bar{c})}$ is the subset of BR_{0D} containing hidden charm in the form of charmonium resonances. ($BR_{(c\bar{c})}$ must be obtained from other independent measurements).

The rare decay branching fraction may then be obtained from:

$$BR_{rare} = BR_{0D} - BR_{(c\bar{c})}. \tag{1.12}$$

Chapter 2

The Experimental Apparatus

2.1 The SLC

In this analysis we used a sample of approximately ∼62,000 tagged B or $\bar{B}$ decays which were obtained from the decays of a sample of ∼350,000 Z^0 particles created by the SLAC Linear Collider (SLC) in its 1997-8 run. The SLC, depicted in figure 2.1, is a 2 mile long linear accelerator which accelerates electrons and positrons to energies of 45.6 GeV before colliding them at a 120 Hz rate to produce particles at the Z^0 pole. Details about the machine may be found in [16].

High luminosities are only achievable at e^+e^- linear colliders by using focussing optics to compress the beams in order to create a very small high particle density interaction region (IR). The SLC IR measures 1 μm × 2 μm in the directions transverse to the beams, and approximately 200 μm in the longitudinal direction. The beam spot is very stable by design since any instabilities would easily cause the two beams

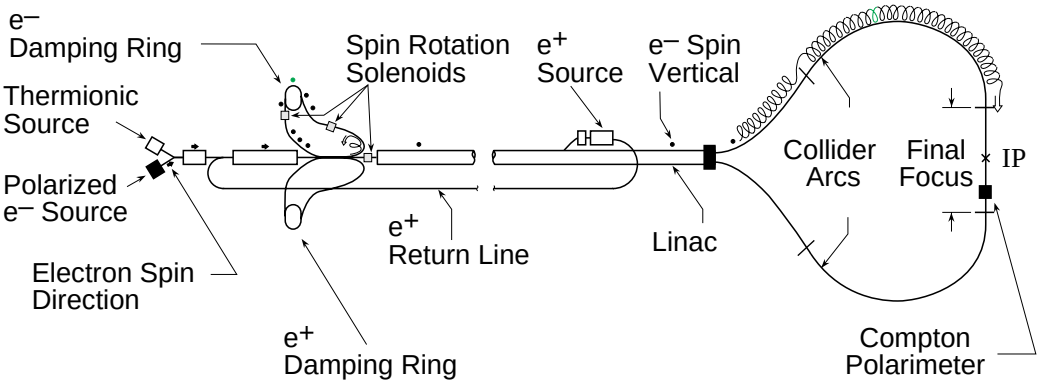

Figure 2.1: The SLC.

to miss each other. The stability of the beam spot allows its position to be measured to very high accuracy as will be described in chapter 4. This precise determination of the primary interaction point (IP) where the Z^0 is created and instantaneously decays allows a very efficient and pure heavy flavor tag based on finding secondary heavy hadron decay vertices displaced from the IP. This tag will be discussed in chapter 7.

2.2 The SLD

The particles created in the Z^0 decay are measured with the SLC Large Detector (SLD), pictures of which are shown in figures 2.2 and 2.3. The components of the detector are arranged in cylindrical barrels centered on the e^+e^- beam axis, and so a standard cylindrical coordinate system will be used throughout this chapter. The components most relevant to the present analysis include a inner tracking chamber called the VXD3 [17] for measuring particle trajectory positions and directions, an outer central drift chamber (CDC) [18] [19] and 0.6 T magnetic field for measuring

particle momenta, several liquid argon calorimeter sections (49 X_0, 2.8 λ_I) [20] for electron identification and thrust axis determination, and an instrumented flux return/muon detector, the warm iron calorimeter [21]. The tracking chambers will be described below, and details about the other individual detector components may be found in the references given above.

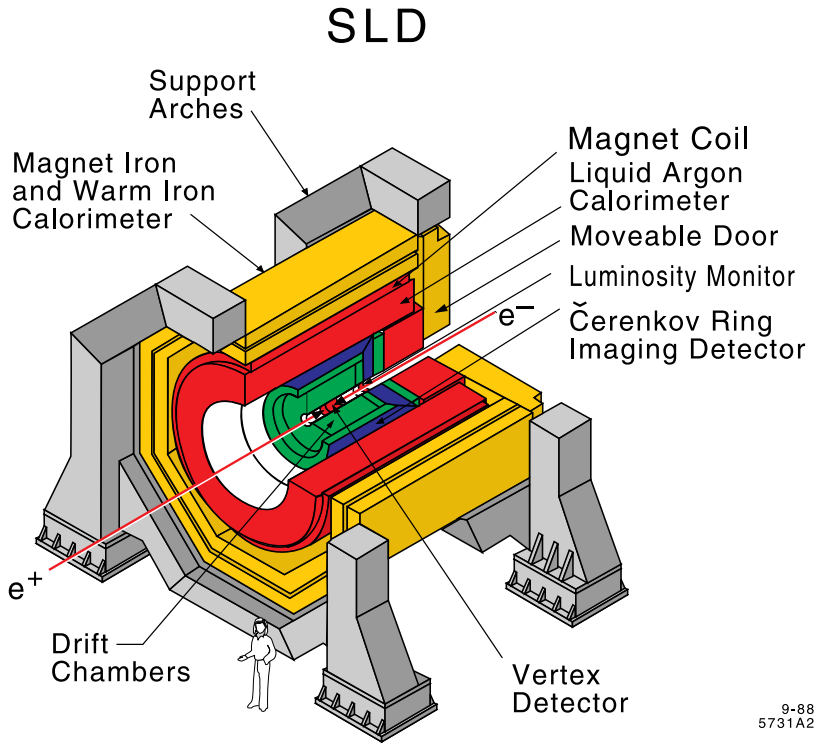

Figure 2.2: The SLD.

2.3 The Vertex Detector

The VXD3 is a detector that uses silicon charge coupled devices (CCDs) to make extremely precise position measurements of particle trajectories. The reconstructed

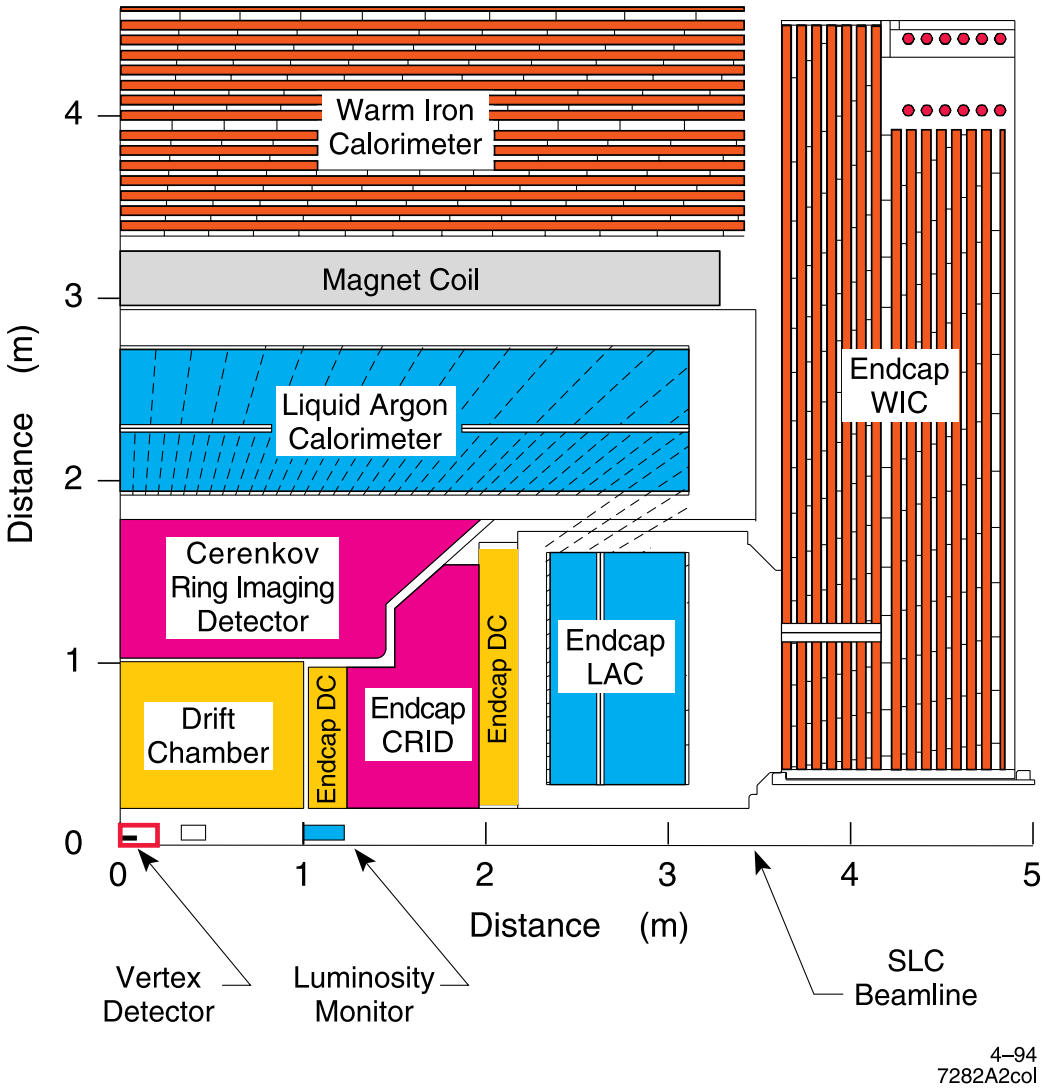

Figure 2.3: SLD section.

tracks are later used to find particle decay vertices. Whereas conventional wire- or strip-based detectors can only measure positions accurately in the dimension transverse to the wire or strip (ϕ for a cylindrical detector), the great advantage of pixel-based detectors like the VXD3 is that they can make measurements in both dimensions along the surface of the detector (ϕ and z). The high cost of large area CCDs constrains CCD detectors to be inner, low radius detectors, to be used in conjunction with cheaper larger radius strip or wire detectors. The inner detector is used for making precise position and direction measurements, while the outer detector with its longer lever arm is used for measuring the curvature of the trajectory.

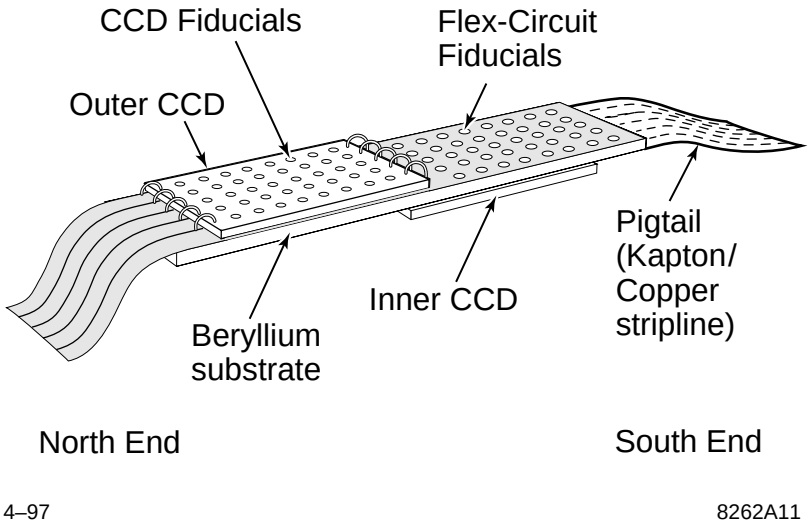

Figure 2.4: VXD3 ladder geometry.

The VXD3 consists of three cylindrical barrel layers of radius $\sim$ 2.8 cm, $\sim$ 3.8 cm and $\sim$ 4.8 cm respectively. The sides of each barrel are shingled with rectangular support structures called 'ladders,' 12 in layer 1 (the innermost layer), 16 in layer 2, and 20 in layer 3. Each ladder has two 1.6 cm $\times$ 8.0 cm CCDs attached, giving a total

of 96 CCDs. The ladder geometry is shown in figure 2.4. The CCDs covering the Northern hemisphere of the detector ($\cos\theta > 0$), are mounted on the outer surface of each ladder, and the CCDs covering the Southern hemisphere ($\cos\theta < 0$) are mounted on the inner surface. The layout of CCDs is displayed in figure 2.5. The total radiation length of the ladders plus CCDs in each layer is 0.4%. The 3-layer angular coverage of the detector extends to $|\cos\theta| < 0.85$. Each CCD contains 800 $\times$ 4000 pixels with pixel size 20 μm $\times$ 20 μm and charge deposition region extending to a depth of 20 μm.

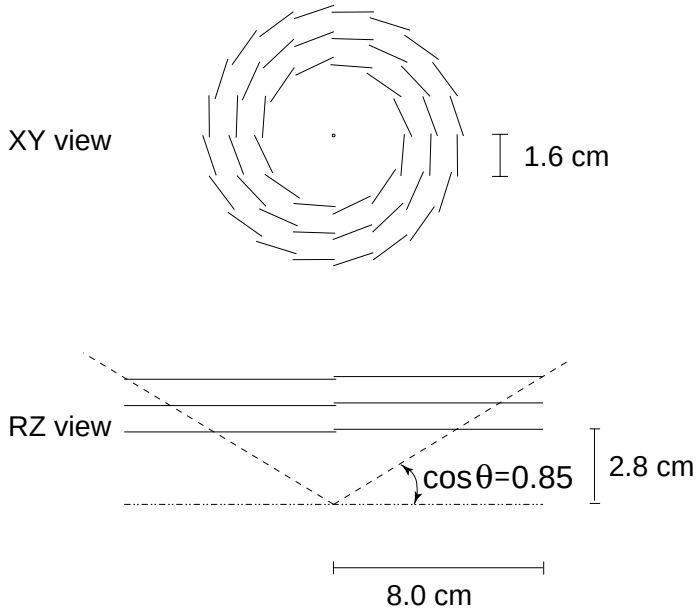

Figure 2.5: The VXD3 detector geometry.

An example of a typical $B\bar{B}$ event observed in the data is shown in figure 2.6 in the RZ view and in figure 2.7 in the $R\phi$ view. The precise track position measurement allows the extrapolated $B\bar{B}$ tracks to be resolved from the IP as shown in the zoomed

$R\phi$ view in figure 2.8. The measured tracks may be intersected to reconstruct heavy hadron decay vertices as discussed in chapter 6, and used in heavy flavor tagging. The B and $\bar{B}$ vertices are clearly visible in figure 2.8, each at approximately 2 mm separation from the primary vertex.

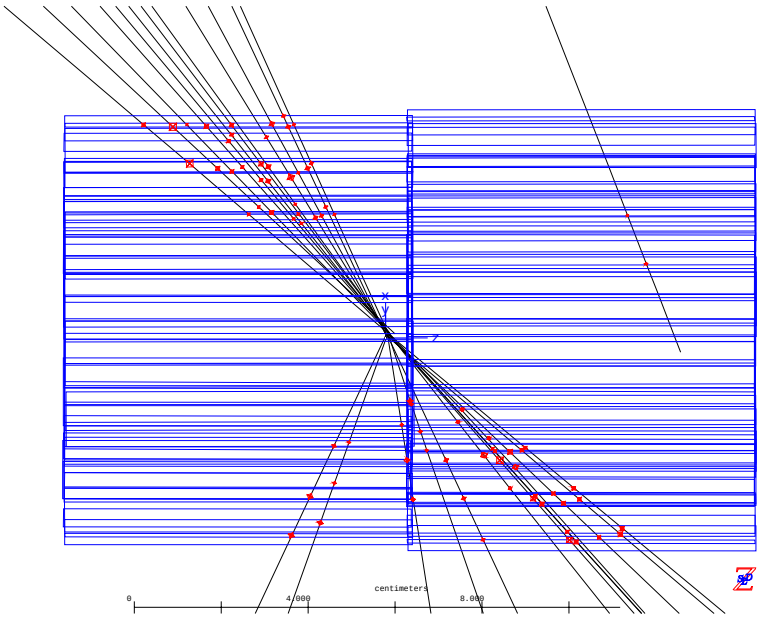

Figure 2.6: The RZ view of a typical $B\bar{B}$ event. Scale = 2 cm.

The VXD3 tracking resolution is significantly better than that of other contemporary detectors. The ability to measure full 3D positions comes at the expense of a slow CCD readout speed ($\sim$ 200 ms for a full readout), but this is not a problem for a relatively low event rate machine like the SLC. The low SLC beam related background levels also allow the innermost detector layer to be placed very close ($\sim$ 2.8 cm) to the IR without suffering excessive radiation damage to the CCDs. The errors in extrapolating a particle trajectory from the innermost detector hit back to the IR are

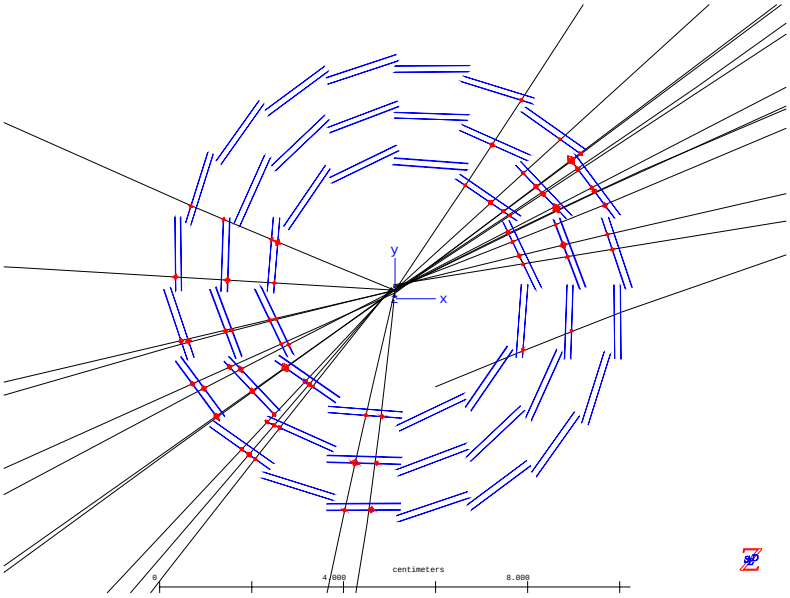

Figure 2.7: The $R\phi$ view of a typical $B\bar{B}$ event. Scale = 2 cm.

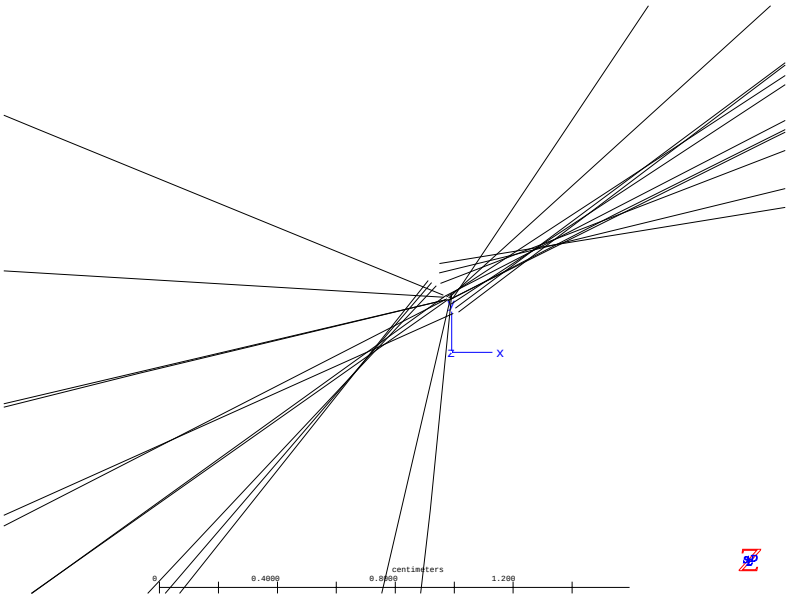

Figure 2.8: The zoomed $R\phi$ view of a typical $B\bar{B}$ event. Scale = 2 mm.

therefore much reduced.

2.4 The Central Drift Chamber

The wires of the CDC are arranged in drift cells, with each drift cell containing 8 anode wires and an arrangement of cathode wires called 'field' wires in order to shape the drift field. The arrangement of wires in the CDC is shown in figure 2.9. The drift cells are arranged in 4 axial superlayers (layers 1, 4, 7, 10) and 6 stereo superlayers (layers 2, 3, 5, 6, 8, 9). Wires in axial superlayers are strung parallel to the z axis of the cylindrical geometry. Stereo wires are also strung in a cylindrical geometry, but with a slight relative twist between the two endplates on which the wire ends are mounted. Because of this twist, called the 'stereo angle,' the assumed $R\phi$ position of a hit on a stereo wire gives information about the z position of the hit. In practice, the z measurement from the vertex detector is much more precise, and the stereo wire z information is mainly used in the track reconstruction.

The drift gas is $\sim$ 21% argon for charge amplification, and $\sim$ 75% CO_2, $\sim$ 4% isobutane, and 0.2% H_2O. The transverse position resolution is $\sim 100\mu$m.

The large set of hits in the CDC must be grouped together somehow to find the particle trajectories. The first step in reconstructing the tracks is the recognition of helical patterns in the hit distribution. The pattern recognition algorithm and track fit are discussed in appendix C.

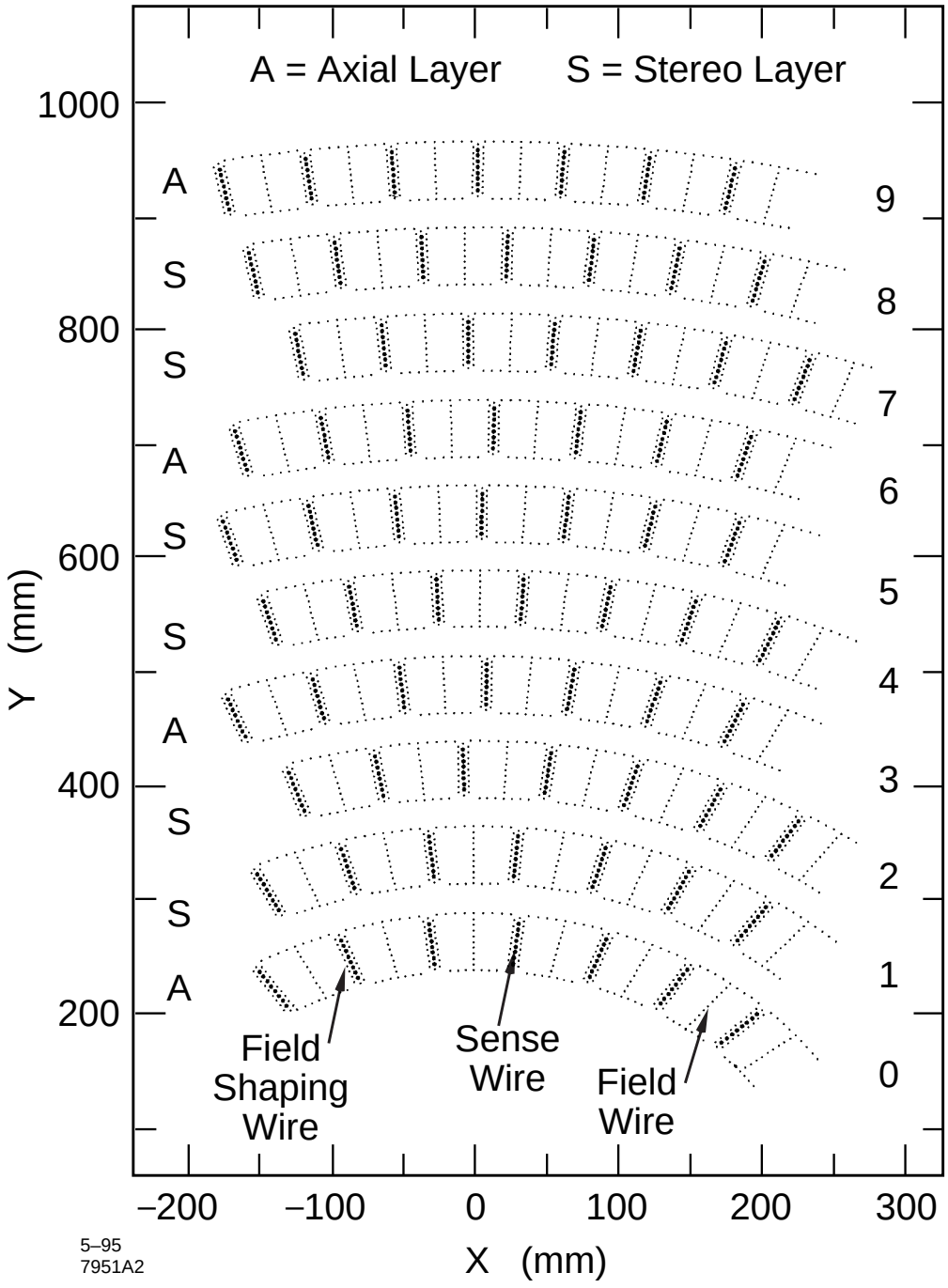

Figure 2.9: The CDC wire geometry.

2.5 Analysis of the Tracking Chambers

For the purposes of a vertexing analysis, the most important detector components are the tracking chambers. The vertex resolution derives directly from the transverse track resolution, and the assumed track errors must be calculated from the measured track momentum. In this section, the resolutions of the CDC and VXD3 are discussed.

2.5.1 Momentum measurement with the drift chamber

To measure the momentum, a spatially uniform $B = 0.6\,T$ magnetic field is generated throughout the tracking chambers oriented along the beam axis. Charged particles then move along helices coaxial with the magnetic field direction. The momentum transverse to the field is given by

$$P_t = Q \cdot B \cdot R_c \tag{2.1}$$

where R_c is the radius of curvature of the projection of the helix to a circle. Written in convenient units, this formula gives:

$$\begin{aligned} P_t &= \left(\frac{c}{\mathrm{m/s}}\right) \times 10^{-9} \cdot \left(\frac{B}{\mathrm{T}}\right) \cdot \left(\frac{R_c}{\mathrm{m}}\right) \ [\mathrm{GeV}/c] \\ &\approx 0.003 \left(\frac{B}{\mathrm{T}}\right) \cdot \left(\frac{R_c}{\mathrm{cm}}\right) \ [\mathrm{GeV}/c] \end{aligned} \tag{2.2}$$

For the SLD's relatively small magnetic field, the typical R_c is about 500 cm.

For realistic detector sizes of ∼1 meter, the particle trajectories look very close to straight lines with small xy deviations that can be locally described to a very good approximation as parabolic.

$$y(x) = y_0 + \frac{1}{2}K \cdot (x - x_0)^2 \tag{2.3}$$

where x is the distance along the tangent vector at the point (x_0, y_0), and $y - y_0$ is the transverse deviation from a straight line and $K \equiv 1/R_c$ is the curvature.

Measurements of a discrete set of hits along the track may be thought of as measurements of these small transverse deviations. The resolution of a tracking chamber in measuring both the direction of the tangent vector and the particle momentum is therefore determined by the precision of the transverse position measurements $\sigma_{r\phi,z}$.

Expressing the curvature as:

$$K = 2(y - y_0)/(x - x_0)^2, \tag{2.4}$$

the resolution in $1/P_t$ is then approximately:

$$\sigma_{1/P_t} = \frac{1}{0.003B} \cdot d(K) = (1/0.003B) \cdot F(n) \cdot \sigma_{r\phi,z}/r^2 \tag{2.5}$$

where r is the effective radius of the detector between the innermost and outermost hits, and F(n) is a statistical factor dependent on the number of hits that are measured. For large n, $F(n) = \sqrt{720/(n+4)}$. For the SLD drift chamber, n = 80, $\sigma_{r\phi} \approx 100$ μm, and r = 80 cm, giving an ideal $1/P_t$ resolution of 0.0025 c/GeV,

ignoring scattering effects. The measured asymptotic resolution 0.0049 c/GeV is somewhat worse, presumably due to alignment effects and drift time variations [19]. Combined with vertex vertex detector information, the overall momentum resolution is measured to be:

$$\sigma_{1/P_t} = 0.0026 \oplus \frac{0.0095}{P_t^2} \tag{2.6}$$

2.5.2 Position measurement with the vertex detector

A minimum ionizing charged particle passing through the 20 μm active region of the CCDs liberates approximately 10^3 electrons ($\sim$ 80 electrons/μm) which are collected in a grid of local potential wells of dimension $20 \times 20 \times 20$ μm^3, yielding a discrete pixellated measurement of a particle's trajectory. Assuming Gaussian statistics, a hit completely contained within a pixel has a transverse resolution of 20 μm/$\sqrt{12}$ = 5.8 μm, but enough clusters span more than one pixel that a cluster centroid algorithm can be used to improve the average local hit resolution to approximately 4 μm in the directions transverse to the particle trajectory.

This local hit resolution is measured by finding combinations of 3 hits linked to a common drift chamber track. The track is forced to go through the innermost and outermost of the 3 hits in the 'triplet,' while retaining its measured curvature. The residual of the middle hit to the interpolated track position plotted in figure 2.10 is a direct measurement of the local hit resolution. The width of the residual distribution divided by the average lever arm factor of $\sqrt{1.5}$ gives the single hit resolution as 3.6 μm in the $r\phi$ projection and 3.9 μm in z.

In order to reconstruct the particle decay vertices near the IP, tracks measured in

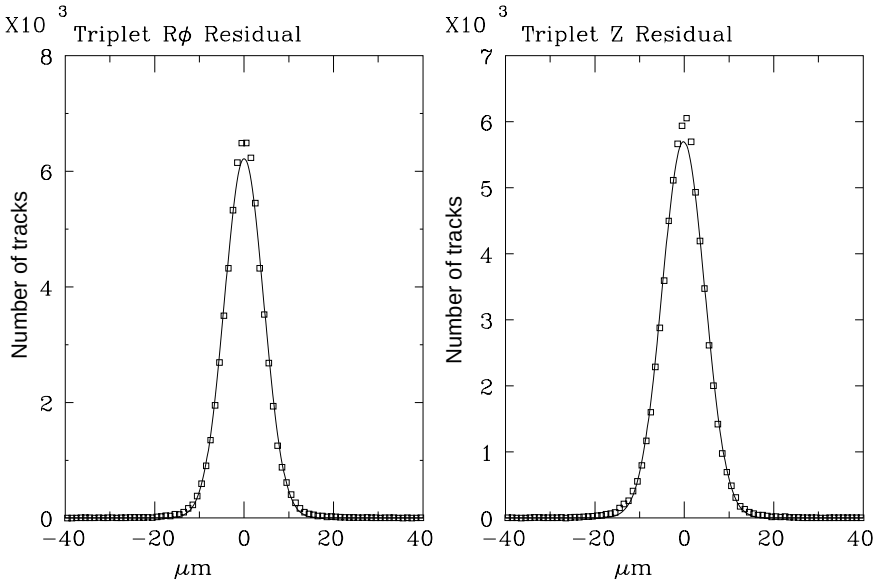

Figure 2.10: The VXD3 triplet residuals in $r - \phi$ and in z.

the detector must be extrapolated or 'swum' back to positions near the IP. This is accomplished by numerically integrating each track's equation of motion. In each of a series of discrete steps, one must calculate the new tangent vector to be used in the next step, and also the new track error matrix including possible effects of multiple Coulomb scattering if the particle passes through any material. As will be shown in chapter 5, the performance of the tracking systems in vertexing is directly related to the transverse track error near the IP. This error may be characterized by the impact parameter resolution, i.e. the error in the measurement of the impact parameter of the swum track to the IP.

By examining the parabolic expression for a particle trajectory given in equation 2.3, it is evident that the transverse errors have three sources: a constant due to the error on the initial position of the track, a tangent vector angular error whose

effects grow linearly with the swim distance, and a curvature error whose effects grow quadratically with the swim distance. To minimize the errors, the swim is started at the innermost detector hit in the VXD3, which typically occurs at a radius of 2.8 cm. The constant error is then just the 4 μm transverse error on this hit. For centimeter scale swim distances, the curvature error of order 0.1 $\mu\text{m}/\text{cm}^2$ is negligible, so the only remaining error comes from the tangent vector angle ϕ.

The ϕ error has two sources: transverse detector resolution, and multiple Coulomb scattering. Since the VXD3 inner and outer layers are separated by 2 cm, the detector resolution part may be estimated as

$$\begin{aligned} \sigma_{\phi,res} &= \frac{4\ \mu\text{m}}{2\ \text{cm}/\sin\theta} \\ &= 2\sin\theta\ \left[\frac{\mu\text{m}}{\text{cm}}\right] \end{aligned} \tag{2.7}$$

The multiple scattering contribution has a Gaussian core of width

$$\sigma_{\phi,ms} \approx \frac{13.6\times10^{-3}[\text{GeV}]}{p\cdot v}\cdot\sqrt{\frac{x}{X_0}} \tag{2.8}$$

where x is the width of material traversed, and X_0 the radiation length of the material. The various possible scatters of a particle as it moves through the detector must be modelled in the fit to the detected hits. For this discussion, only the scatters between the IP and the VXD3 layer 1 will be considered. Including layer 1, there is approximately 0.92% X_0 of material at approximately the layer 1 radius. This gives

a scattering angle distribution of width

$$\sigma_{\phi,ms} = 13.0 \left[\frac{\mu\text{m}}{\text{cm}}\right] \cdot \frac{[GeV]}{p \cdot v \cdot \sqrt{\sin\theta}} \tag{2.9}$$

The total transverse position resolution at the IP can then be estimated as:

$$\begin{aligned} \sigma_{r\phi,z} &= 4\ \mu\text{m} \oplus \left(2\sin\theta + \frac{13\ [\text{GeV}]}{p \cdot v \cdot \sqrt{\sin\theta}}\right) \left[\frac{\mu\text{m}}{\text{cm}}\right] \cdot \left(\frac{2.8\ \text{cm}}{\sin\theta}\right) \\ &= 6.9\ \mu\text{m} \oplus \frac{36.4\ [GeV]}{p \cdot v \cdot \sin\theta^{3/2}}\ \mu\text{m} \end{aligned} \tag{2.10}$$

where $2.8\ cm/\sin\theta$ is the swim distance.

For typical particle momenta around 1 GeV, the impact parameter resolution is dominated by multiple scattering. In addition, single scatters may produce a large non-Gaussian tail falling as $1/\theta^4_{scat}$ in the scattering angle distribution, leading to much worse impact parameter resolution for a few percent of the tracks. It is therefore critical in detector design to minimize the amount of scattering material within the vertex detector.

The SLD measured impact parameter resolution is measured to be:

$$\sigma_{r\phi} = 8\ \mu\text{m} \oplus \frac{33}{(p/\text{GeV}) \cdot \sin\theta^{3/2}}\ \mu\text{m} \tag{2.11}$$

$$\sigma_{rz} = 10\ \mu\text{m} \oplus \frac{33}{(p/\text{GeV}) \cdot \sin\theta^{3/2}}\ \mu\text{m}. \tag{2.12}$$

The transverse beam position measurement errors are approximately 3.2 μm as is discussed in chapter 4. After subtracting these errors, the measured impact param-

eter resolution can be seen to be in fairly good agreement with the track transverse resolution estimated before. The slightly larger asymptotic resolution in rz may be due to CCD shape effects at high $\cos\theta$ giving a transverse hit resolution worse than $\sim$4 μm and/or hit inefficiencies in the innermost VXD3 layer requiring some tracks to have longer swim distances.

Another method of measuring the resolution is to use $Z^0 \rightarrow \mu^+\mu^-$ decays. In these 'μ-pair' events, the two 45.6 GeV muons fly out back-to-back along very straight trajectories. Since they were both created at the same Z^0 decay point, the miss distance of the two reconstructed tracks gives a good measurement of the asymptotic high momentum transverse resolution independently of the beam position measurement. This distribution is shown in figure 2.11. Dividing the widths of these distributions by a statistical factor of $\sqrt{2}$, the single track transverse resolution is measured to be:

$$\sigma_{r\phi} = 7.7\ \mu\text{m}, \quad \sigma_{rz} = 9.6\ \mu\text{m},$$

also in good agreement with the estimate.

The performance of the vertex detector may also be somewhat degraded by alignment errors. The resolution results reported in this chapter are achieved only after a careful internal alignment procedure is performed Although local sections of the detector may be internally aligned well enough to achieve ~ 4 μm hit resolution, each local section must still pieced together with the other local sections. The procedure of aligning the detector and simulating the resolution will be discussed in chapter 3.

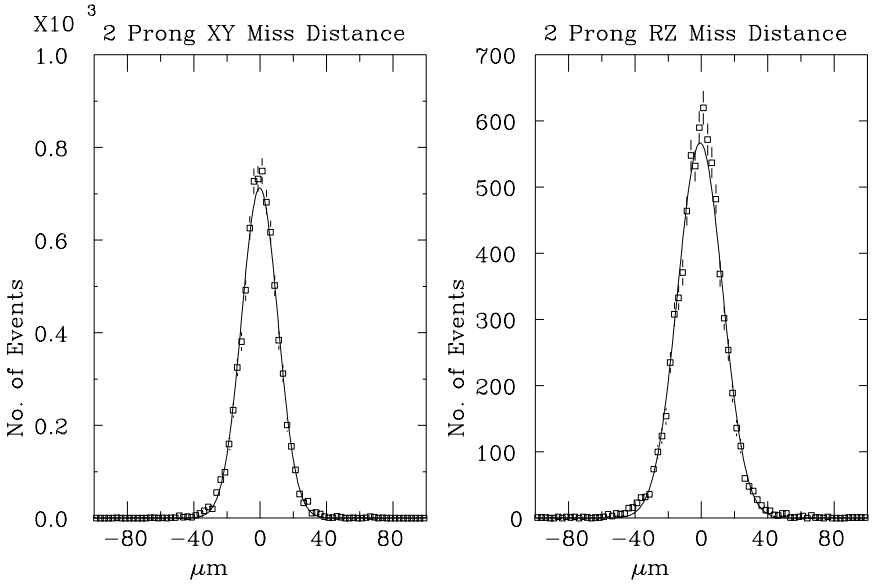

Figure 2.11: The $\mu^+\mu^-$ track miss distances in xy and in z.

Chapter 3

Vertex Detector Alignment

It is useful to distinguish between four separate issues concerning detector alignment. First, the physical alignment of the detector occurs during the construction and installation of the detector. CCDs are carefully mounted on ladders which are then inserted into the detector frame. The whole assembly is placed inside the SLD barrel and aligned with respect to the drift chamber. The subsequent cooling of the detector to operating temperatures affects the physical alignment through thermal contraction and associated geometric distortions.

Next, a detector alignment model is created in order to parameterize the observable misalignments and thereby make corrections to the interpretation of collected data. Physical effects such as CCD misplacement, thermal contraction, gravity sag, and distortions of the CCD shapes are all included in the modelling. The parameterization of small displacements from the ideal detector geometry allows small corrections to be made to the map from pixel coordinates on each CCD to physical

3-dimensional space. More detailed information on the alignment procedure may be found in [17] for the VXD3 internal alignment and [22] for the global alignment with respect to the drift chamber.

Third, the detector must be simulated for the generation of MC simulation data. With finite data sets, it is not always possible to construct a complete model for all possible misalignment effects, and so in this step, the remaining small misalignments are broadly characterized, and their effect simulated in the MC. The perfect geometry in the MC is degraded until it provides an adequate match with the data resolution.

Finally, estimators for the track errors should be calculated in a consistent way in the data and in the MC. Only then will χ^2 or confidence level cuts correspond to the same cuts on the assumed underlying distribution. For example, if the errors are underestimated by some amount in the data, this underestimation must also be modelled in the MC in order to make a fair comparison.

3.1 The Detector Alignment Model

The VXD3 detector alignment is done by minimizing the residuals of VXD3 CCD hits to tracks constrained by other hits. More specifically, combinations of 3 hits on distinct CCDs that are linked to the same drift chamber track are formed. The track is constrained to pass exactly through two of the hits while retaining its curvature (as measured by the drift chamber), and the distance residual of the remaining hit to the extrapolated/interpolated track position is plotted. Misalignments of any of the three CCDs involved cause the mean of the corresponding residual plot to deviate

from zero. So, the mean residuals plotted as functions of ϕ and $\tan\lambda$ provide a set of quantities to be minimized through reinterpretations of the CCD positions and orientations.

Each combination of 3 CCDs provides a local constraint on the relative alignments of the 3 CCDs with respect to each other. The most powerful constraints are from the 40 'triplet' regions which are combinations in which each of the hits is on a different barrel layer. These constraints can be imagined as girders enforcing the relative alignment of the barrels. The 96 'shingles,' combinations including two hits on the same layer in the $\sim$0.3-1.0 mm shingled overlap region between ladders, glue each detector layer together in ϕ. The 96 'doublets,' which are combinations including two hits on the same ladder in the $\sim$1.0 mm overlap region between the North CCD and the South CCD, serve to glue the Northern and Southern halves of each detector layer together.

One can still imagine that with this procedure of gluing CCDs together on their overlap regions may still yield a flattened or otherwise distorted cylinder, despite the structural support from the triplets. The μ-pair events provide a set of back to back high momentum tracks which may be used as girders to support diametrically opposite regions of the detector. Impact parameters of tracks to IP positions determined with previous alignments are also used in this way.

In principle, the set of residuals given by constraint equations may be simultaneously minimized through a χ^2 fit. In practice however, the number of parameters in the fit is too large to do this efficiently. Each CCD has 3 rotational and 3 translational degrees of freedom, so the total number of quantities to be determined is

$96 \times (3 + 3) = 576$.

Instead, an innovative technique developed by David Jackson is used. The residual parameters are reweighted according to their significance and the equations are solved by matrix inversion. Because each residual plot gives constraints on only 3 CCDs, the matrix to be inverted is sparse, and the numerical technique of singular value decomposition may be employed. In the final alignment, CCD shape distortions are also allowed as 4th-order polynomials in $\tan\lambda$, further increasing the complexity of the matrix equation.[1] As shown in figure 2.10, the local single hit resolution is improved to better than 4 μm after the data alignment.

3.2 MC Resolution Modelling

Although the tracking resolution is much improved after the VXD3 internal alignment and global alignment are done, it is still not perfect. The remaining misalignments are regarded as unavoidable and must be carefully modelled in the MC. The resolution in the MC derived from a perfect detector geometry must be degraded until it provides an adequate description of the true resolution of the detector.

The resolution degradation is done in two stages. The first constraint comes from the observation that μ-pair miss distances (figure 2.11) give a direct measurement of the asymptotic transverse tracking resolution. To match the miss distance distributions, the CCD positions in the MC model of the detector are smeared with Gaussians of an appropriate width. However, because of low μ-pair statistics, this constraint is

[1] λ is the polar angle measured from the xy plane.

not terribly strong.

The impact parameter distributions of tracks to the IP in *uds* events provides similar information except for the fact that the IP measurement (described in chapter 4) is itself derived from the track measurements. Nevertheless, given the hypothesis that the detector misalignments are symmetrically distributed about the correct alignment, the IP measurement is reliable on average and then the impact parameter distributions provide measurements of transverse track errors. The xy impact parameter may be defined as the xy projection of the distance of closest approach (DOCA) of a track to the beamline. A z position may be obtained from the point of closest approach (POCA) to the beamline of this track, and the distance in z between this position and the measured IP z position may be used as a measure of the z impact parameter. A comparison of the cumulative distributions for all hadronic events indicates that the Gaussian CCD smearing was by itself not large enough to account for all of the misalignment effects. See, for example figure 9.2 in chapter 9.

Examination of the impact parameter distributions in bins of solid angle reveals another feature: the means of the distributions exhibit systematic shifts as a function of $\cos\theta$ and ϕ. Figure 3.1 shows some examples of z DOCA distributions in four CCD triplet regions of ϕ. These plots reveal that the shifts of the means are truly shifts of the distributions and not due to spurious changes in the shapes of the distributions. Such shifts may potentially cause local systematic effects in vertexing due to correlations between the shifts in tracks from neighboring regions.

These impact parameter shifts observed in the data distributions are modelled in the MC simulation by taking tracks in those regions and systematically adjusting

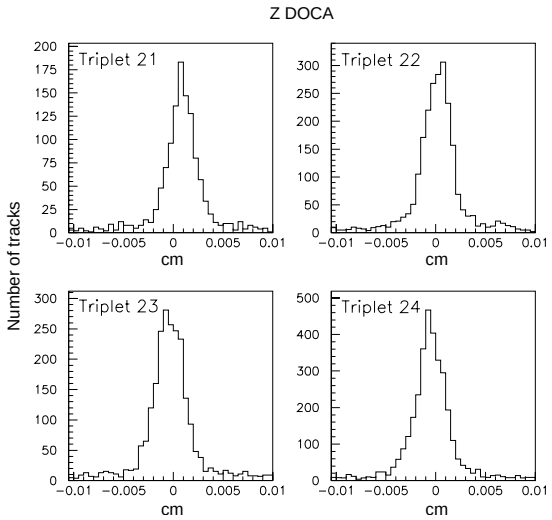

Figure 3.1: Data Z DOCA (distance of closest approach of the track to the beamline) distributions in several triplet phi regions. $0 < \cos\theta < 0.65$

their positions to match the observed shifts. In principle, the observed shifts could be due to either biases in the track positions which would give decay length independent effects on vertexing or due to biases in the track angle which would give effects which decrease with longer decay lengths. To model the worst case scenario, the impact parameter mismatches are modelled as being completely due to position shifts. The means of the xy and z impact parameter distributions in the data and the shifted MC are compared in figures 3.2 and 3.3. In each case, the detector is divided into four regions in $\cos\theta$ and into the 40 triplet phi regions. The $\cos\theta$ regions were chosen to isolate the larger CCD shape effects at high $|\cos\theta|$. Some further tuning was also done in the doublet region at very low $|\cos\theta|$. The cumulative shift distributions are shown in figure 3.4. These distributions show that the mean shift is $\sim$0.02 μm so that no unintended biases are introduced in heavy flavor decay length reconstruction. The effective correlated smearing is $\sim$3.3 μm in rϕ and $\sim$9.6 μm in z.

After the tuning is finished, the overall MC impact parameter distributions appear to be well-matched to those from the data. The comparisons are shown in figures 3.5 and 3.6, plotted in four regions of momentum and three regions of $\cos\theta$. In these plots, the xy impact parameters and the z DOCAs are signed with the thrust axis so the small positive tails are due to heavy flavor decays. Most of the tracks are IP tracks and so the overall width of the distribution is a measure of the momentum dependent tracking resolution. The matches in the low momentum plots indicate that multiple scattering in the detector material is being well-modelled. The matches at high momentum indicate that the remaining small detector misalignments are also now modelled. The xy impact parameter plots at high momentum indicate that

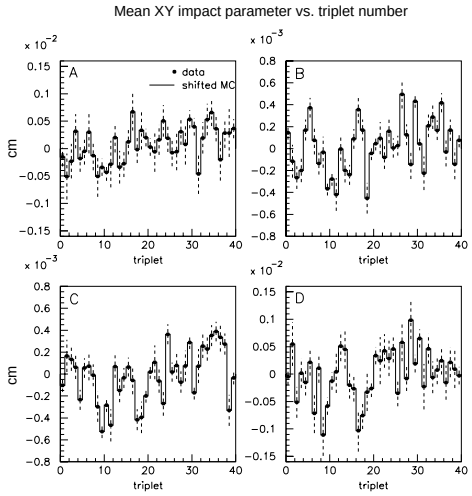

Figure 3.2: Data versus MC comparison of xy impact parameter means (cm) in 4 regions of $\cos\theta$ and 40 triplet regions of ϕ. (A) $\cos\theta <$ -0.65. (B) -0.65 $< \cos\theta <$ 0.0. (C) 0.0 $< \cos\theta <$ 0.65. (D) 0.65 $< \cos\theta$.

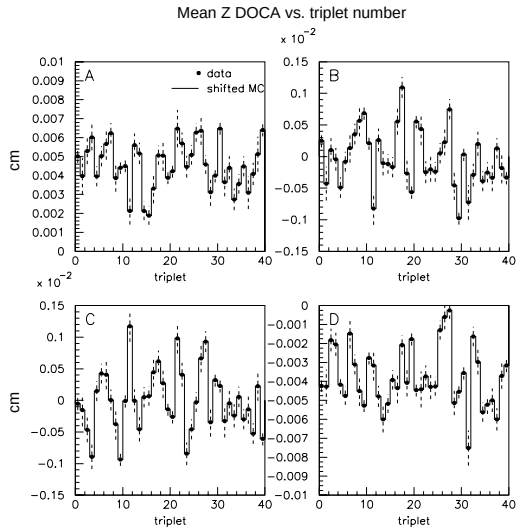

Figure 3.3: Data versus MC comparison of z impact parameter means (cm) in 4 regions of $\cos\theta$ and 40 triplet regions of ϕ.

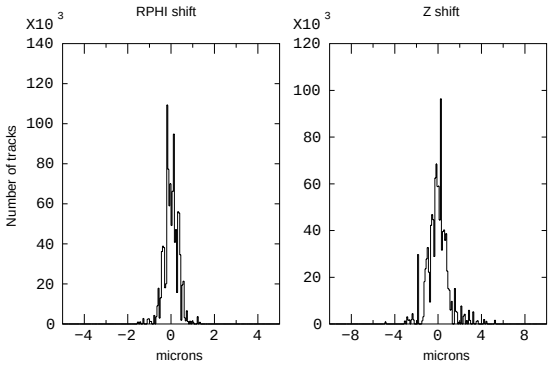

Figure 3.4: Cumulative shifts [μm]. Rϕ: mean=0.02, σ=3.3, Z: mean=0.02, σ=9.6.

the MC might be oversmeared by a small amount. This effect is presumably due to the two cumulative attempts to reproduce the misalignments, first with Gaussian CCD position smearing and next with the track position shifts. In principle, this oversmearing could be corrected with a future re-generation of the MC simulation.

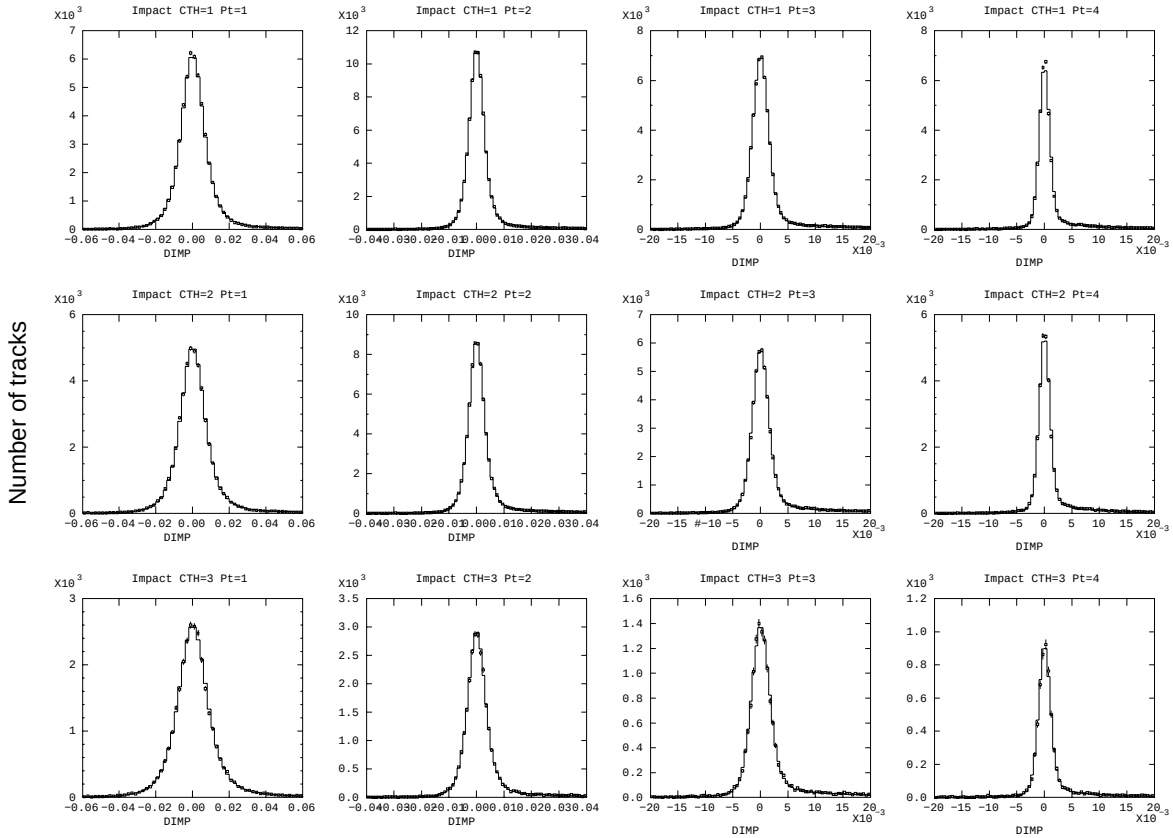

Figure 3.5: Data versus MC comparison of XY impact parameter distributions (cm) in 4 ranges of track P_t (left to right: < 0.7 GeV/c, 0.7-2.0, 2-5, > 5) and 3 regions of $|\cos\theta|$ (top to bottom: < 0.3, 0.3-0.55, > 0.55).

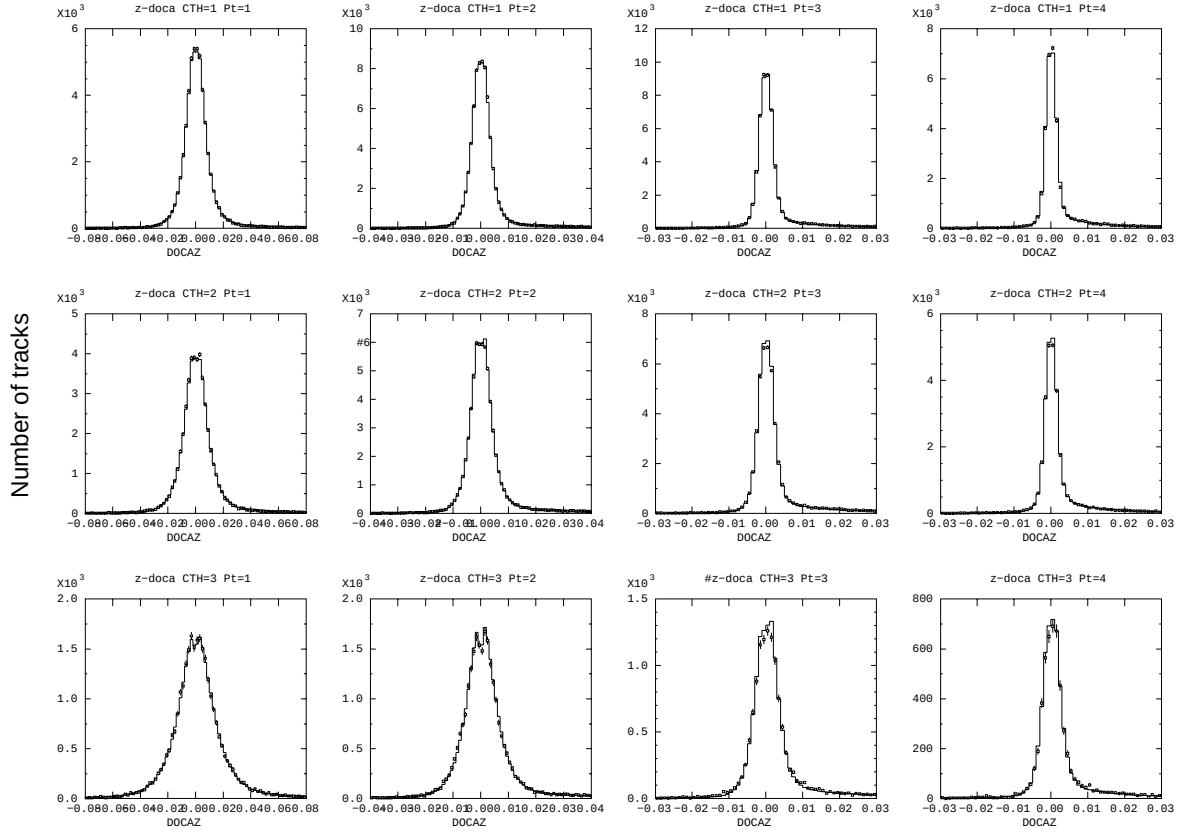

Figure 3.6: Data versus MC comparison of Z DOCA distributions (cm) in 4 ranges of track P_t (left to right: < 0.7 GeV/c, 0.7-2.0, 2-5, > 5) and 3 regions of $|\cos\theta|$ (top to bottom: < 0.3, 0.3-0.55, > 0.55).

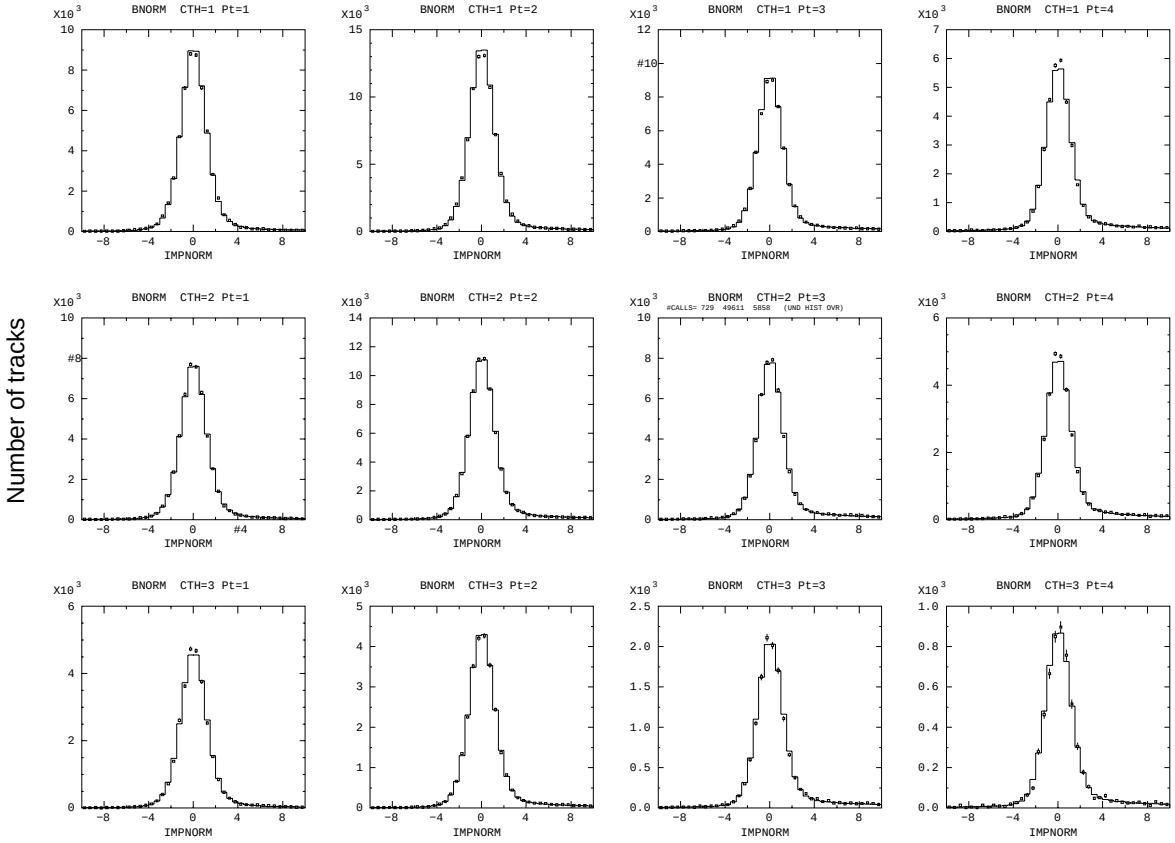

Figure 3.7: Data versus MC comparison of normalized XY impact parameter distributions in 4 ranges of track P_t (left to right: < 0.7 GeV/c, 0.7-2.0, 2-5, > 5) and 3 regions of $|\cos\theta|$ (top to bottom: < 0.3, 0.3-0.55, > 0.55).

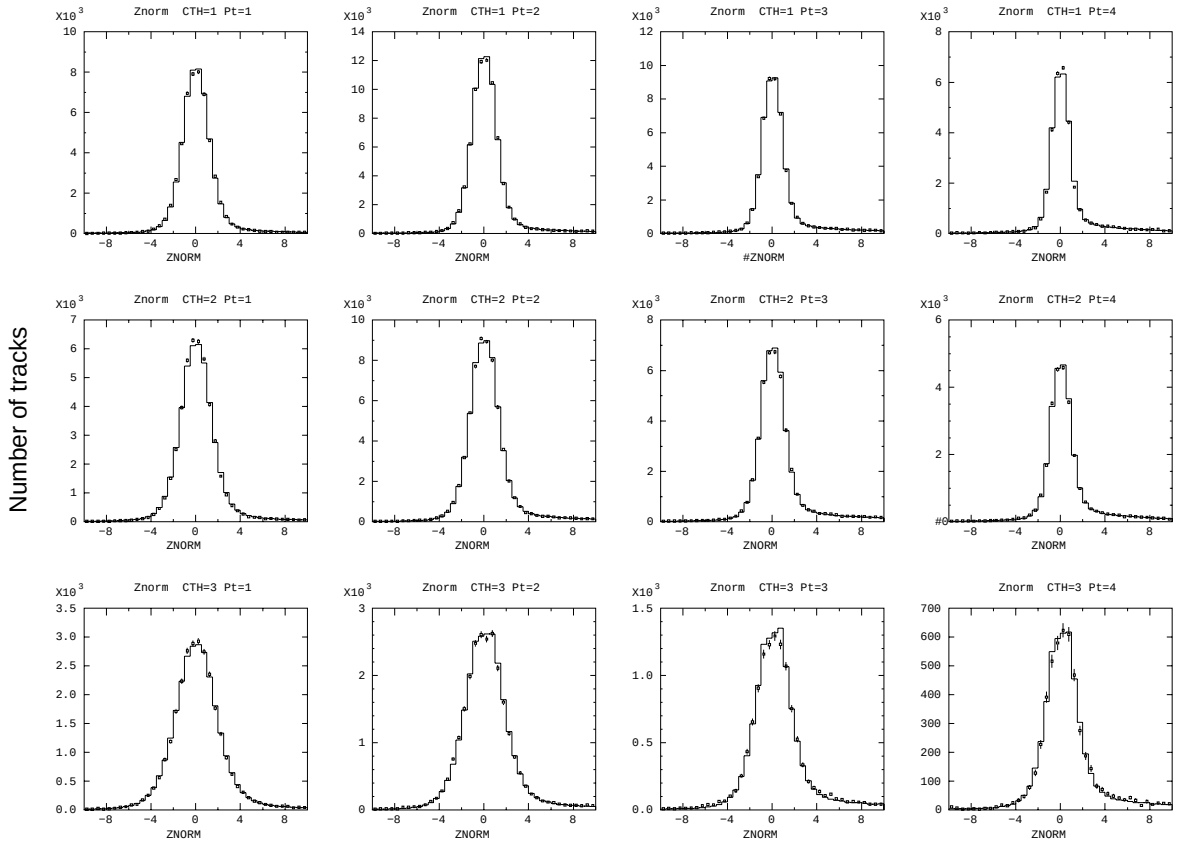

Figure 3.8: Data versus MC comparison of normalized Z DOCA distributions in 4 ranges of track P_t (left to right: < 0.7 GeV/c, 0.7-2.0, 2-5, > 5) and 3 regions of $|\cos\theta|$ (top to bottom: < 0.3, 0.3-0.55, > 0.55).

3.3 Error Estimators

The error estimators are calculated from CCD cluster centroid errors, CCD position errors, and multiple scattering errors, all propagated through the track swim to the IP. For both the data and MC the errors are calculated from a common geometry parameter set, and so they receive identical contributions from detector position errors and also from multiple scattering on known detector material. However, the CCD charge deposition model has not been well-tested and in principle, for high momentum tracks, small differences might be seen at the level of VXD3 cluster centroid errors. For example, the average number of pixels contained in clusters may be different, leading to a different average cluster resolution. Figures 3.7 and 3.8 show the normalized XY and Z impact parameter distributions, where each track impact parameter histogrammed has been normalized by the calculated error estimator for that track. Because of the common geometry used for the estimator calculation, no differences between data and MC are expected in these plots as long as the true error distributions are modelled correctly in the MC. Even at high momentum no significant discrepancies are seen, implying that the cluster centroiding differences are negligible.

Chapter 4

The Beam Position Measurement

The small stable IR of the SLC combined with the precise position resolution of the VXD3 allows the clean separation of heavy flavor decay tracks from IP tracks. The heavy flavor tracks may then be vertexed and the vertex kinematics analyzed to give a high efficiency, high purity B tag. In this section, a technique initially developed by Steve Wagner for measuring the beam position will be discussed.

The SLC has a small stable IR which is approximately 1 μm $\times$2 μm in the directions transverse to the beam and about 200 μm in the longitudinal direction. The longitudinal position of the Z^0 creation and decay may change from event to event by a relatively large amount over the 200 μm beam-beam overlap region, and so it must be measured event by event. The xy position variation is small enough that an event averaged determination is sufficient for physics analyses.

The xy position is determined using sets of Z^0 hadronic decays. The hadronic decays are jetty and have a well-defined thrust axis. Each track originating from

the IP in these jets may be used to measure the beam position in the direction transverse to the track. Because of the approximate colinearity of the jets in most events however, a single event may usually only measure the beam position in one of the two dimensions. Another event with an orthogonal thrust axis is required to measure in the other dimension. The typical track error is about 50 μm, so in order to make a precision measurement, many tracks should be used.

In the IP-finding algorithm, tracks from $\sim$30 consecutive hadronic events are fit to a common vertex in order to determine the beam position. Each event has approximately 15 usable quality tracks, and on average, half of the events measure the x position and half measure y. The expected precision in each dimension is then approximately 50 $\mu\text{m}/\sqrt{30 \cdot 15/2} = 3.3$ μm.

Tracks from heavy flavor decay vertices displaced from the IP may complicate the measurement. Approximately 40% of hadronic events are heavy flavor events. In these events however, a large fraction of the tracks still originate from the IP, so the non-IP track contamination is less than 20%. The average over 30 events gives a scatter of the $\sim$12 heavy flavor decays in ϕ which helps to avoid biasing the IP measurement towards the heavy flavor decay vertices in the event sample.

Another method to reduce this bias is to reject heavy flavor tracks based on their large impact parameters with respect to previous measurements of the IP. The procedure involves a running average over 30 events. Each time a new event is added, the weights from the oldest event in the sample are removed from the running sum. In this way, the newest event being considered always has the most current IP measurement. To reject tracks from long decay length heavy flavor vertices, only tracks

within 5σ in track errors to the most current measured IP position are included in the vertex fit.

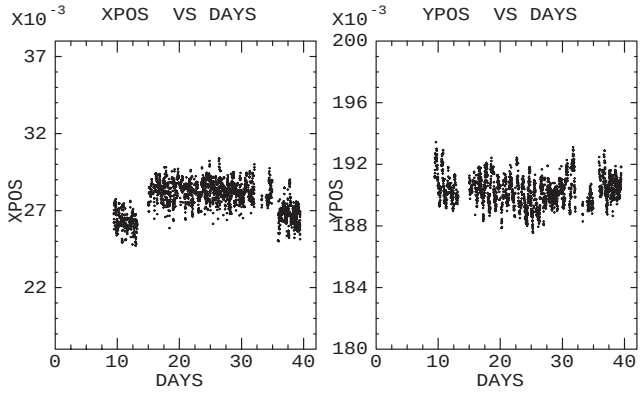

Figure 4.1: X and Y beam position measurement [cm] versus days.

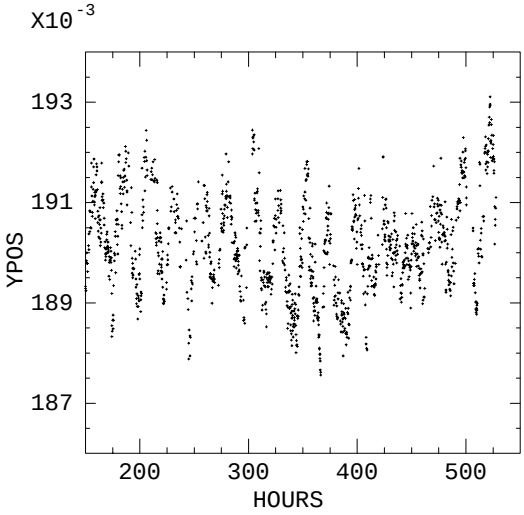

Figure 4.2: Zoom in: Y beam position measurement [cm] versus hours.

A typical time history of the x and y beam positions plotted in figure 4.1 shows that the beam position is stable under continuous machine running, but may change when machine operating conditions are changed such as during downtimes. Zooming

in to an hourly time history, figure 4.2 shows that the beam position drifts from day to night by about 40 μm or about 3 μm/hour, presumably due to temperature variations. The 30 hadronic events used in the measurement occur typically within a time period of 15-30 minutes depending on the current machine luminosity, so the assumption of beam stability over the averaging time is justified. Run periods in which the time history shows the beam position changing rapidly are vetoed for heavy flavor analyses since the average IP measurement is not reliable for these periods.

The beam position measurement errors are measured on average using μ-pair events. The impact parameter of these high momentum tracks is plotted in figure 4.3. These distributions are the convolution of the IP error distribution with the high momentum track error distribution. The width of the latter distribution is independently measured to be $\sim$7.55 μm from the miss distance of μ-pair tracks to each other. The fitted width of the impact parameter distribution is 8.2 μm, and so the IP measurement errors may be estimated as $\sigma_{IP} = \sqrt{8.20^2 - 7.55^2} = 3.2$ μm.

The longitudinal IP position IP_Z must be measured event-by-event. In hadronic events, a median track algorithm developed by Dong Su is used. In each event, a set of well-measured tracks containing vertex detector hits is compiled. Each track is swum to its 2D point of closest approach (POCA) to the measured IP_{XY}. In 3D, this procedure may be viewed as finding the POCA of the track to the beam line. The z position at the POCA for fragmentation tracks (Z_{POCA}) is an estimator for IP_Z. However, tracks from heavy flavor decay vertices may intersect the beam line at rather large distances of order $c\tau/\sin\theta$ where τ is the lifetime of the decaying heavy hadron. Also, mismeasured tracks or tracks with large scatters in the detector

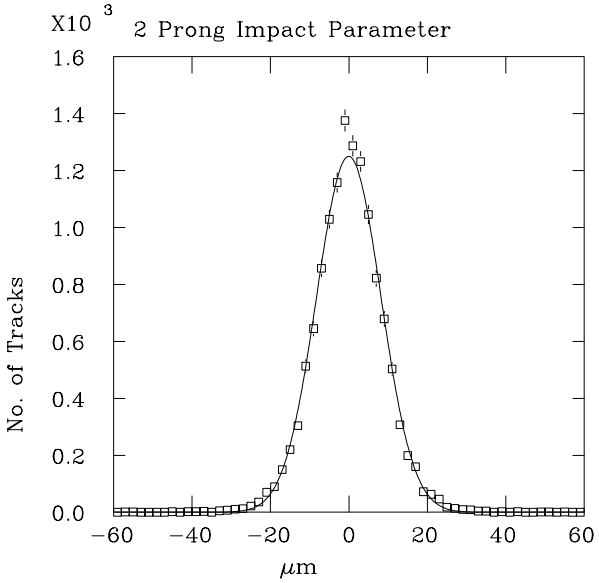

Figure 4.3: Impact parameter of μ-pair tracks to the measured IP position.

may cause the Z_{POCA} distribution to have a long tail. These large biases can lead to unacceptable errors in decay length measurements. So, instead of simply averaging the Z_{POCA} positions, the median Z_{POCA} position is chosen as the best estimator for the IP_Z. MC studies indicate that the resolution of this measurement is $\sim$20 μm on average.

Unfortunately, there is no independent measurement that can be made in the data to calibrate this resolution. In principle, dividing the Z^0 decay into hemispheres and using the median track in each hemisphere can give two independent measurements of IP_Z. The smaller number of fragmentation tracks in each hemisphere increases the probability that the median track is a heavy flavor decay track though, and the measurement resolution is degraded. So, for the charm counting analysis, the MC prediction of the resolution is used. The 20 μm resolution scale is so much smaller

than the typical millimeter decay length scale that the IP error may be neglected in decay length calculations. For vertexing in general, the confidence level cut to separate vertices from the IP is usually set to such a high value (99.5% in the current analysis) that any possible small difference between the data and the MC resolution does not cause a big change in the rate of fake vertex production from fragmentation tracks. The fake vertex production rate is considered further in chapter 6.

Chapter 5

Vertex resolution

5.1 Longitudinal track resolution

In chapter 2, we saw that the transverse track measurement resolution is:

$$\sigma_{r\phi} = 8\ \mu\text{m} \oplus \frac{33}{(p/\text{GeV}) \cdot \sin\theta^{3/2}}\ \mu\text{m} \tag{5.1}$$

$$\sigma_{rz} = 10\ \mu\text{m} \oplus \frac{33}{(p/\text{GeV}) \cdot \sin\theta^{3/2}}\ \mu\text{m} \tag{5.2}$$

The typically large boost of a B hadron in a Z^0 decay causes the Z^0, the B hadron, and the cascade D to be roughly colinear. We would therefore like to know the track resolution longitudinally along this decay axis. The longitudinal resolution is simply the transverse resolution divided by $\sin\alpha$ where α is the angle the particle makes with

the decay axis in the lab frame.

$$\sigma_L = \sigma_{r\phi,rz}/\sin\alpha \tag{5.3}$$

A heavy flavor decay track typically makes an angle α of order $1/\gamma$ with the decay axis. This angle may be calculated simply as

$$\begin{aligned} \tan\alpha = P_t/P_l &= \frac{P_0 \cdot \sin\alpha_0}{\gamma \cdot (P_0 \cdot \cos\alpha_0 + \beta \cdot E_0)} && (5.4) \\ &\approx (1/\gamma) \cdot \frac{\sin\alpha_0}{\cos\alpha_0 + 1} + \mathcal{O}(m^2/P_0^2, 1-\beta) && (5.5) \end{aligned}$$

where α_0 is the angle of the track with respect to the decay axis in the rest frame of the decaying particle, and E_0 and P_0 are similar rest frame quantities. The angular factor

$$\frac{\sin\alpha_0}{\cos\alpha_0 + 1}$$

multiplying $(1/\gamma)$ is typically of order one, but in principle can vary from zero to ∞ as P_{l0} or P_{t0} go to zero. For β close to 1,

$$P_l \approx E \approx \gamma(P_0 \cdot \cos\alpha_0 + E_0) \tag{5.6}$$

so large $\tan\alpha$ is only achievable for particles with very small lab frame energy E. Using a practical cut of $E > 0.5$ GeV to select usable well-measured tracks with

small errors, we get the requirement

$$\cos\alpha_0 > (0.5 \text{ GeV}/\gamma - E_0)/(\beta \cdot P_0)$$

For typical values of $\gamma = 6$, $E_0 = 0.5$ GeV, we find for pions,

$$\cos\alpha_0 > -0.87.$$

Then for isotropic decays, roughly $\sim 6\%$ of the solid angle of particles is useless for vertexing because these particles are boosted to lab frame energies below 0.5 GeV. Figure 5.1 (d) shows the longitudinal single track resolution as a function of $\cos\alpha_0$ for pions at two values of E_0. As argued, the resolution deteriorates quickly at large negative $\cos\alpha_0$.

Particles are also lost in the forward α_0 region where the particles do not have enough P_t to resolve vertex positions along the B decay axis. These particles have large lab frame energies and correspondingly small transverse errors around 8 μm, but this very precise resolution is degraded by the small α. As shown in figure 5.1 (d), again about $\sim 6\%$ of the solid angle is lost at high $\cos\alpha_0$. So, the total particle loss is $\sim 12\%$, and only $\sim 88\%$ of charged particles are potentially useful in resolving vertex positions. These inefficiencies have only been calculated for particles of average decay rest frame energy, and further inefficiencies due to low P_t can be expected for particles of lower rest frame energy.

From this discussion, we see that the poorer transverse resolution of lower momentum tracks is compensated by a larger angle α with respect to the B decay axis.

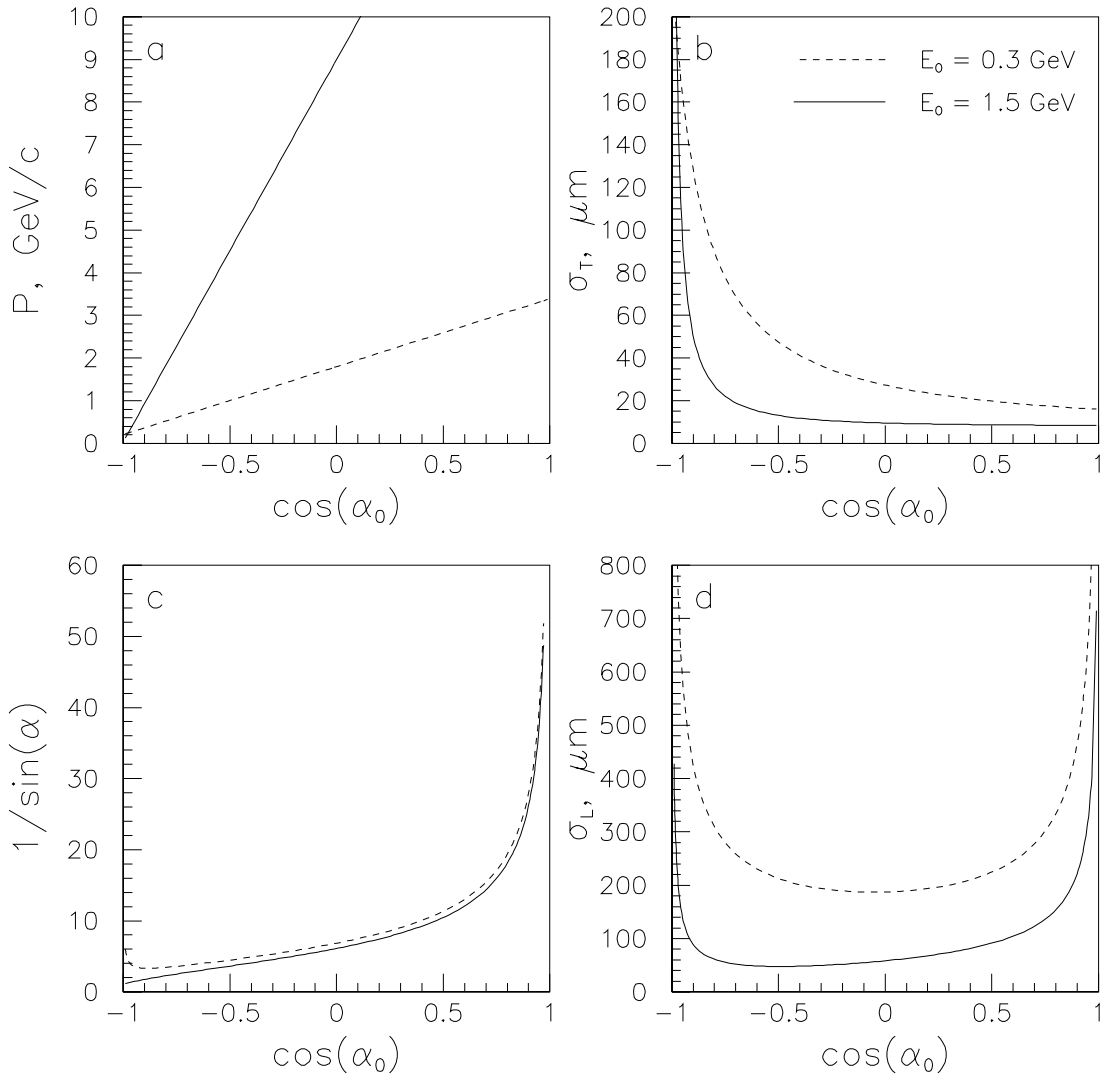

Figure 5.1: Predicted vertexing quantities in B decays: (a) Lab frame particle momentum P. (b) Transverse track errors. (c) Resolution projection factor. (d) Longitudinal track errors. All are plotted as functions of the B rest frame particle angle α_0. Plots are for pions at high and low B rest frame energies E_0. Note that the longitudinal resolution has roughly constant valleys where the resolution is mainly determined by the B rest frame energy.

The better transverse resolution of higher momentum tracks is degraded by a smaller α. Also, although the large boost of the B hadrons in a Z^0 decay expands the decay length of the B by a factor of $\gamma\beta$, the longitudinal track resolution is worse than the transverse resolution by almost the same factor of $1/\sin\alpha \approx \gamma$. So, in the end, the figure of merit in evaluating a detector's performance in resolving heavy flavor vertices is the ratio of the transverse track resolution to the lifetime $c\tau$, just as it is in analyses based on impact parameter measurements.

5.2 Data/MC Vertex Resolution Comparison

While the transverse tracking resolution has been calibrated between data and MC using μ-pair miss distances and track-IP impact parameter distributions, it would still be useful to see how well the track resolution information gets propagated to the found vertices. The $Z^0 \to \tau^+\tau^-$ events give a particularly clean system in which to make this measurement since each decay hemisphere contains only one $\tau^\pm$ vertex.

To calculate the vertex position resolution, we must first define operationally what we mean by a vertex. If the detector had perfect resolution, then a vertex can be defined as the intersection of tracks. For finite resolution, a vertex may be defined as a point with which a set of tracks have some finite probability of intersecting. This notion can be formalized by approximating the track transverse errors with Gaussian distributions, and calculating the χ^2 of a collection of tracks with the hypothesis of a common intersection point. The probability (confidence level) of this hypothesis provides a 1-parameter criterion for determining whether to group the tracks into

a vertex. Vertices may then be defined using a minimum probability requirement. Decays of $\tau^{\pm}$ into 3 charged particles can be used to study both the high probability and the low probability regions of the vertex χ^2 distribution in order to check that same effective definition of vertices is being used in both data and MC.

3-prong $\tau^{\pm}$ decays mostly occur through the broad $a_1(1260)$ resonance, but about a third of the time, an additional neutral hadron is produced. The typical charged pion energy might then be estimated to be $\sim$300 MeV in the $\tau^{\pm}$ rest frame. In Z^0 decays, each $\tau^{\pm}$ carries away 45.6 GeV of energy, resulting in a boost of $\gamma\beta = 25.6$.. The single track longitudinal resolution predicted by the formulae in the previous section are plotted in figure 5.2 as a function of $\cos\alpha_0$. Comparison with the corresponding plots in figure 5.1 shows that the longitudinal track resolution is somewhat degraded by the high boost of the decaying particle. The typical 1 σ single track resolution may be estimated as roughly $\sim$350 μm. Dividing this by $\sqrt{3}$ gives the predicted 3-prong vertex resolution as $\sim$200 μm.

The goal is then to measure the vertexing resolution by measuring the width of the negative tail of the 3-prong $\tau^{\pm}$ vertex decay length distribution. $Z^0 \rightarrow \tau^+\tau^-$ events are selected by using a set of cuts developed by Jim Quigley [23]. These cuts include track multiplicity cuts and jet energy/shape cuts to reject hadronic events and 2-photon events as well as track angle and momentum cuts to reject μ-pair and bhabha events. After selecting only 3-prong hemispheres, MC studies indicate that the non-$\tau^{\pm}$ background is below 0.2%.

The 3-prong $\tau^{\pm}$ decays in this sample are fit to a common vertex in order to obtain the $\tau^{\pm}$ decay point. To calculate the decay length, a measurement of the IP position

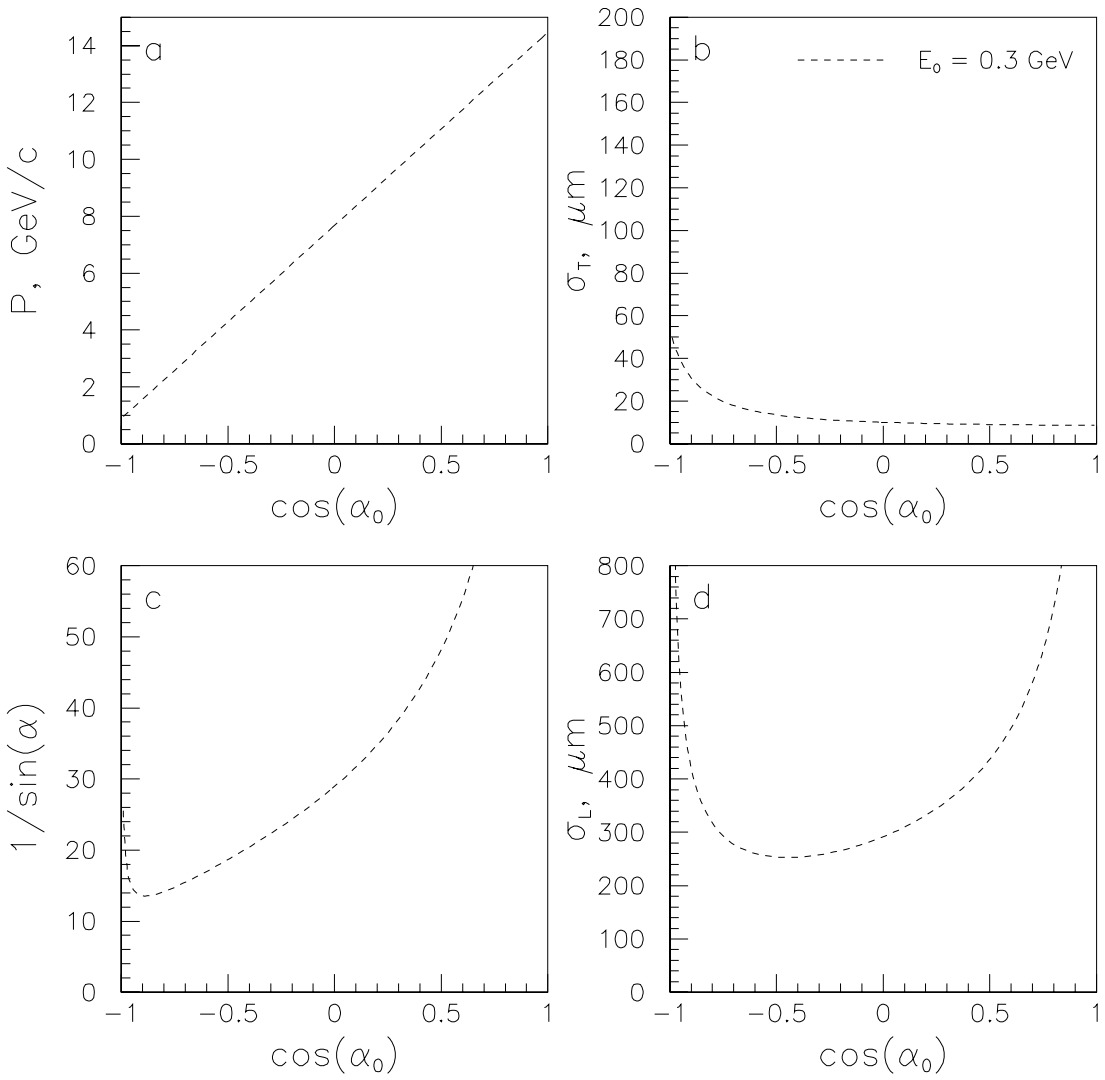

Figure 5.2: Predicted vertexing quantities in $\tau^{\pm}$ decays: (a) Lab frame particle momentum P. (b) Transverse track errors. (c) Resolution projection factor. (d) Longitudinal track errors. All are plotted as functions of the $\tau^{\pm}$ rest frame particle angle α_0. Plots are for pions at a typical $\tau^{\pm}$ rest frame energy $E_0 = 0.3$ GeV.

is needed. As described in chapter 4, the stable xy beam position can be measured from hadronic events occurring at around the same time as the τ-pair event. The IP z position must be determined from information in the current event however. Because of the high $\tau^{\pm}$ boost, the signature for a τ-pair event is two back-to-back highly collimated jets of particles. The IP z position can therefore be measured by forming the resultant momentum vector from all tracks in a jet, and finding its point of closest approach to the well-determined beamline. MC studies indicate that the error in this measurement is only $\sim$8 μm. The magnitude of this error is so much smaller than the 200 μm scale of the longitudinal errors that any correlations between the two measurements may safely be neglected. The measured decay length is calculated as the distance between the IP and the 3-prong vertex position.

The measured decay length distribution is fit to a convolution of an exponential distribution with a Gaussian smearing distribution:

$$\begin{aligned} f(x) &= \int d(x_0) \frac{1}{\sqrt{2\pi\sigma}} \exp\left(-\frac{(x-x_0)^2}{2\sigma^2}\right) \cdot \frac{1}{D} \exp\left(-\frac{1}{D}(x_0)\right) \\ &= \frac{1}{2}\left(1 + \mathrm{erf}\left(\frac{x-\sigma^2/D}{\sqrt{2}\sigma}\right)\right) \cdot \frac{1}{D} \exp\left(-\frac{1}{D}\left(x - \frac{\sigma^2}{2D}\right)\right) \end{aligned} \tag{5.7}$$

As can be seen from the form of this function, the average resolution σ is determined mainly from the negative tail of the distribution and the $\tau^{\pm}$ decay length constant $D \equiv \gamma\beta c\tau_{\tau^{\pm}}$ is determined mainly from the exponential tail at larger positive decay lengths. The fitted MC and data distributions are shown in figure 5.3, where a cut of vertex probability $> 5\%$ is used to limit the measurement to the core resolution. The MC and data resolutions agree very well with each other and with the analytic

estimate above.

The tails in the χ^2 distribution are important as well since they determine the rate of creating fake vertices. The vertex probability distributions in data and MC are compared in figure 5.4 in four regions in $\cos\theta$. The horizontal axes represent the integrated probability (confidence level) of the hypothesis that all three tracks originate from the vertex. These integrated probabilities are calculated from the assumed track errors. The probability distribution functions are normalized to unity so that the vertical axes may be interpreted as the measured probability per bin. If all errors were perfectly Gaussian, then these distributions would be flat with with a binned probability of 0.02 in each bin. The match between data and MC in the non-Gaussian tails at low confidence level appears to be reasonable.

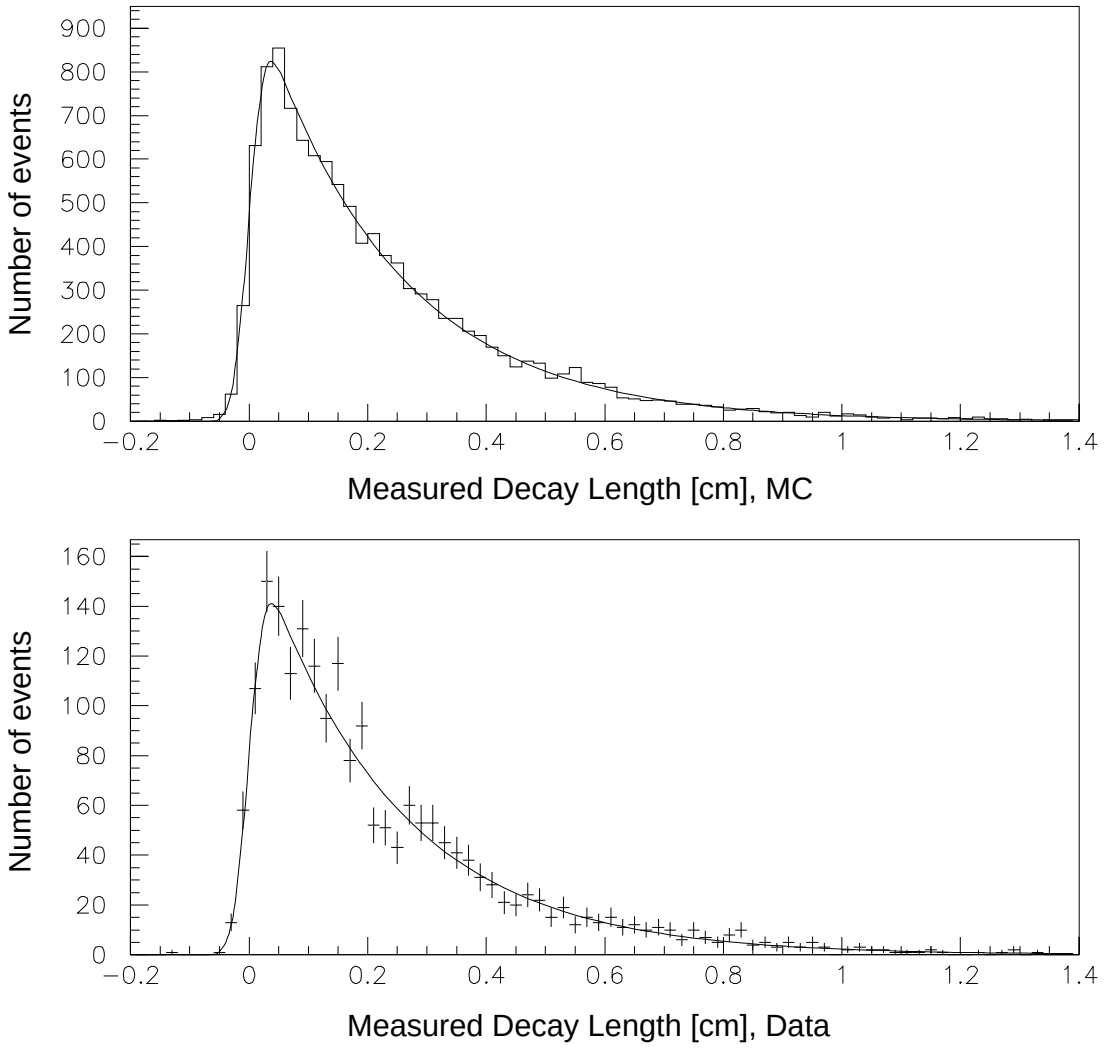

Figure 5.3: Measured $\tau^{\pm}$ decay length distributions (cm) in the MC (top) and the data (bottom). Only 3-prong vertices with vertex probability $> 5\%$ are plotted. The fitted MC resolution is 202 ± 8 μm and the fitted data resolution is 207 ± 14 μm. The uncorrected fitted lifetime is 300 ± 8 fs.

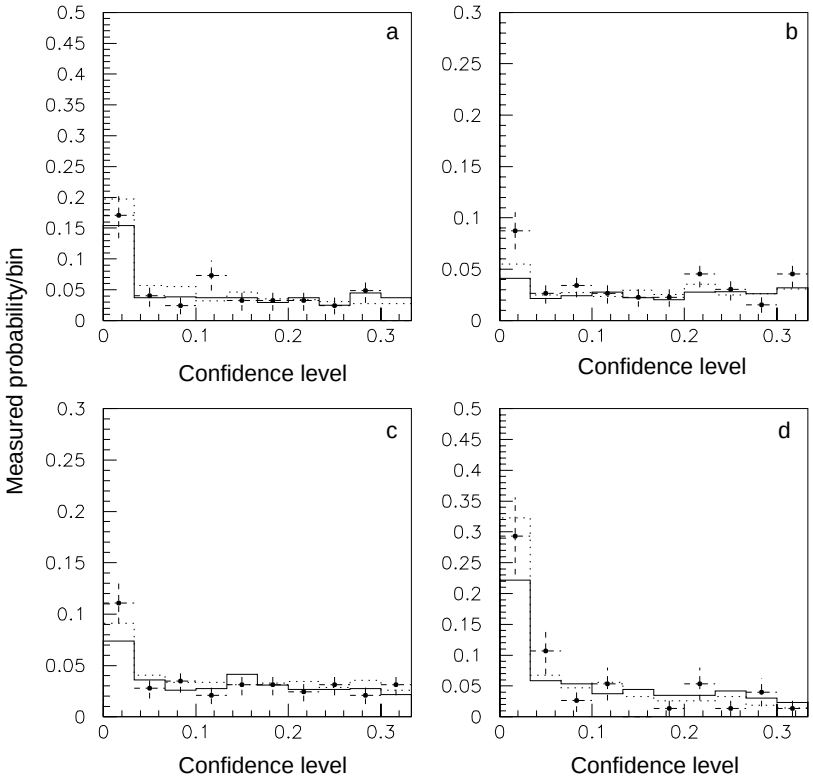

Figure 5.4: 3-prong $\tau^{\pm}$ vertex probability distributions as functions of the vertex hypothesis confidence level. The distributions are shown in 4 regions of $\cos\theta$: (a) <-0.65, (b) -0.65 to 0, (c) 0 to 0.65, (d) >0.65. The bin size is 0.02 and all distribution functions are normalized to unity. Solid histogram $\equiv$ vanilla MC. Dashed histogram $\equiv$ MC with track position shifts. Points $\equiv$ Data.

Chapter 6

Vertexing

To form multiple vertices from a set of tracks, some algorithm must be employed to determine which tracks to put in each candidate vertex. For this purpose, the primary tool used in this analysis is the ZVTOP3 topological vertexing package [24] developed by David Jackson to exploit the excellent SLD vertex detector resolution. It is used ubiquitously in SLD heavy flavors analyses as the first stage in heavy flavor tagging, and it is also the basis for similar physics studies for future linear colliders. ZVTOP3's purpose is to take a set of tracks and find a discrete set of points or vertices where they intersect within their position errors. It contains two separate methods for accomplishing this purpose, both of which are used in this analysis.

The first method is referred to as the resolubility algorithm. A Gaussian probability tube is made for each track to model the measurement uncertainty in the track's position. As shown in figure 6.1, the swum track position errors for the two directions transverse to the tangent vector are used to define a 2-dimensional Gaussian P.D.F.

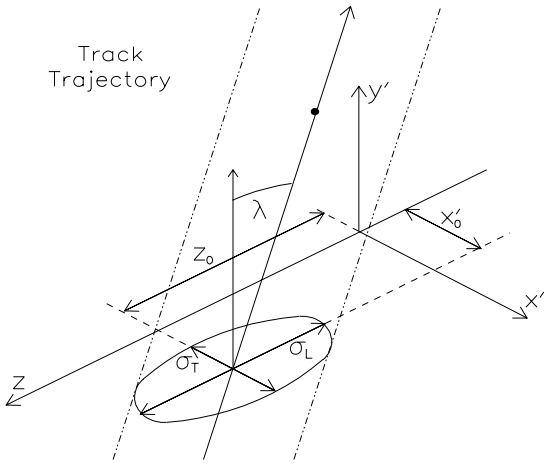

Figure 6.1: Defining the Gaussian probability tube for a track. x' and y' are local track coordinates. z is the beam direction and λ is the polar angle of the track tangent vector measured with respect to the transverse $x'y'$ plane. The Gaussian widths σ_T and σ_L in $R-\phi$ and z is defined using the track impact parameter errors.

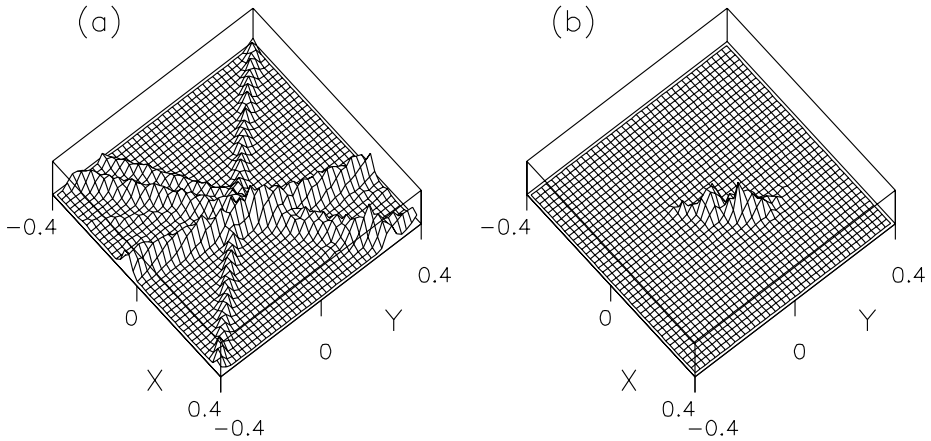

Figure 6.2: Left: Intersections of Gaussian track tubes. Right: the tube overlap function.

at each point along the measured track. The resolubility algorithm then looks for regions of large overlap of these probability tubes. Figure 6.2 shows an example of intersections of track tubes and the overlap function produced. Vertices are separated by requiring that local maxima in the overlap function are separated by deep enough minima. A similar Gaussian P.D.F. is used to model the uncertainty in the IP position in order to separate fragmentation tracks from heavy flavor decay tracks.

An obvious problem with this method is that it cannot find vertices for one-prong decays. Furthermore, the vertex separation method is not based on a rigorous probabilistic calculation, and so its performance in simultaneously finding both B and D vertices is limited. However the resolubility algorithm excels at finding single vertices well separated from the IP. It is a robust general-purpose algorithm to use in heavy flavor analyses, particularly in the heavy flavor vertex mass tagging described below.

The second method is called the ghost track algorithm [25] and it is used primarily to reconstruct the cascade structure of B decays. It attempts to recover some of the inefficiencies of the resolubility algorithm. Because of the large boost of the B particles in Z^0 decays, the B and D vertices in the decay cascade are typically close to being colinear with the IP. (The momentum of the D transverse to the B flight direction is typically very small compared to the longitudinal momentum.) The ghost track algorithm models this line from the IP to the B to the D by threading a 'ghost' track through all of the tracks in the hemisphere by fixing one end at the measured IP position and adjusting the angle to minimize the summed χ^2 it makes with the real tracks. The decay length of the heavy hadrons makes a long lever arm which

pulls the ghost track towards the true heavy hadron decay position. The transverse errors of the ghost track are determined from its largest normalized distance of closest approach (DOCA) with any track in the cascade once its direction has been fixed. The transverse error is defined such that every track in the hemisphere has $\chi^2 \leq 1$ when vertexed with the ghost track. The IP is again modelled with a Gaussian P.D.F. with dimensions 7μm $\times 7\mu$m $\times 30\mu$m.

A brute force probabilistic multiple vertex fit is then performed by calculating a set of vertex probabilities for all possible '2 tracks + ghost track' candidate vertices as well as all possible '1 track + IP' candidate vertices. The highest probability vertex is saved and the track(s) used in that vertex are flagged as used. Of the remaining candidate vertices, those which contain the used track(s) are rejected. New probabilities are then calculated for all possible 'saved vertex + 1 extra unused track' candidate vertices, and are considered along with the previous set of viable candidate vertex probabilities involving unused tracks. Again, the vertex with the highest probability is saved and the track used is removed from the list. New track appending data are calculated and the procedure continues until the highest probability found is lower than some probability cut criterion (PCUT), which is set to 0.5% in the current analysis. All remaining unvertexed tracks are considered to be incompatible with any multi-prong vertex and incompatible with the IP, and so they are vertexed with the ghost axis to form 1-prong vertices.

The use of the ghost track accomplishes two goals, each with its caveats. First, it has the ability to form 1-prong vertices by vertexing single tracks with the ghost axis. The position resolution of 1-prong vertices is not very good since a single track can

only localize a vertex in two of the three spatial dimensions. Information on the third dimension must come from the ghost axis, and is systematically biased. For example, the tangent vectors to tracks from a D decay may be considered as estimators for the D flight direction, and hence point back on average to the B decay position. If the ghost track is considered as an estimator for the B flight direction, then a 1-prong D vertex will typically intersect the ghost track close to the B decay position and underestimate the D decay length. A small fraction of these tracks from off-axis D decays will actually intersect the ghost axis in front of the B decay position giving an apparently negative D decay length. Similarly, since the ghost track typically points somewhere in between the B and D vertices, B decay lengths will be underestimated by 1-prong B vertices.

Second, by using brute force probabilistic vertex fitting, the algorithm is able to achieve a high efficiency for separating B and D vertices. The probabilities calculated are based on the assumed ghost track width however. Underestimates of this width give overestimates of the χ^2 and cause off axis vertices to be broken up and vertexed as sets of false 1-prongs on axis. Overestimates of this width will lead to an understimate of the χ^2 and inefficiencies in vertex separation. Underestimates are more common however since all tracks point back in general to the B decay vertex and therefore tend to give underestimates of the B-D transverse separation. Overestimates usually happen only when there are particles in the event which are not associated with the IP-B-D decay chain, such as products of decays of long lived particles or cosmic rays. A special 'tidy' option in ZVTOP3 attempts to remove K_s, Λ and gamma conversion tracks using kinematic cuts on neutral 2-prong vertices and also to reject other high

impact parameter tracks from detector interactions and/or from misreconstructions.

The MC predicted vertex finding efficiencies using the 'ghost track' algorithm are plotted in figures 6.3, 6.4, and 6.5 as functions of true IP-B separation, true B-D separation, and the smallest true vertex separation (Δ) in 2D decays. The effective vertexing resolution is about 0.5 mm which is sufficient to resolve most of the vertices in the decay chain.

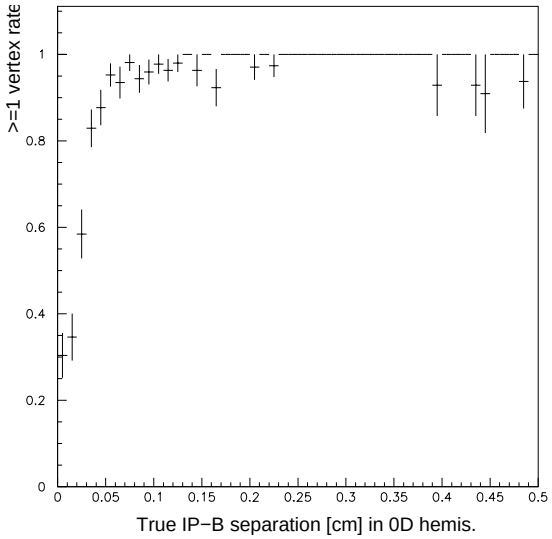

Figure 6.3: MC predicted 'B' vertex finding efficiency as a function of true IP-B separation in $0D$ hemispheres.

The plots do not asymptote to perfect efficiency at large true separation because of intrinsic inefficiencies due to vertex track multiplicity and kinematics, and possibly also due to further inefficiencies in the vertexing algorithm. For example, vertices producing no charged tracks are not detectable. This inefficiency is particularly serious for 2D decays where the 3-vertex rate asymptotes to only $\sim$40%. In the SLD B decay MC, all three heavy flavor decay vertices are visible only about 50% of the

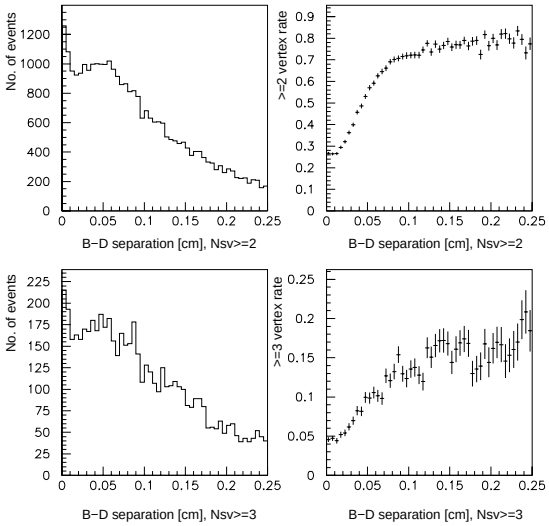

Figure 6.4: Left: True B-D separations in $1D$ hemispheres with ≥ 2, ≥ 3 found secondary vertices. Right: The corresponding vertex finding rates as a function of true B-D separation.

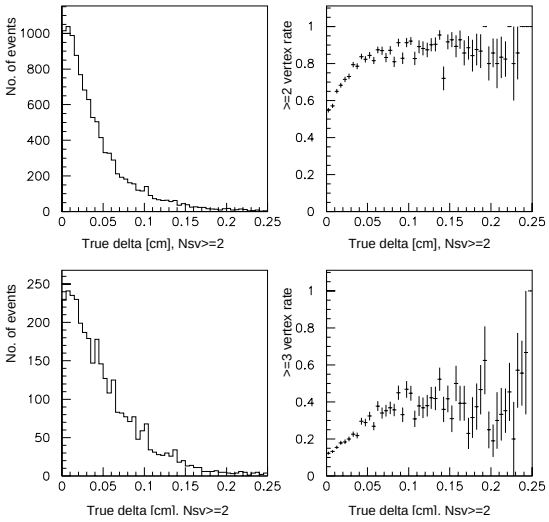

Figure 6.5: Left: The smallest true vertex separation Δ in $2D$ hemispheres with ≥ 2, ≥ 3 found secondary vertices. Right: The corresponding vertex finding rates as a function of Δ.

time. Even when a vertex is in principle visible, the decay kinematics may complicate its detection. Vertices producing only tracks with low P_t with respect to the decaying particle's flight direction are difficult to resolve since these tracks are also likely to be consistent with the decaying particle's parent vertex. For example, a low P_t track produced at the B vertex may also be consistent with the IP. Similarly, a slow pion from a $B \rightarrow D^* X$ decay may be consistent with both the B vertex and with the subsequent D decay vertex. Also, as mentioned previously, 1-prong vertices exhibit particularly poor resolution for off-axis particle decays.

The vertex finding rates do not asymptote to zero either at small true separation because of detector resolution effects leading to the production of mismeasured 'fake' vertices. This vertex overproduction is especially evident in the 2-vertex distribution in figure 6.4 in which multiple vertices are found even for very low true B-D separations below the resolution scale. Mismeasured tracks in these unresolvable vertices cause fake vertices to be formed at larger apparent vertex separations. Similarly, even if the B and the D vertices are resolved, mismeasured tracks in either vertex may cause yet more fake vertices to be formed, giving for example, the non-zero 3-vertex rate in $1D$ decays shown in figure 6.4.

The fake vertices are formed from tracks populating the tails of the track error distribution. For the current analysis, a 3 σ probability cut is used to define vertices. For a Gaussian error distribution, each vertex track would be expected to only have a 0.5% chance of being inconsistent with its true position of origin and possibly forming a fake vertex through its intersection with either the ghost track or with some other real track in the event. However, non-Gaussian tails in the error

distribution lead to much larger rates of fake vertex production. These tails may arise from mis-reconstructed tracks with incorrect detector hits attached, large single scatters for lower momentum tracks, or small detector misalignments affecting mainly higher momentum tracks. The tails in high momentum track error distributions are a particularly serious problem, since these tracks provide most of the short distance vertexing resolution needed to resolve the decay vertex topology.

For any track momentum, fake vertices will appear at distance scales larger than the corresponding 3 σ distance scale characterizing the vertexing resolution. However, it can be expected that the scale of the non-Gaussian error tails are not too much different from that of the Gaussian core of the error distribution since particles with grossly mismeasured detector hits will not survive through the track fit described in appendix C, and will instead contribute to the overall track finding inefficiency. Hence, the 3 σ vertexing resolution scale also roughly characterizes the distance scale for fake vertex production.

The 3-vertex plots in figure 6.4 show fake vertex production in $1D$ decays to be at least a 15% effect at large true separations, and only a 5% effect at small separation where mismeasured tracks are more likely to be attached to pre-existing vertices rather than to form new vertices on their own. However, even in the cases where the correct number of secondary vertices is found, for example, 2 vertices for $1D$ decays and 3 vertices for $2D$ decays, it is not clear from these plots whether every found vertex is real or if fake vertices also contribute to the vertex count.

To summarize, the efficiencies to obtain the expected vertex count in each of the [n]D categories are fairly good, but not perfect, and the problem of overcounts due

to fake vertex production is troublesome. Both of these issues are addressed in the context of the data analysis in chapter 8.

Chapter 7

B tagging

The long decay length of heavy hadrons provides a powerful way to distinguish heavy flavor hadronic events from light flavor events. The daughter particles from the decay of a heavy hadron with boost γ are distributed in a cone of angular size $\alpha \approx 1/\gamma$ (see chapter 5). The decay length is an exponential distribution of characteristic length $\gamma\beta c\tau$, and so the impact parameter distribution of the daughter tracks is roughly exponential with a width $\approx \beta c\tau$. Given sufficiently precise beam position measurements and sufficiently precise track transverse errors:

$$\sigma_{IP},\ \sigma_{track} << \beta c\tau \approx 100 - 500\ \mu\text{m}, \tag{7.1}$$

heavy flavor decay tracks may be separated from the IP with high efficiency. The beam position measurement is described in chapter 4 and yields $\sigma_{IP} \approx 3.2\ \mu$m in the transverse directions and $\approx 20\ \mu$m along the beam, much smaller than the typical

heavy flavor track impact parameter. The track transverse errors are analyzed in chapter 2 where they are shown to be also typically much smaller than the impact parameter scale.

An early method developed to tag heavy flavor decays is therefore to simply count tracks with significant impact parameter to the IP. Because of the differences in lifetimes and decay multiplicities, lower non-zero counts correspond to $c\bar{c}$ events, and higher counts correspond to $b\bar{b}$ events. However, if tracks can be separated from the IP, they may also be intersected to form vertices distinguishable from the IP. There is no advantage in switching from using transverse information in the impact parameter distributions to longitudinal information in the decay length distributions. As is argued in chapter 5, the time dilation factor of γ in the decay length is cancelled by the same factor of $1/\sin\alpha \approx \gamma$ degrading the track resolution. However if sufficiently many of the heavy hadron decay charged tracks can be put into the separated secondary vertex, then extra kinematic information about the decay becomes available.

By making the very good assumption that most tracks from B decays are $\pi^{\pm}$, the summed energy and momentum of all of the vertexed tracks may be calculated. The invariant charged mass may then be defined as:

$$M_{ch} = \sqrt{\left(\sum_i \sqrt{|\vec{p}_i|^2 + m_\pi^2}\right)^2 - \left(\sum_i \vec{p}_i\right)^2} \tag{7.2}$$

This quantity is typically less than the heavy hadron mass because of the missing kinematic information in the neutral daughter particles and in the charged daughter particles which did not get vertexed. For example, charged particles may be

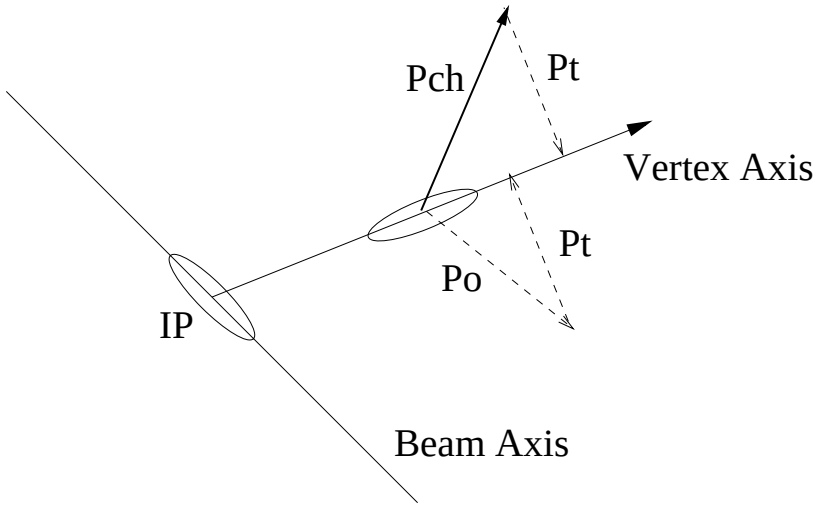

Figure 7.1: The missing P_t due to non-vertexed daughter particles, measured using the resultant charged momentum P_{ch} and the vertex axis.

mistracked, lost to tracking inefficiencies, or swallowed by the IP. In principle, the resultant missing particle kinematics may also be measured, but the SLD calorimeters do not have sufficient segmentation to do this. However, due to conservation of momentum, the Lorentz invariant total transverse momentum of the missing particles is equal and opposite to that of the vertexed charged particles. This fact is shown in figure 7.1. The following inequality may then be derived:

$$M_{ch} \leq \sqrt{{M_{ch}}^2 + {P_t}^2} + P_t \leq M_{true} \tag{7.3}$$

where P_t is the magnitude of the visible (or missing) transverse momentum and M_{true} is the true mass of the decaying heavy hadron. The first inequality is obviously true for any positive semidefinite P_t. The second inequality may be seen by going to the rest frame of the decaying hadron and noting that $M_{true} = E_{true} = E_{ch} + E_{missing}$,

and $\sqrt{{M_{ch}}^2 + {P_t}^2} \leq E_{ch}$ and $P_t \leq E_{missing}$. The 'P_t corrected mass,' defined as

$$M_{Pt} \equiv \sqrt{{M_{ch}}^2 + {P_t}^2} + P_t \tag{7.4}$$

is a much better estimator for M_{true} than just M_{ch}.

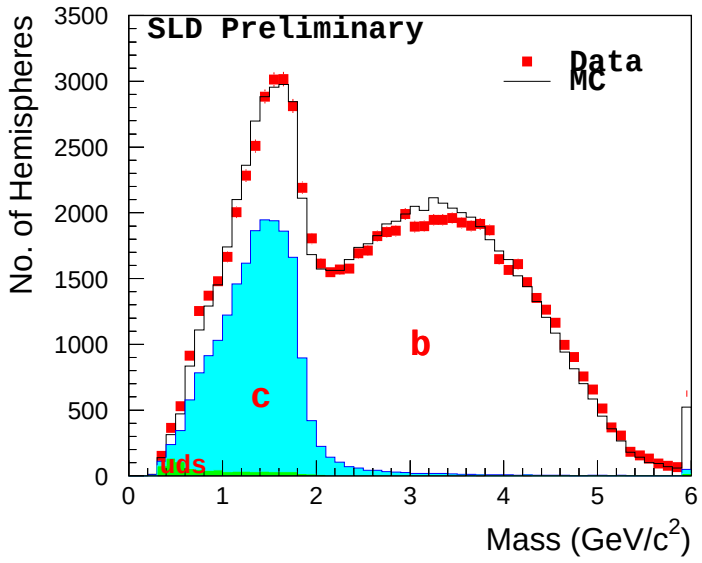

Figure 7.2: The P_t corrected mass, M_{Pt} distribution with contributions shown from uds, c, and b hemispheres.

The distribution of M_{Pt} is shown in figure 7.2, in which the clean separation of uds, c, and b hemispheres can be clearly seen. Further cuts on the vertex momentum may also be used to more cleanly select c decays. The current charm counting analysis employs a neural net B tag (B3MASS) [26] which incorporates the above information along with the vertex flight distance and track multiplicity in order to produce a exceedingly pure sample of B's with high selection efficiency. The neural net has a single output which varies from 0.0 to 1.0, with higher values being more B-like. The

efficiency-purity curve of the tag is shown in figure 7.3 in which a cut on the neural net output is varied.

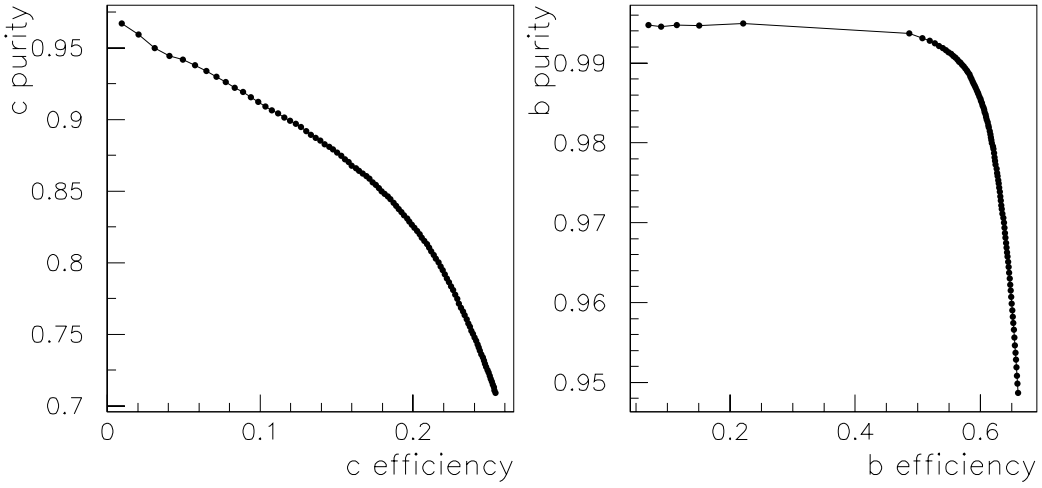

Figure 7.3: The B3MASS neural net tag efficiency-purity curves for c and b tagging.

Since Z^0 decays produce B hadrons in pairs, the B hemisphere tag and double tag rate may be used to simultaneously measure the B tag efficiency, ϵ_b and $R_b \equiv BR(Z^0 \to b\bar{b})/BR(Z^0 \to \text{hadrons})$ if R_c, the $c \to b$ mistag rate ϵ_c, the $uds \to b$ mistag rate ϵ_{uds}, and the hemisphere tag correlation C_b are assumed to be correctly modelled by the MC [27]. The favorable comparison between the B tag efficiency measured in the data and that predicted by the MC is shown in figure 7.4. The current charm counting analysis uses the default cut of 0.75 on the neural net output which corresponds to a B tag with efficiency $\epsilon_b = 61.7\%$ and purity $\Pi_b = 98.3\%$.

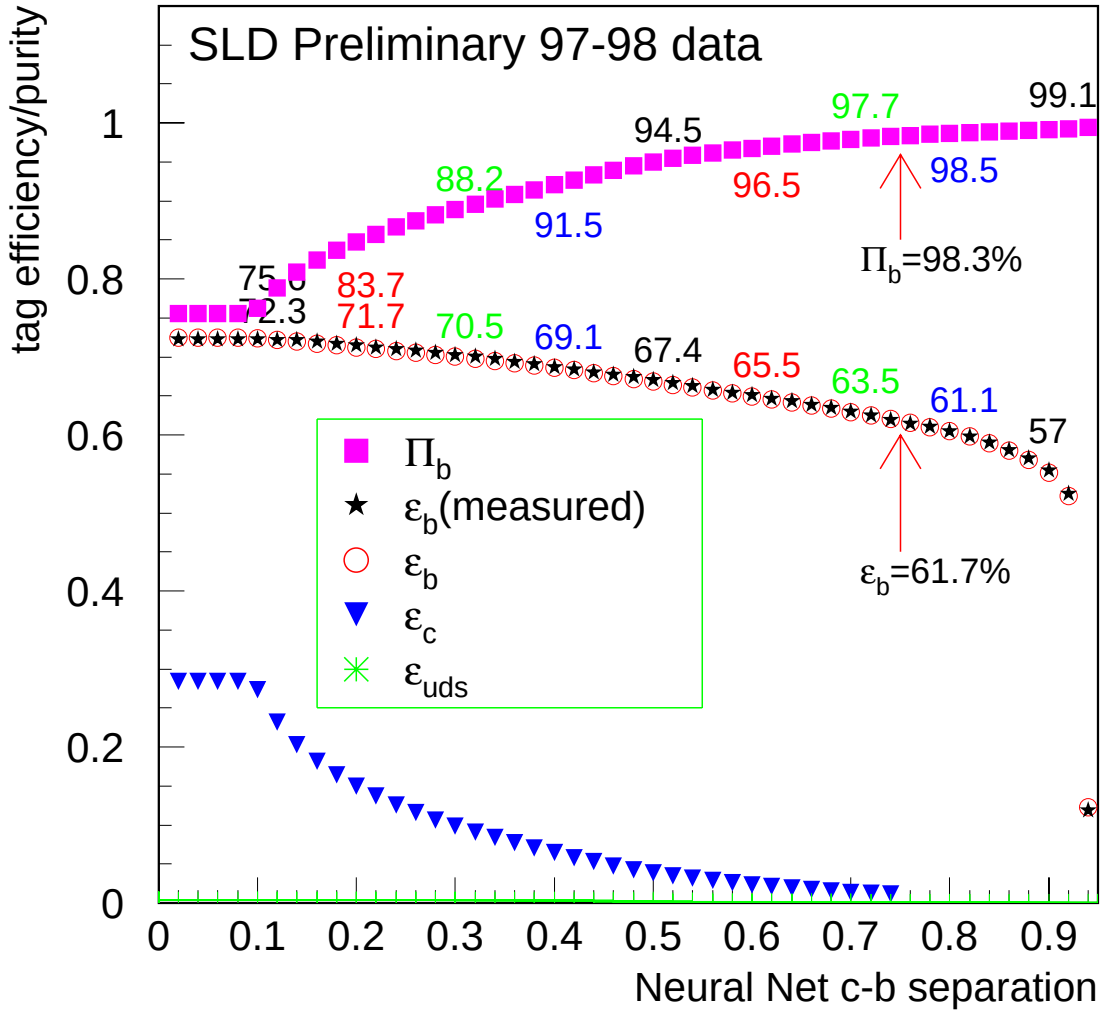

Figure 7.4: Measured B tag efficiency ϵ_b compared with the MC prediction for various values of the B3MASS neural net cut. Also plotted are the predicted mistag rate ϵ_c and the corresponding B tag purity Π_b. (The mistag rate ϵ_{uds} is so small it does not appear on the scale of this plot.)

Chapter 8

The Analysis Procedure

8.1 Event Selection

The first step in the analysis is to get a sample of B decays that are unbiased so that the decay mode composition and kinematics are representative of B decays in general. At the Z^0 pole, the high momentum of the primary quarks leads to the formation of jets of hadronic particles. The jet formed by the b quark and the jet formed by the $\bar{b}$ quark are usually almost back to back as is typical of a two-body decay. Small acolinearities may be caused by another primary parton carrying away momentum in the form of a separate lower energy gluon jet. The Z^0 decay event may then be divided into hemispheres, each hemisphere containing a B hadron which originated from a primary quark. The b and $\bar{b}$ quarks are assumed to fragment independently into hadrons. Due to the large number of degrees of freedom in the fragmentation process, the decays of the resulting B hadrons are assumed to be uncorrelated.

The procedure is first to get a sample of Z^0 hadronic decay events which are identified through jet energy deposition in the calorimeter and through detection of multiple jet tracks in the tracking chambers. Event cuts are made requiring a minimum visible energy of 18 GeV and at least 7 tracks consistent with coming from the IR. Furthermore, to obtain events well contained within the detector, a thrust axis angle $|\cos\theta| < 0.8$ is required. Using these cuts, about 250,000 hadronic Z^0 decays are selected. The requirement of multiple tracks may introduce a small bias in the event selection since very low multiplicity B decays may be rejected. However the coincidence of low fragmentation multiplicity in both hemispheres along with low B decay multiplicity again in both hemispheres is presumably a very low probability occurrence, and so the multiplicity bias on the B sample is believed to be negligible.

A neural net B-tag (see chapter 7) is performed separately in each hadronic event hemisphere. Since the B-tag is highly correlated with long decay length and with large track multiplicity, a sample of tagged hemisphere is unlikely to be representative of B decays in general. However, since b quarks and $\bar{b}$ quarks are produced in pairs, a positive tag in either hemisphere suffices to identify the event as a $b\bar{b}$ event. Assuming that the two B hadrons decay independently, the hemisphere opposite a tagged hemisphere is then completely unbiased in proper decay time, decay mode kinematics and particle multiplicity. In effect, the opposite hemisphere is tagged as containing a B hadron decay without actually using any information from that hemisphere. The same unbiased tagging argument applies to a positive tag in either hemisphere, so if both hemispheres are tagged, then each is unbiased by virtue of being the hemisphere opposite a tagged hemisphere. Altogether, a sample of 62,000 B decay hemispheres

is obtained in this way.

8.2 Vertex Counting

To find topological vertices, the ZVTOP3 'ghost' algorithm (described in chapter 6) is applied to the sample of 'opposite hemisphere tagged' B decay hemispheres, both in the data sample and in the MC. A vertex χ^2 probability (confidence level) cut of 0.5% is used to define vertices, and the 'tidy' option is used to find and remove K_s, Λ and gamma conversion vertices. For the MC, the vertex count distribution is generated separately for each of the [n]D B decay topologies as well as for the *udsc* background. The details of the MC modelling of each of the [n]D topologies is described in appendix B.

The SLD MC predicted vertex count distributions are shown in figure 8.1. The $0D$ distribution shown is modelled with a set of tabulated $b \to (c\bar{c})$ decays and is strongly peaked in the 1-vertex bin. Modelling the distribution with $b \to u$ or $b \to s$ decays gives a similar peak. A non-negligible fake vertex production rate of about 20% is also seen. The $1D$ distribution is modelled using a combination of tabulated modes and quark decay models. This distribution shows the same large efficiency as in the $0D$ distribution for separating the heavy flavor decay vertices from the IP. Furthermore, both the 'B' and the 'D' vertex are reconstructed about 50% of the time and the fake vertex rate is about 10%. The $2D$ distribution is modelled using a set of tabulated modes based on CLEO measurements. This distribution shows a low efficiency for reconstructing all three vertices, but a much higher efficiency for

reconstructing at least two vertices compared with the $1D$ distribution. It is difficult to estimate at this stage how many fake vertices populate the 3-vertex bin based on the 2D plot alone. Also plotted is the found secondary vertex count for the *udsc* background which leaks through the B tag. The shorter charm decay length and low average charged particle multiplicity results in a low rate of finding secondary vertices.

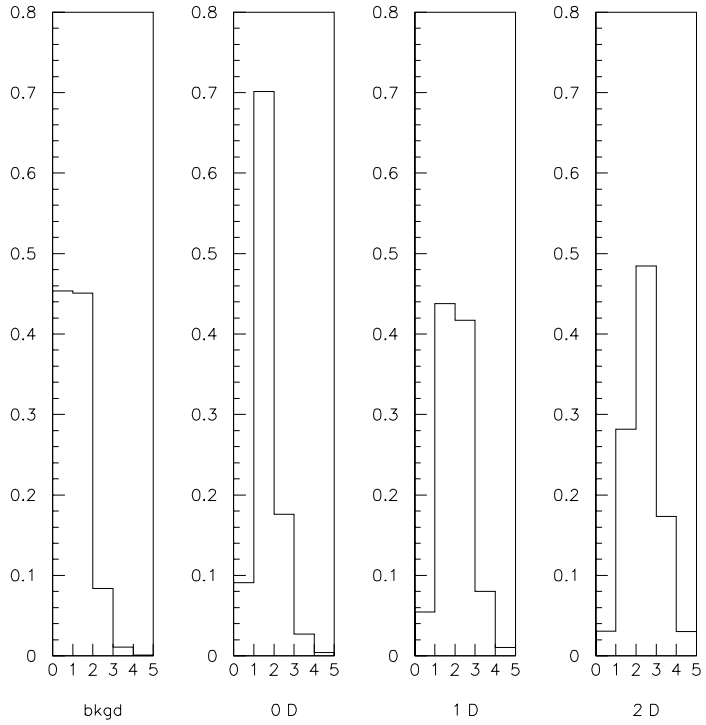

Figure 8.1: MC predicted found secondary vertex count. Each histogram has been normalized to unit weight.

These predicted distributions are different enough that they contain significant analyzing power in unfolding the data distribution. However, they are also similar

enough such that small changes in the shapes of the distributions may cause large systematic effects in the measurement. To try to minimize our susceptibility to such systematic effects, we can require that the vertices being counted are found in the correct places, so that the MC predicted vertex position distributions match the vertex position distributions in the data. Such a requirement would ensure that the vertices being counted in the MC are the same vertices being counted in the data.

8.3 The Vertex Separation Distributions

Physically, we would expect the found vertices to appear at several distinct distance scales. True heavy flavor decay vertices would of course appear at the appropriate decay length scales discussed before. However, these distributions would be truncated at short decay lengths due to finite vertexing resolution. The scale for this truncation is set by the track momentum and angular distributions, and the corresponding tracking resolution. For fake vertices formed by tails in the track measurement error distribution, the distance scale is set by the tail width. However, as argued in chapter 6, most of the tail population presumably lies very close to the distance scale set by the 3 σ χ^2 probability criterion used for defining vertices. Therefore, the appropriate scale for fake tail vertices can be approximated by the momentum-dependent vertexing resolution scale of $\sim 100 - 500$ μm.

We could plot the vertex position distributions and examine them by eye to check that we are not overcounting or undercounting vertices in any region. Even better, we can incorporate the vertex position distributions in a fit of the data to the predicted

distributions. Each bin in the vertex count distribution can now be viewed as having a set of vertex position distributions hidden behind it. The 1-vtx bin has the IP to vtx_1 separation, the 2-vtx bin has the IP to vtx_1 separation and the vtx_1 to vtx_2 separation, etc. These distributions are shown in figures 8.2 and 8.3 and are discussed further below.

The MC predicted distributions of found vertices are generated using a MC sample with $\sim$ 25 times the statistics of data. These distributions are shown in figure 8.2 for the IP to vertex 1 separation and in figure 8.3 for the nearest neighbor secondary vertex separations. The distributions are plotted separately for the true topological categories: *udsc* background, $0D$, $1D$, $2D$, and also versus the apparent topological categories: N_{sv} = 1, 2, 3, $\geq$4. The nearest neighbor secondary vertex separation plots are all very similar, each containing the D decay length scale and the cutoff at the resolution scale. Therefore, if there is more than one secondary vertex separation to be plotted in a decay hemisphere, all are histogrammed in the same plot. For example, in the N_{sv}=3 category, both the vertex 1 to vertex 2 separation and the vertex 2 to vertex 3 separation are put in the same histogram. The histograms are binned in constant logarithmic intervals in order to produce a higher sampling rate at the shorter vertex resolution scale of interest, and a lower sampling rate at the longer decay length scale which is mainly used for normalization. The histograms are labelled with two indices, the first denoting the topological category (B,0,1,2), and the second giving the total secondary vertex count. For example 'B2' refers to the sample of true *udsc* background hemispheres in which two secondary vertices were found.

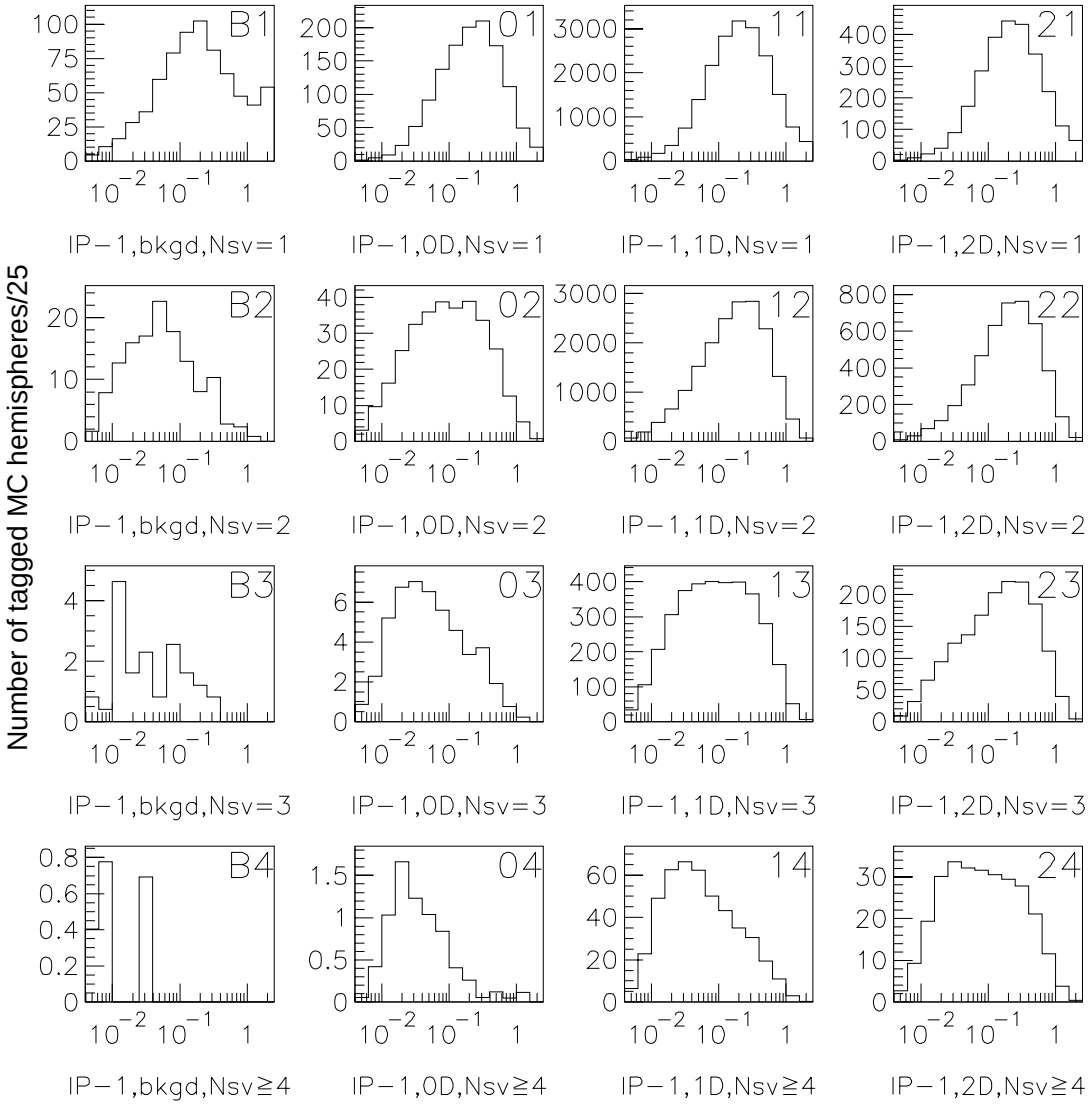

Figure 8.2: MC predicted IP-vertex 1 separations (cm) on a log scale. The rows represent N_{sv}=1,2,3,$\geq$4, and the columns represent *udsc* background, $0D$, $1D$, and $2D$. The histograms have been normalized to a data-sized sample.

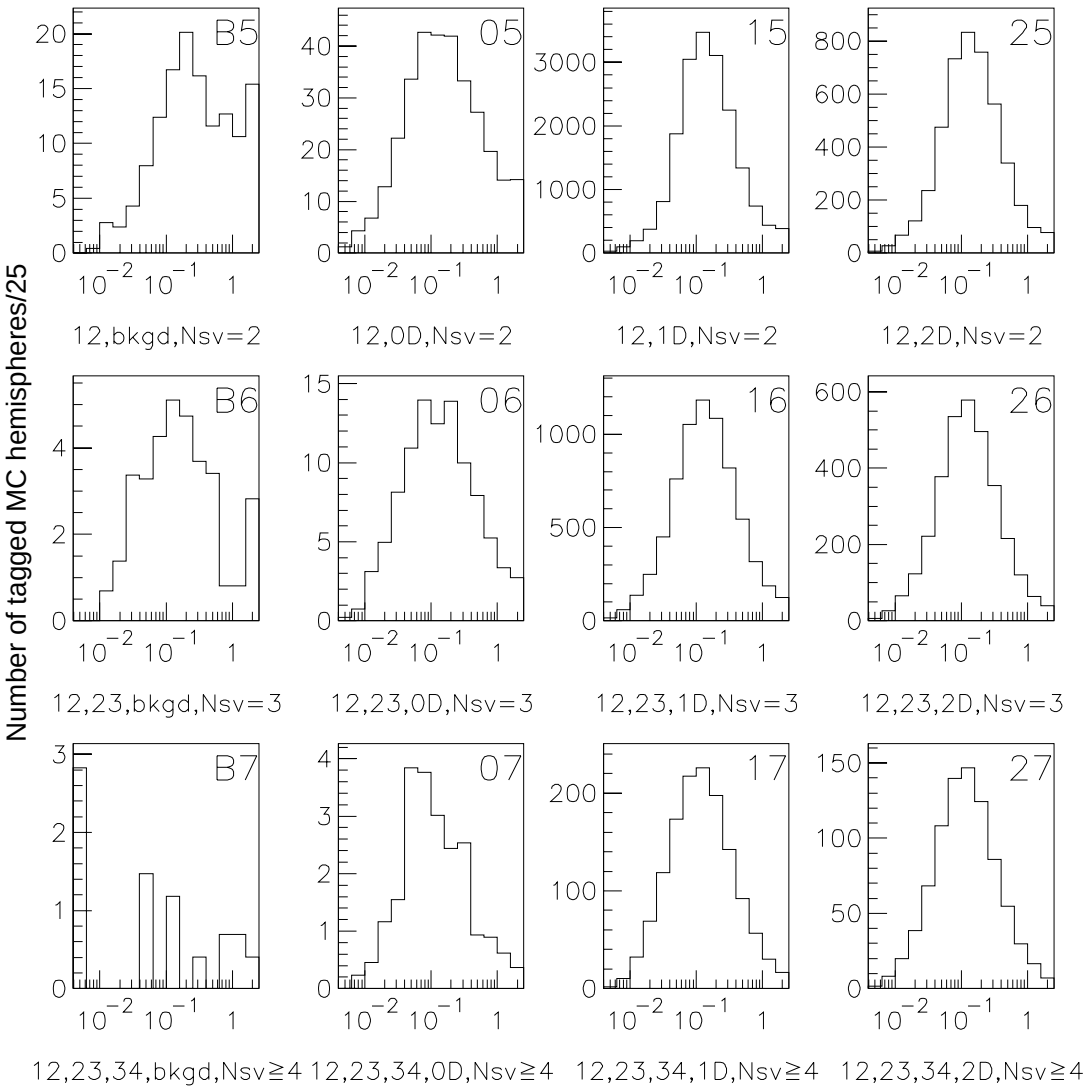

Figure 8.3: MC predicted nearest neighbor vertex separations (cm) on a log scale. The rows represent N_{sv}=2,3,≥4, and the columns represent *udsc* background, $0D$, $1D$, and $2D$. In the cases of N_{sv}=3 or 4, all nearest neighbor separations are histogrammed in the same plot. The histograms have been normalized to a data sized sample.

By looking at the histograms on a logarithmic scale, the emergence of fake vertices with increasing N_{sv} becomes apparent. As the number of found secondary vertices increases, relatively more vertices appear at the 500-1000 μm separation scale than at the decay length scales greater than 1 mm, even in the categories where there really are no more true vertices to find. For example, since $1D$ decays contain at most two true vertices, histogram 13 contains at least one fake vertex and 14 contains at least 2 fake vertices. The balance between the resolution scale and the decay length scale is also seen for $2D$ decays in plots 21-24. The nearest neighbor plots 15-17, and 26-27 show these features to a lesser extent.

To create the MC predicted shapes, a set of four histograms (e.g. B1-B4, 11-14, 21-24, 31-34) for each true topological category are appended together with an extra bin for the N_{sv}=0 count. This set of bins is then projected into a vector and normalized by the number of true decays of that category that was used in creating the histograms. The resulting distribution shapes are shown in figure 8.4. These shapes still contain the same information as the vertex count shapes in figure refF:mcvtxcnt but now extra information about the vertexing resolution and the fake vertex production rate is made available through the measurement of the IP-'B' separation. The data can then be fit bin-by-bin to the predicted shapes for each category.

In principle, the nearest neighbor secondary vertex distributions (B5-B7, 15-17, 25-27, 35-37) contain extra vertexing resolution information and could be used in a similar fashion in creating a set of shape functions. However, the statistics of using this new set of fitting functions is not correct, since for n secondary vertices plus the IP, there are n vertex separation distributions to be plotted. The n-vtx bin therefore

effectively gets weighted n times in the vertex count distribution. The correct way to include all of the information is to make a n-dimensional histogram with independent pieces of information on orthogonal axes. This way, each B decay in the sample is only put into a single bin. However, this procedure is not feasible since the MC sample is not sufficiently large to create well-modelled multi-dimensional shape predictions. Instead, the information from the nearest secondary vertex separations is rejected. Not much is lost since these histogram shapes do not contain much differentiating power anyway.

8.4 The Fit

The three inclusive branching ratios are measured simultaneously along with the *udsc* background in the B-tag by doing a simultaneous fit of every vertex separation distribution in the data to a linear combination of the set of distributions predicted by MC simulation. The fitting function used is:

$$F^i_{data} = R_n \cdot [(1-R_{bkgd}) \cdot [BR_{0D} \cdot F^i_{0D} + (1-BR_{0D}-BR_{2D}) \cdot F^i_{1D} + BR_{2D} \cdot F^i_{2D}] + R_{bkgd} \cdot F^i_{bkgd}] \tag{8.1}$$

where $F_{0D}, F_{1D}, F_{2D}, F_{bkgd}$ are the four normalized MC distributions, and i = $\{1..57\}$ is the bin number. The parameters extracted from the fit are normalization R_n, the *udsc* background fraction R_{bkgd} in the B tag and the branching ratios BR_{0D}, BR_{2D}. BR_{1D} has been eliminated to impose the constraint that the branching fractions sum to unity.

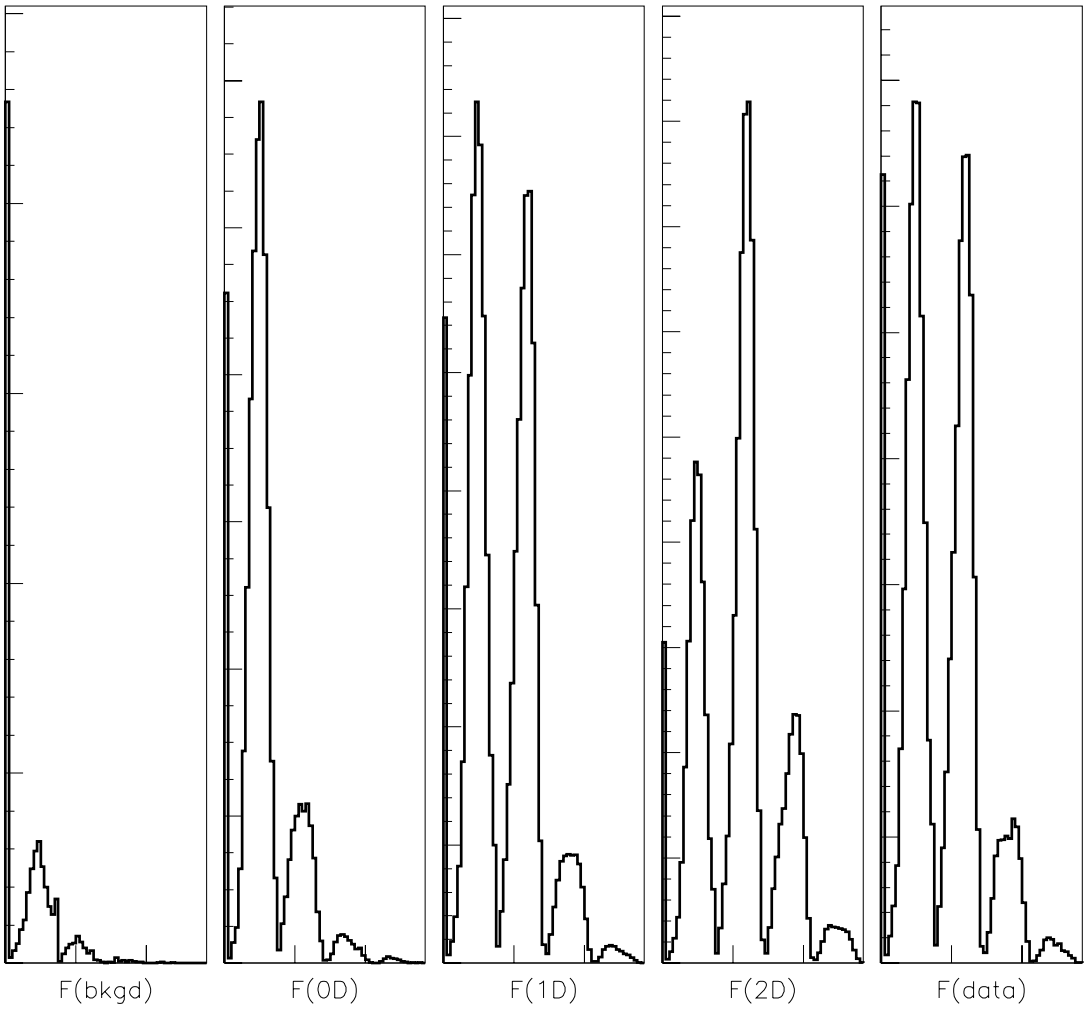

Figure 8.4: Binned distribution shapes for each of the MC decay categories and the distribution shape seen in the data. The horizontal axis represents the bin number. The bin content is: bin $1 \equiv N_{sv} = 0$ count; bins $2..57 \equiv IP - B$ separations for $N_{sv} = 1, 2, 3, 4$ (14 bins each). The vertical scale is arbitrary.

The results of the fit are plotted in figure 8.5. Plots (a)-(d) show the fitted IP-vertex 1 separation distributions for $N_{sv} = 1, 2, 3, 4$. Plot (e) shows the fitted $N_{sv} = 0$ count as well as the other N_{sv} bins which are also effectively fitted by virtue of the fit to the normalizations of plots (a)-(d). Plots (f)-(h) are the nearest neighbor secondary vertex separations which are not included in the fit, but appear to be well-matched nonetheless. The χ^2/d.o.f. of the fit is about 1.6. There remains a small apparent discrepancy for all of the distance plots for the few bins in the middle of the vertex resolution scale, around 200-400 microns, indicating that the B decay model does not predict exactly the correct kinematics. The shorter distance end of the vertex resolution scale is well matched, indicating that the detector alignment modelling is good. The measured *udsc* background level of $(2.8 \pm 0.3)\%$ is consistent with expectations of a high B tagging purity. The fit gives:

$$\begin{aligned} BR_{0D} &= (3.7 \pm 1.1)\% \\ BR_{2D} &= (17.9 \pm 1.4)\% \end{aligned} \tag{8.2}$$

with a error correlation coefficient of $C_{0D,2D} = 0.702$. Varying the data and MC histogram binning gives negligible changes to these results.

8.5 Using MC as Data

To make sure that the measurement procedure does not give any systematic biases to the results, measurements are made on a set of 15 data-sized samples of $B\bar{B}$ MC. The

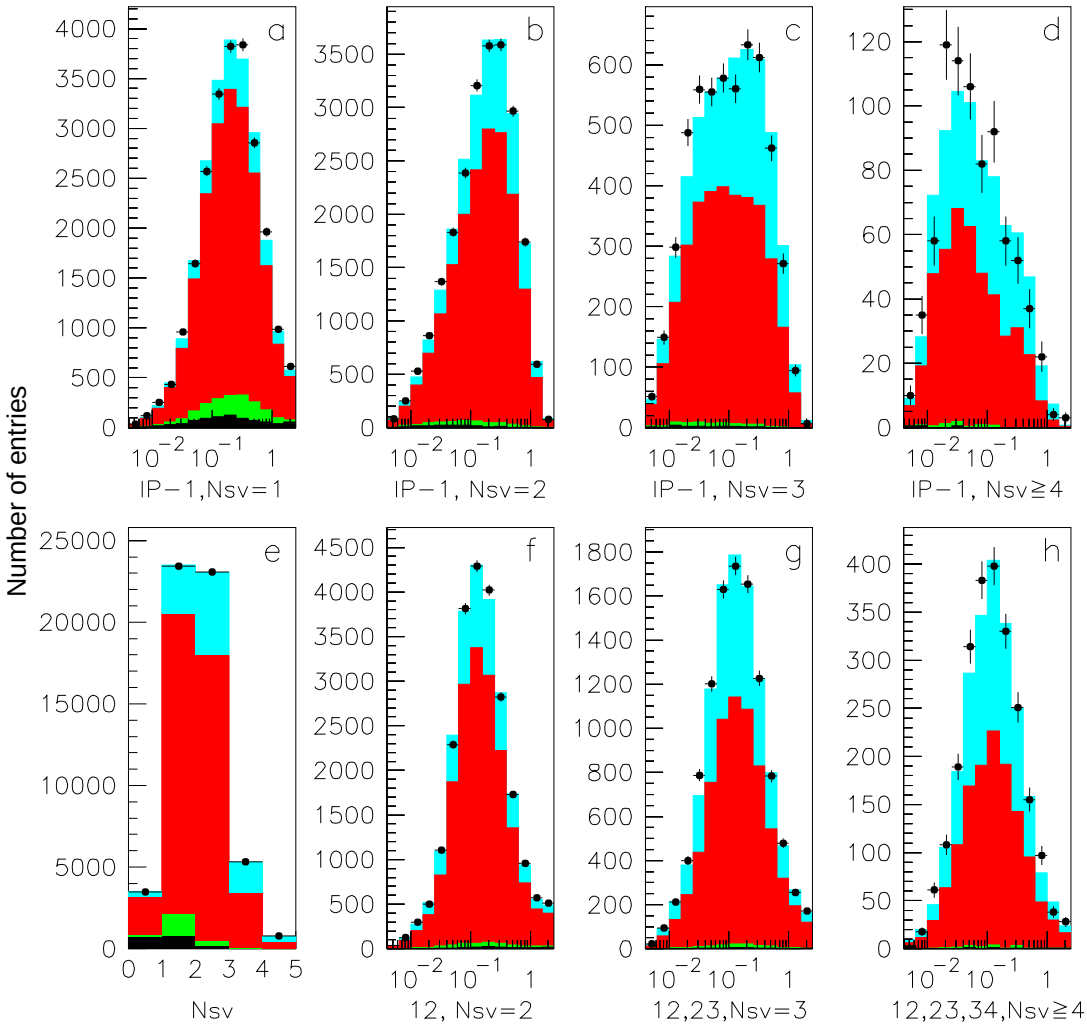

Figure 8.5: Fit results on a log scale. The stacked MC histograms are from bottom to top: *udsc* background, $0D$, $1D$, and $2D$. (a)-(d) show the IP to vertex 1 separation [cm], (f)-(h) shows the nearest neighbor vertex separations [cm], and (e) shows the resulting match in the vertex count distribution.

MC shape distributions used in the fitting function are derived from an independent unweighted MC sample with ten times the statistics of the data sample in order to minimize statistical fluctuations in the fitting function. The true MC sample fractions are $BR_{0D} = 2.3\%$ and $BR_{2D} = 17.7\%$. The means of the 15 measurements are $BR_{0D} = (2.4 \pm 0.3)\%$ and $BR_{2D} = (18.0 \pm 0.4)\%$. There is no evidence for any systematic bias in the method. The RMS scatter of the 15 measurements gives an empirical check of the statistical errors calculated in the fit. The measured RMS deviations of $\Delta_{0D} = (1.0 \pm 0.1)\%$ and $\Delta_{2D} = (1.5 \pm 0.2)\%$ are consistent with the fit statistical errors in equation 8.2. An example of one of the fitted MC-as-data distributions is shown in figure 8.6. The χ^2/dof is typically close to 1.0, indicating that the statistics of the fit is behaving as expected.

8.6 Crosscheck with tagged leptons

The results of the analysis may be cross-checked by experimentally varying the composition of the data sample being measured. This can be done by finding some other measureable quantity which is sensitive to the inclusive branching fractions. One such quantity is the momentum of leptons produced in B decays. As shown in figure B.4, due to the larger available phase space, prompt B leptons have a harder momentum spectrum than leptons from the cascade D decay. When the decay is boosted into the lab frame, the Lorentz invariant transverse momentum still exhibits this separation as shown in the first plot in figure 8.7. Because in $2D$ decays, the virtual W bosons must decay to charm and strange quarks, they are unable to produce prompt

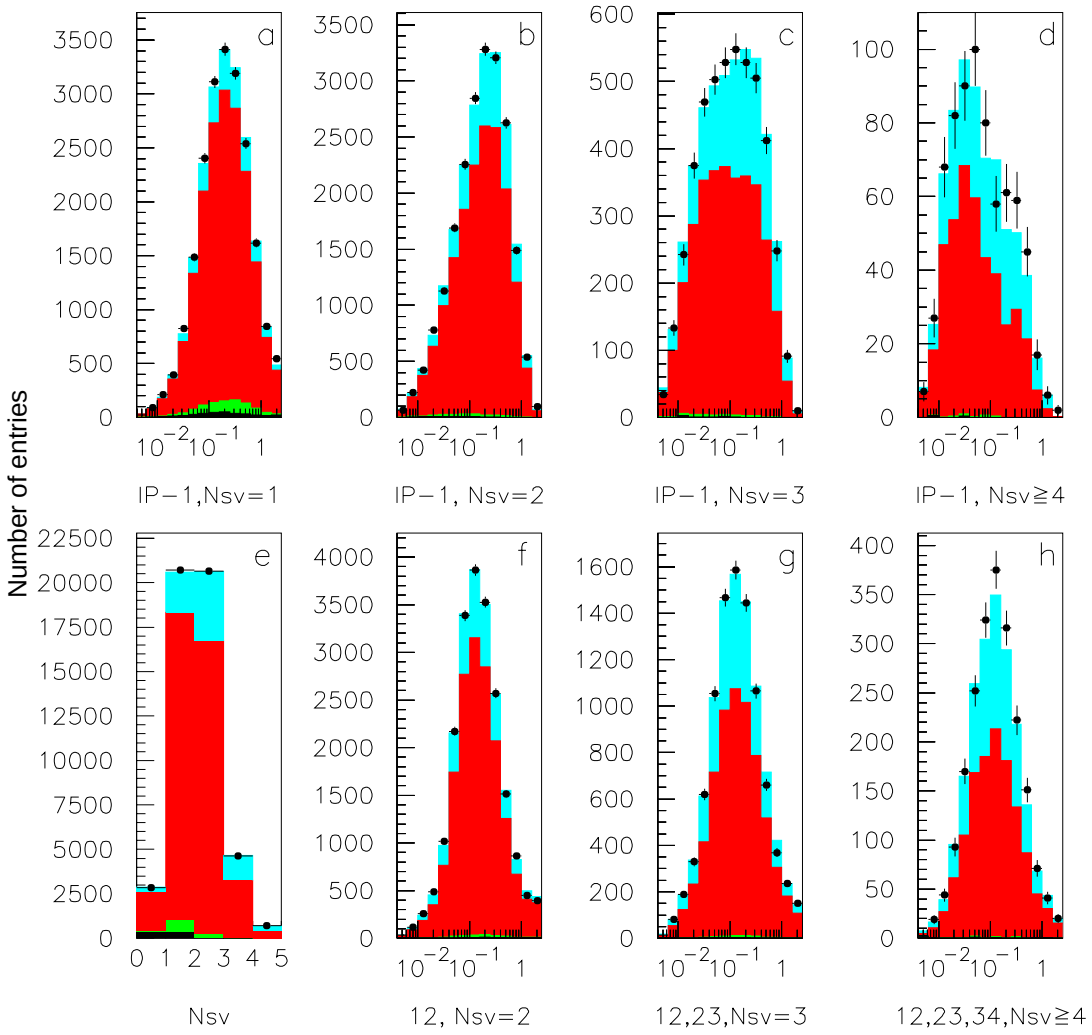

Figure 8.6: MC-as-data fit results on a log scale. The stacked MC histograms are from bottom to top: *udsc* background, $0D$, $1D$, and $2D$. (a)-(d) show the IP to vertex 1 separation [cm], (f)-(h) shows the nearest neighbor vertex separations [cm], and (e) shows the resulting match in the vertex count distribution.

B leptons. The only leptons in $2D$ decays are therefore from decays of the D's, and the lepton momenta are distributed at lower values of P_t as shown in the second plot in figure 8.7.

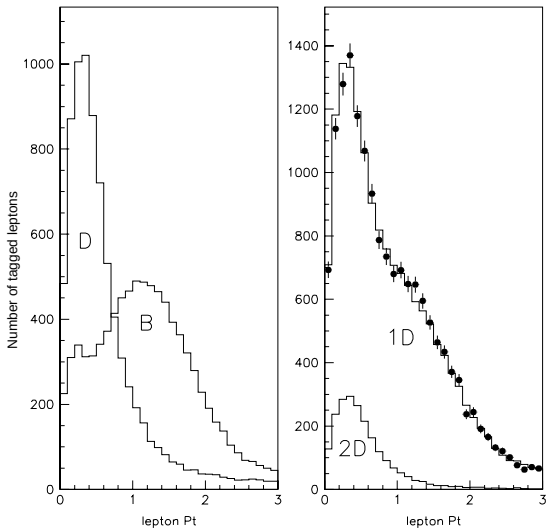

Figure 8.7: Left: Measured P_t (GeV/c) for tagged leptons in the MC. Prompt B leptons are distributed at higher P_t than the softer D decay leptons. Right: Measured P_t for tagged leptons in $1D$ decays and $2D$ decays. The cumulative MC distribution shape is compared with the tagged lepton distribution in the data (points). The MC/data comparison plot has been normalized to the number of tagged leptons in order to remove a possible small ($< 10\%$) mismatch in the lepton tagging efficiency normalization.

These plots contain $e^{\pm}$ tagged with showers in the innermost calorimeter (the electromagnetic section of the liquid argon calorimeter), and $\mu^{\pm}$ tagged with hits in the outermost calorimeter (the warm iron calorimeter). The vertex/ghost axis is used as an estimator for the B flight direction in order to calculate the lepton transverse momentum. The high P_t tails in the distributions are presumably due to errors in this flight direction estimator.

The lepton tagging procedures are described in [28]. According to MC modelling, the electron tagging efficiency is flat in momentum above 2 GeV/c and averages $\sim 62\%$. The electron tagging purity has been measured using pions from K_s^0 decays to be $\sim 70\%$. The muon tag has an efficiency is $\sim 81\%$ and a purity of $\sim 68\%$ above 2 GeV/c according to the MC. Calibrations of these lepton tags are difficult to do, but for the present purposes, the main concern is that the efficiencies are flat in momentum so that the tagged lepton momentum spectrum does not get distorted. The comparison between the cumulative MC tagged lepton distribution and the tagged lepton distribution in the data in figure 8.7 indicates a fairly good match between the distributions.

The B decay sample fractions of the different decay categories may be varied by requiring the measured P_t of tagged leptons to be greater than some minimum value. By moving this cut around, the sample fractions may be continuously changed. For example, most of the the $2D$ decays may be removed by requiring a high P_t tagged lepton in each decay event in the sample.

Assuming that the B and D semileptonic decays and the D energy distributions are correctly modelled, then for any value of the P_t cut, the MC should still make a reliable prediction for the vertex separation distributions, provided that the same lepton P_t cut is used in generating both the data distributions and the MC distributions. The measurement technique may then be used to measure the decay type fractions in the biased data sample. The results of repeated measurements with various minimum P_t cuts is shown in figure 8.8. These results are shown compared with the biased fractions predicted by the MC. The predicted drop in the $2D$ fraction with increasing P_t

cut is observed in the data, thus showing that the measurement procedure is working. An example of the results of the a new fit in which the data sample has been biased to be mostly $1D$ is shown in figure 8.9. This plot indicates that the vertex separation distribution shapes are being modelled correctly for the semileptonic decays in the $1D$ sector, both at the smaller resolution scale and the larger decay length scale. In particular, figure 8.9(e) shows that, in a well-understood category of B decays, the MC detector modelling produces the correct number of fake vertices.

8.7 Crosscheck with vertex charge

Another check on the MC modelling is to make the measurement separately for a charged B sample and for a neutral B sample. With the assumption of local quark-hadron duality, the [n]D rates are predicted to be independent of the spectator quarks and thus independent of the charge of the B hadron. In order for the measurements on the two samples to coincide, the MC modelling must be done correctly both for the charged B sector and for the neutral B sector. A fundamental limitation of this technique is that any method used to measure the charge of the B hadron will undoubtedly introduce biases in the [n]D composition of the resulting charge-tagged samples. These biases can only be estimated from MC studies.

The B3MASS B tagging package described in chapter 7 offers a natural way of measuring the B hadron charge by simply summing the charges of the tracks put in the secondary vertices [26]. This charge sum is further improved by including track fragments called 'VXD3 vectors' which have good position and direction resolution

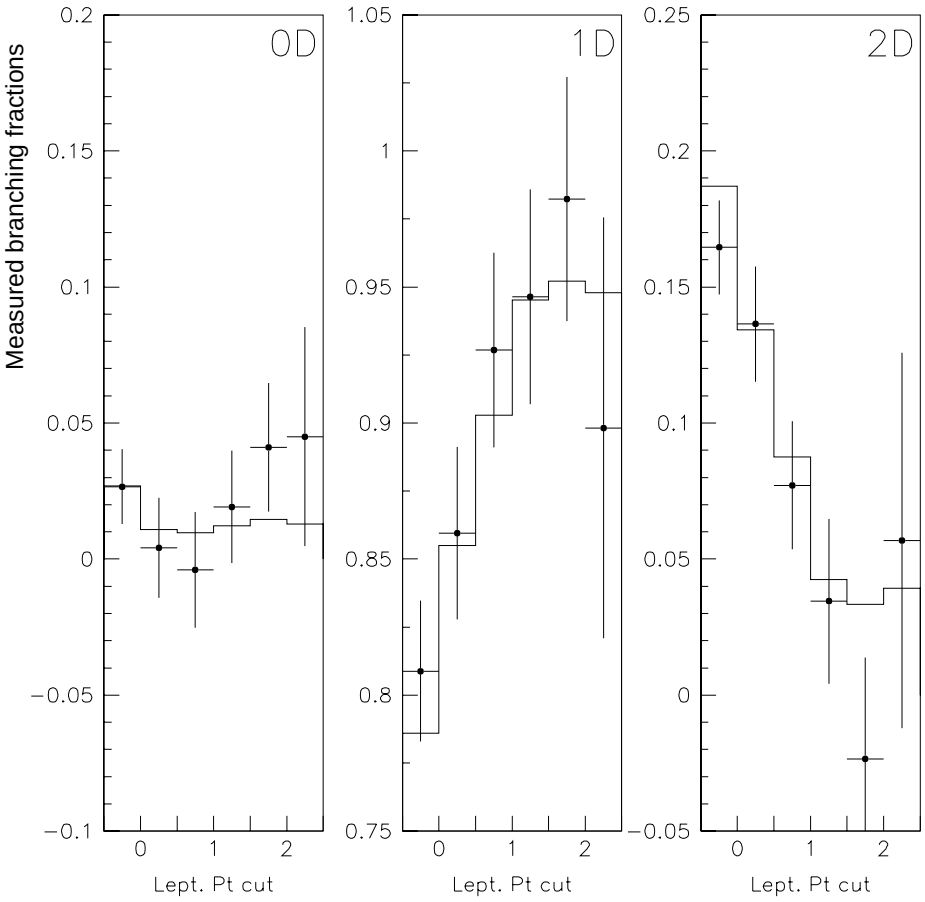

Figure 8.8: Measured inclusive fractions as a function of the tagged lepton minimum P_t cut (in GeV/c). Data measurements (points) are compared with the MC predicted fractions (histogram). The $\min(P_t) < 0$ bin represents the sample of decays with no tagged leptons, and the $\min(P_t) = 0$ bin represents the sample of decays with at least one tagged lepton of any P_t

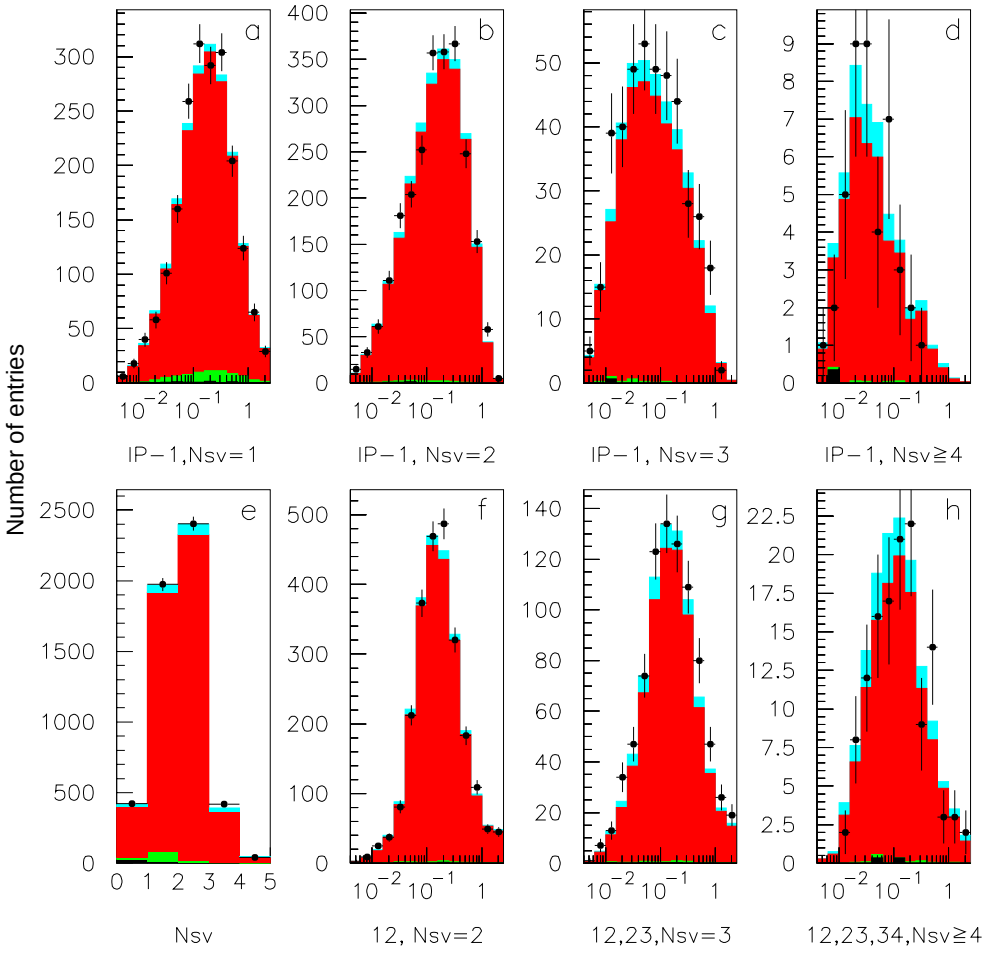

Figure 8.9: An example of the fit giving one of the measurements plotted in figure 8.8. Here, a minimum lepton P_t of 1.0 GeV/c is required, thereby biasing the data sample to be mostly $1D$ semileptonic decays

from vertex detector hits but did not get associated with drift chamber hits due to inefficiencies in the tracking algorithms. When these track fragments are constrained to go through the B3MASS secondary vertex, they are able to provide reliable track charge information. The measured vertex charge Q is shown in figure 8.10 for the data and the contributions from different sources as modelled by the MC.

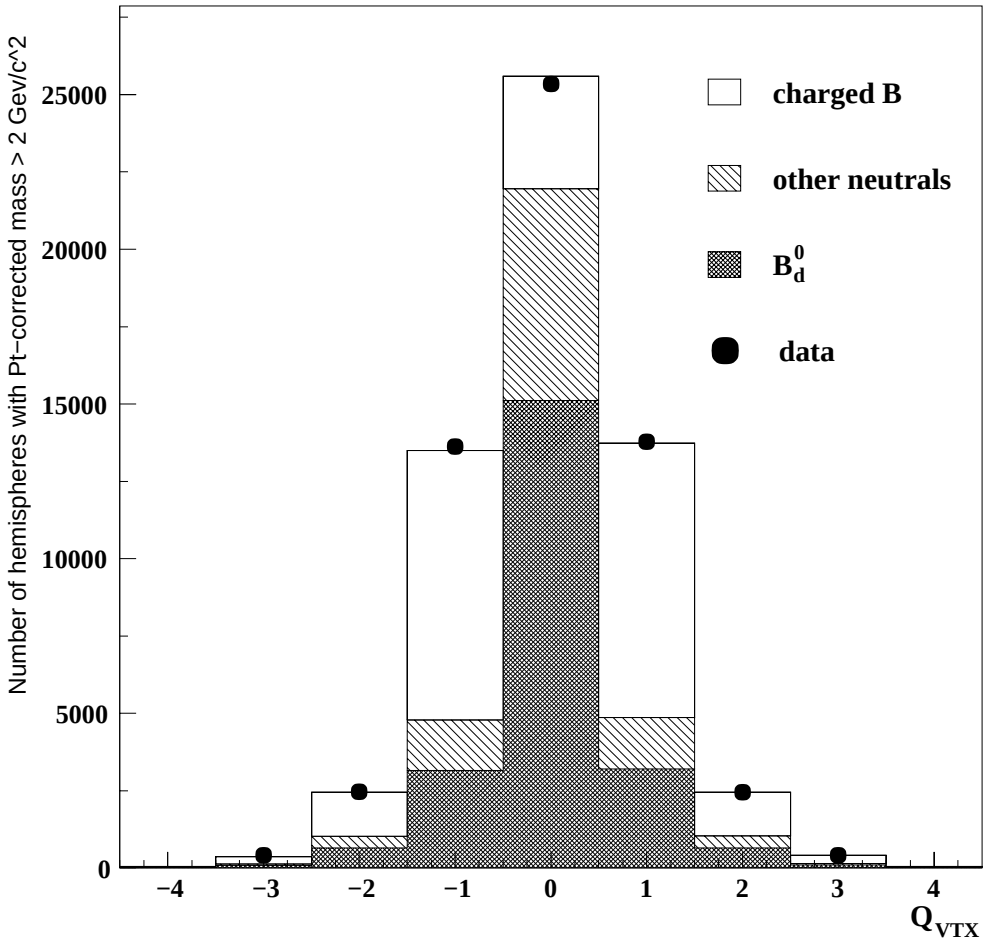

Figure 8.10: The measured vertex charge using fully reconstructed tracks and VXD3 vectors attached to the B3MASS secondary vertex.

The high vertex charge purity of this technique requires using only decay hemi-

More variations of the sample composition

Sample type	MC true BR_{0D}	MC true BR_{2D}	Data BR_{0D}	Data BR_{2D}
Unbiased	2.3%	17.4%	$(2.9 \pm 1.1)\%$	$(17.1 \pm 1.3)\%$
$M_{Pt} \geq 2$ GeV	2.3%	18.5%	$(3.7 \pm 1.0)\%$	$(19.8 \pm 1.5)\%$
$Q = 0$	2.3%	18.0%	$(3.2 \pm 1.3)\%$	$(17.0 \pm 2.1)\%$
$Q \neq 0$	2.3%	18.9%	$(3.4 \pm 1.3)\%$	$(19.1 \pm 2.1)\%$

Table 8.1: MC predicted sample biases for various samples and the corresponding data measurements for various sample cuts.

spheres containing a vertex with Pt-corrected vertex mass $M_{Pt} > 2$ GeV/c^2 in order to reject hemispheres likely to have missing charged tracks. This requirement biases the B decay sample composition towards higher charged multiplicity decays however. Further model-dependent biases are introduced in creating $Q = 0$ and $Q \neq 0$ samples. The biased MC fractions and the results of the fits to the biased data sample are shown in table 8.1. The MC predicted sample biases between the $Q = 0$ sample and the $Q \neq 0$ sample are smaller than the data measurement statistical errors, so it cannot be concluded that the biases are being modelled correctly. However, the $Q = 0$ and $Q \neq 0$ measurements are consistent with each other, so there is no evidence of any problems with the MC modelling or with the local quark-hadron duality assumption. The separate fits to the $Q = 0$ and $Q \neq 0$ samples are shown in figures 8.11 and 8.12. No problems are seen with the modelling of either sector.

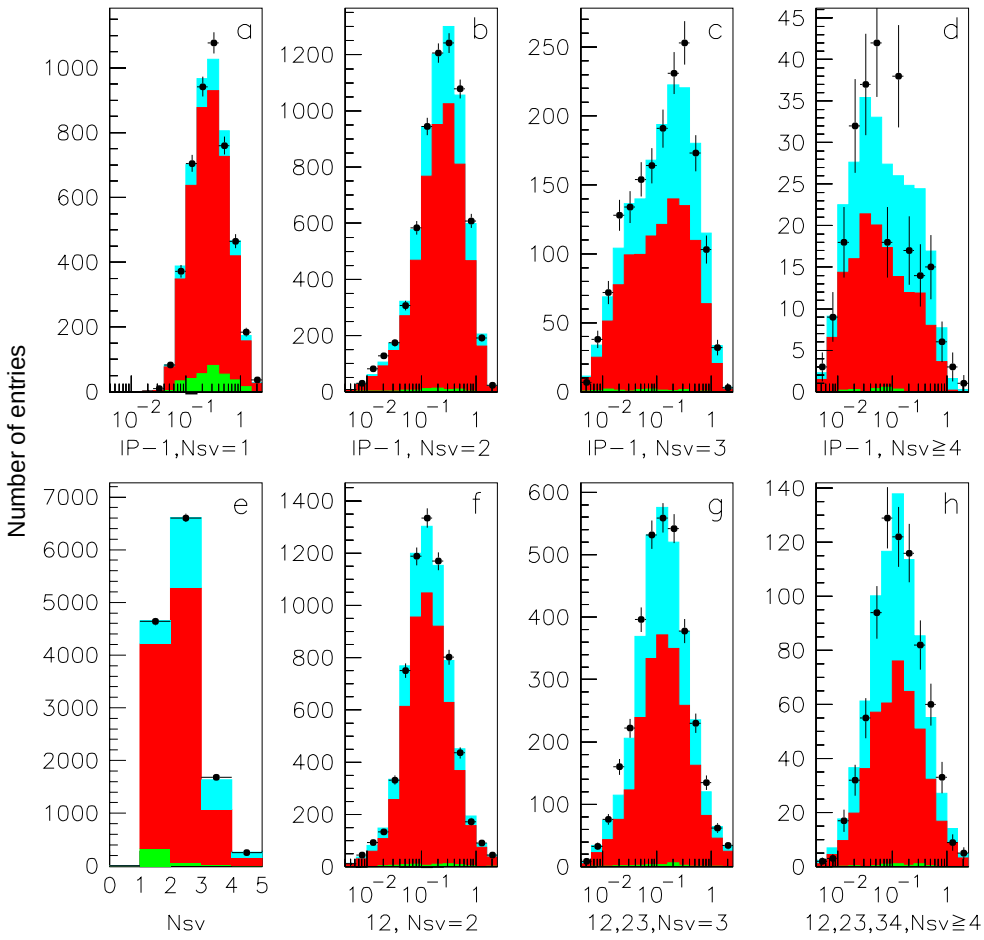

Figure 8.11: The fit results using data and MC distributions with $M_{Pt} > 2.0$ GeV/C^2 and $Q = 0$

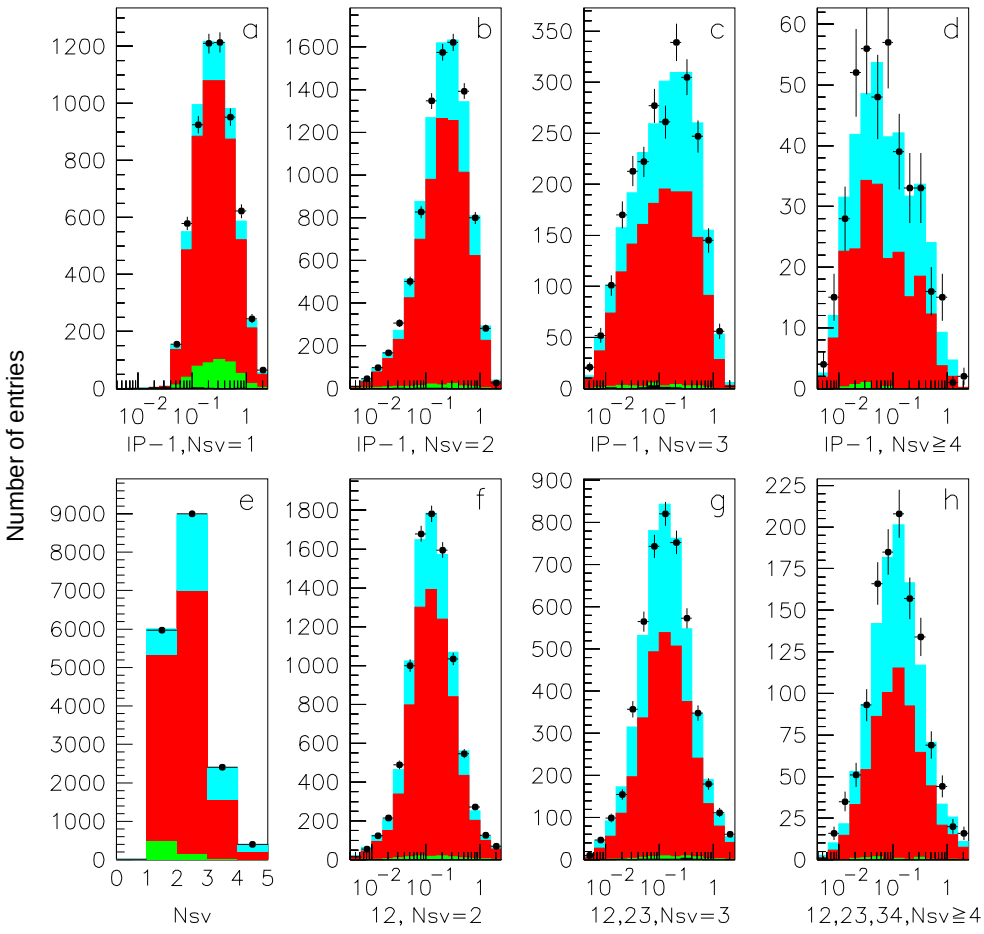

Figure 8.12: The fit results using data and MC distributions with $M_{Pt} > 2.0$ GeV/C^2 and $Q \neq 0$

Chapter 9

Systematic Errors

The main systematic uncertainties in this analysis are those affecting the MC predicted vertex count for each of the decay types. These can be separated into two categories: the uncertainties due to detector modelling, and the uncertainties due to physics modelling. The results of the systematic errors analysis discussed here are tabulated at the end of the chapter.

9.1 Detector Effects

The detector resolution controls the ability to separate and count vertices. As discussed in chapter 6, tails in the resolution distribution lead to the production of fake vertices and a resulting overcount. Ideally, the shape of the resolution function and its cut-off at low vertex separation should be exactly matched between data and MC to give a good model of the vertex count. In practice, this goal is impossible because

of a lack of perfect knowledge of B decay physics, particularly of the daughter particle kinematics at each vertex. Using a phenomenological B decay model in the MC gives reasonable results however, as shown in the fit to the vertex separation distributions, figure 8.5 in chapter 8. The short distance resolution given by high momentum tracks is well-matched between data and MC, indicating that the detector alignment is well-modelled.

Additional smearing of the tracking resolution can cause noticeable mismatches in the short distance behavior of these plots. For example, for transverse smears of $\sim$10 μm, the corresponding plots are shown in figure 9.1. The fake vertices contribution is especially evident in plot (d) which shows the overproduction of vertices for the $1D$ category throughout the resolution region (40-1000 μm). This $1D$ contribution to this plot may be compared with the corresponding contribution to plot (b) which shows correctly vertexed $1D$ decays. The transverse smearing does not affect most of this resolution region since the longer fake vertex separation scales are induced by multiple Coulomb scattering of lower momentum particles. Instead, the discrepancies between data and MC caused by the smearing can be seen below 200 μm in plots (c) and (d) where the fake vertices are presumably formed from high momentum/large angle tracks from $1D$ decays.

Although the fitted distributions are somewhat sensitive to the detector resolution modelling, a better way to estimate the systematic effects is to make independent measurements of the detector resolution. This has been done in several ways. The smearing of the intrinsic resolution due to misalignments has been calibrated with μ-pair miss distances as shown in chapter 2, figure 2.11. Local misalignments are

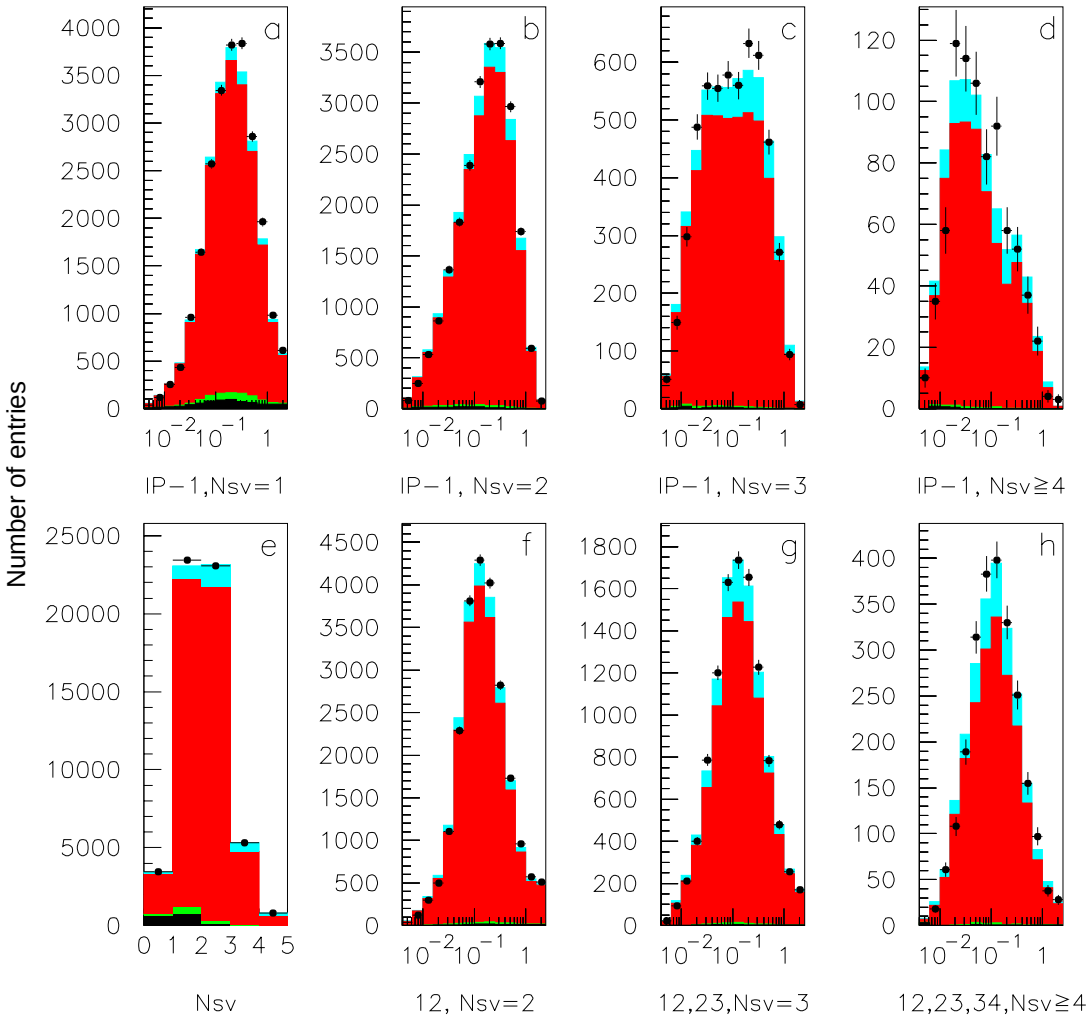

Figure 9.1: Fit results on a log scale, using ∼10 μm smearing on MC tracks. The stacked MC histograms are from bottom to top: *udsc* background, $0D$, $1D$, and $2D$. (a)-(d) show the IP to vertex 1 separation [cm], (f)-(h) shows the nearest neighbor vertex separations [cm], and (e) shows the resulting match in the vertex count distribution.

modelled by shifting tracks to match local mean impact parameter distributions as shown in chapter 3, figures 3.2 and 3.3. Figures 3.5 and 3.6 of that chapter show the match in the cumulative impact parameter distributions, both at high momentum where alignment effects dominate and at low momentum where multiple scattering errors dominate. These figures indicate that tracking resolution is well matched between data and MC. Figures 3.7 and 3.8 show that the error estimators are being consistently calculated between the data and the MC and so a 3 σ probability cut used to define vertices means the same thing in the data and in the MC. Finally, these studies were repeated at the vertexing level using $Z \rightarrow \tau^+\tau^-$ events. In figure 5.3 the negative tail of the measured 3-prong τ decay length distribution indicates that the resulting core vertexing resolution of the MC is well-matched to that of the real detector. Figure 5.4 shows the match in the tails of the error distributions.

To estimate the systematic error due to detector misalignment, the fit to the vertex separation distributions is performed both with and without the track shifts applied to the MC detector model. Removing the track shifts corresponds to a correlated unsmearing of the MC tracks of $\sim$3.3 μm in rϕ and $\sim$9.6 μm in z. i.e. Instead of shifting randomly about the nominal modelled track position, each track is shifted towards a more correct position. The resulting mismatch between the data resolution and the MC resolution is shown in figure 9.2 for the z impact parameter distributions. A reasonable estimate of the systematic error due to uncorrelated local resolution uncertainties is then obtained by taking half of the change in the measured values when doing this simultaneous correlated variation of all tracks. In principle, the systematic error could be even smaller than this estimate since the magnitude of the correlated

variation is much larger than the errors on the mean impact parameter distributions. However, since the precise origins of the shift effects can not be well determined, the more conservative approach of making larger than necessary variations is adopted.

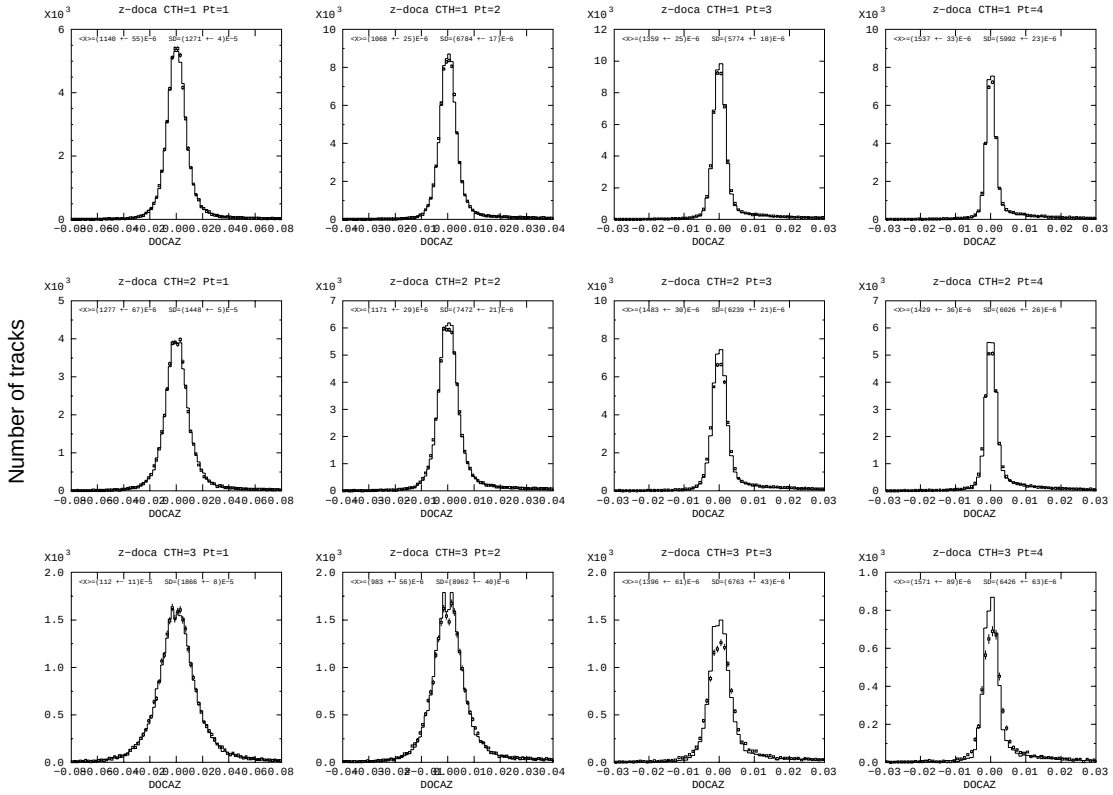

Figure 9.2: Mismatched Data/MC comparison of Z impact parameter distributions in 4 ranges of track P_t (left to right: < 0.7 GeV/c, 0.7-2.0, 2-5, > 5) and 3 regions of $|\cos\theta|$ (top to bottom: < 0.3, 0.3-0.55, > 0.55).

9.2 Physics Modelling Issues

A number of physics modelling issues lead to correlated effects on the measurement. The efficiency cutoff in the vertex resolution function depends on the momentum distribution of the tracks used for vertexing. The resolution function acts on the true decay length distributions which in turn depend on particle type composition, lifetimes, and boost distributions. The charged track multiplicity at each true vertex also affects the efficiency to find the vertex, and the vertex position resolution. The methods for estimating the modelling dependent systematic errors are described below and the results are later summarized.

9.3 The B energy distribution in Z^0 decays

The B hadron energy distribution controls the lab frame momentum of the daughter particles created in the decay. Since the tracking resolution is dependent on particle momentum, changes in the B energy distribution can affect the ability to find and separate vertices. The shape of the energy distribution has recently been measured by SLD [29]. The latest measurement [30] yields an unfolded energy distribution with $\langle x_B \rangle \equiv \langle E_B \rangle / 45.6 \text{ GeV} = 0.710 \pm 0.007$. The default SLD MC generates an x_B distribution with $\langle x_B \rangle \approx 0.700$ using a JETSET+LUND model for quark fragmentation. The resulting distribution is reweighted to match the unfolded measured distribution. Both distributions are shown in figure 9.3. The ± 0.007 variation is achieved by forming a mixture of the original distribution and the reweighted distribution by reweighting only some fraction of the sample.

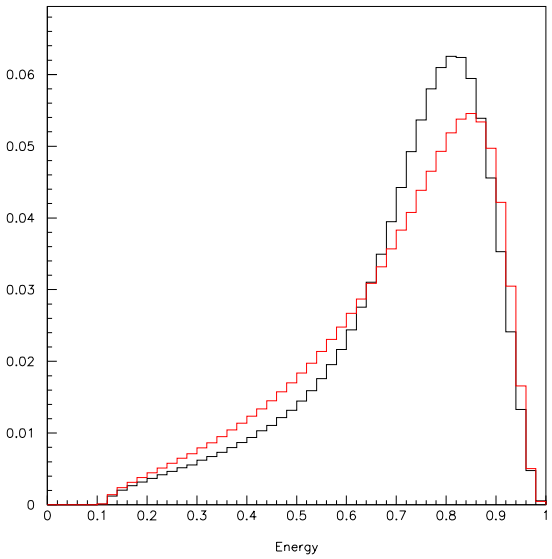

Figure 9.3: Original (dotted histogram) and reweighted (solid histogram) MC B energy distribution. Both are normalized to unity.

The 'opposite hemisphere tagging' procedure could lead to small biases in the B energy distribution which may later affect vertexing efficiency. In a 3-jet event, the highest energy quark jet has the longest B hadron decay length on average, and is the most likely to be tagged. The opposite hemisphere therefore is biased towards lower quark energy and hence lower decay length on average. These energy biases may be problematic if they are not modelled correctly in the MC. The MC predictions for the B tagging efficiency as a function of B energy and the corresponding opposite hemisphere energy bias are shown in figure 9.4. The predicted energy bias is much smaller than the errors in the actual measurement of the B energy distribution, and so the opposite hemisphere energy bias uncertainty is assumed to be included in the x_B variation above.

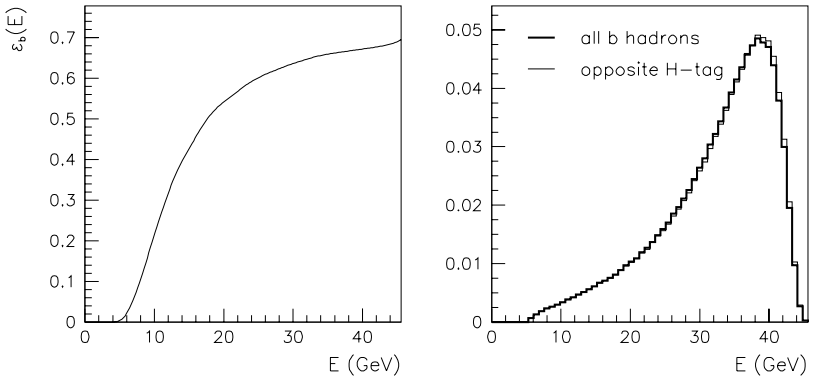

Figure 9.4: Left: MC predicted B tagging efficiency ϵ_b as a function of energy. Right: the opposite hemisphere energy bias.

9.4 Charmed hadron energies

Charmed hadrons are produced either directly from a Z^0 decay or as cascade particles from a B decay. The energy distribution of these hadrons again affects their daughter particle momentum and hence the effective vertexing resolution. For direct D's, the variation of $\langle x_D \rangle \equiv \langle E_D \rangle / 45.6 \text{ GeV} = 0.484 \pm 0.008$ suggested by the LEP Heavy Flavor Electroweak Working Group in [31] is used. The variation shown in figure 9.5 is performed by fitting the MC energy distribution to a Peterson function:

$$P(x_D) \sim \frac{1}{x_D * (1 - 1/x_D - \epsilon/(1 - x_D)^2)}. \tag{9.1}$$

The mean energy is then changed by varying the parameter ϵ. In principle, changes in the x_D distribution might change the vertexing efficiency in charm decay hemispheres and cause the background to look slightly more or less similar to $B \to 0D$ topologies. However, the $0D$ measurement appears to be very insensitive to this variation.

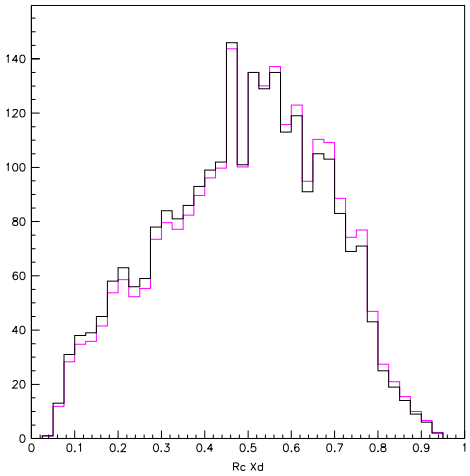

Figure 9.5: Original and reweighted MC D scaled energy ($x_D = E_D/45.6$ GeV) distribution in $Z^0 \to c\bar{c}$ events. Only events that are mistakenly tagged as $Z^0 \to b\bar{b}$ events are histogrammed.

In the case of cascade D's from B decays, the D energy distribution is also inversely correlated with the prompt B vertex particle multiplicity and energy. The more energy the D has, the less phase space is left for the other particles produced at the B vertex. Measurements by CLEO of the cascade D^0 and $D^{\pm}$ momentum distributions have been reported in [15]. The corresponding results for D_s and Λ_c can be found in [32] and [33] respectively. For D meson production, variations of these momentum distributions must be done carefully so that the tabulated measured branching fractions for various classes of decays such as semileptonic decays do not get inadvertantly changed. So, only the momentum distributions for untabulated decays producing D mesons are varied. These include the $1D$ Matrix 0, 8, and 9 decays discussed in appendix B. For c-baryon production, both tabulated and untabulated modes are varied. The variable part of the momentum distributions for

D^0's, $D^{\pm}$'s, and c-baryons are each fitted with Peterson functions. The functions are then varied until the total energy distribution from tabulated and untabulated modes reproduces the mean scaled momentum $\langle x \rangle \equiv \langle p \rangle / 4.95$ GeV for each of the CLEO distributions. Since only $1D$ modes are varied, these changes can be made independently of each other. (The variation of the $2D$ model is described below.) The MC events are then reweighted to the new functional form in order to make the branching fraction measurement. To estimate the error from the uncertainty in the $\langle x \rangle$'s in the CLEO distributions the measurement is made using an un-reweighted MC to define the [n]D categories. These variations are larger than the apparent errors on the $\langle x \rangle$ of the data distributions. However, since numerical values for the $\langle x \rangle$'s are not reported in the CLEO publication, these larger variations are used to estimate the (small) systematic error. The reweighted distributions and variations are shown in figures 9.6 and 9.7.

9.5 Heavy hadron lifetimes

As argued in chapter 5, the figure of merit in determining vertexing resolution is the ratio of the transverse track resolution to the decaying particle's lifetime. Heavy hadron lifetimes have been fairly well measured at the 1-6% level, and so small variations may be made in the MC by reweighting the exponential proper time distributions for each hadron type to lengthen or shorten the distributions. The current PDG numbers are used for the variations.

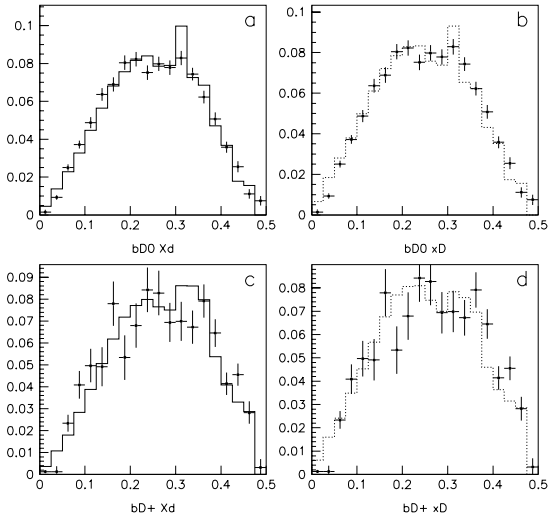

Figure 9.6: c-meson scaled momentum $x = P/4.95$ GeV, MC comparison with CLEO data. (a),(c) MC D^0, $D^{\pm}$ reweighted to match $\langle x \rangle$. (b),(d) un-reweighted MC D^0, $D^{\pm}$ for the variation. All histograms are normalized to unity for shape comparison.

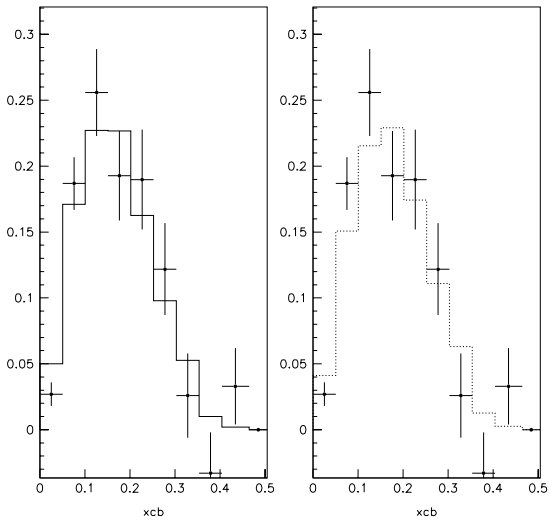

Figure 9.7: c-baryon scaled momentum $x = P/4.95$ GeV, MC comparison with CLEO data. Left: MC reweighted to match $\langle x \rangle$. Right: un-reweighted MC for the variation. All histograms are normalized to unity for shape comparison.

9.6 B species

For the composition of b hadron types produced in Z^0 decays, the LEP recommendations in [34] are used.

$$f_{B_s} = 0.105 \pm 0.018 \tag{9.2}$$

$$f_{\Lambda_b} = 0.101 \pm 0.039 \tag{9.3}$$

$$f_{B^\pm} = f_{B^0} = \frac{1 - f_{B_s} - f_{\Lambda_b}}{2} \tag{9.4}$$

where f_{Λ_b} represents the fraction for all kinds of b baryons.

9.7 0D composition

The $0D$ topology is modelled with charmonia producing modes such as $B \to J/\Psi\ X$ in the SLD MC. While rare B decays such as $b \to u$ and $b \to sg$ are expected to produce the same single vertex topology, the kinematics may be slightly different, and so the vertex finding efficiency and fake rate might also be different. To estimate the magnitude of these effects, $b \to u$ and $b \to sg$ MC is also generated and mixed in with the standard charmonia modes.

The JETSET generator [35] is used to produce $b \to u$ decays via flat phase space sampling. For each Z^0 decay event, one hemisphere is forced to undergo a $b \to u$ quark decay, while the other hemisphere is allowed to decay freely via the SLD B decay model. The $b \to u$ hemispheres therefore do not suffer any bias in the opposite hemisphere B-tagging procedure. Similarly $b \to sg$ hemispheres are generated using

a model created by Kagan and Rathsman [12] which simulates the production of hard kaons. In order to be able to accomodate rare decay rates as large as the theoretical expectation [3] of

$$BR_{rare} \equiv r_{rare} \cdot BR_{SL} \approx (2.6 \pm 1.1)\%, \tag{9.5}$$

the $0D$ sample fractions for each of $b \to u$ and $b \to sg$ are varied from 0 to 50%. This procedure varies BR_{rare} to be as large as $BR_{(c\bar{c})} = 2.3\% \pm 0.3\%$. For the central value of the measurement, only $(c\bar{c})$ modes are used.

9.8 1D composition

For the $1D$ sample, variations of the fractions $f_{D^\pm}$, f_{D_s}, and f_{Λ_c} are made with compensating variations in the largest fraction f_{D^0}. The magnitudes of the variations are contrained by the CLEO D counting measurements which utilize reconstruction of exclusive decays [15] [32], [33], [36]. T

For $f_{D^\pm}$, it is assumed that 80% of the $D^\pm$ counted in the CLEO measurement come from the lower vertex $1D$ category. Hence, $\sim$ 80% of the measurement error is applied to the MC fraction. The same variations are applied to B_s and b baryon decays, although it is not obvious that the CLEO measurements really apply. However, the effects of the variations are generally small, so a rigorous methodology is not necessary. The only exception is in charm baryon production where the CLEO meson decay errors are rather large, and so the corresponding variations are not applied to b baryon decays. The variations of the c-hadron momentum distributions have already been described above.

The last variation is that of the assumed B semileptonic decay rate into electrons, muons and taus. The raw MC is reweighted such that the induced rates for each of these processes (assuming the measured values of the $BR_{[n]D}$) match the corresponding world averages. The weights are then varied to reproduce the measurement errors. For $e^{\pm}$ and $\mu^{\pm}$, a variation of $BR_{SL} = 0.1071 \pm 0.0022$ [6] is used. For $\tau^{\pm}$, a value of $BR(b \to \tau^{-}\bar{\nu}X) = 0.0243 \pm 0.0032$ [37] is used. Although the decays producing both a $\tau^{\pm}$ and a D could mimic $2D$ decays, the systematic errors due to these variations are very small.

9.9 2D composition

The modelling of the $2D$ category is based on measurements by CLEO of $B \to D_s^{(*)}\bar{D}^{(*)}X$ and $B \to D^{(*)}\bar{D}^{(*)}K$ modes. This modelling is described in appendix B. Since the MC modelling defines the $2D$ modes for the BR_{2D} measured in the present analysis, variations of the modelling are necessary in order to estimate the possible deviations of the results from the true BR_{2D}.

The measured D_s momentum spectrum shown in figure B.3 has two components: a high momentum peak due to two-body $D_s^{(*)}\bar{D}^{(*)}$ decays, and a wider, lower momentum n-body spectrum ($n \geq 3$). Figure 9.8 shows various possible contributions to the observed spectrum from different decay modes as modelled by CLEO. To vary the SLD modelling, first the branching ratios for the four two-body decays to $D_s^{(*)}\bar{D}^{(*)}$ are each varied within their respective errors ($\sim 30\%$) for the exclusive mode measurements by CLEO.

Next, the kinematics of the n-body decays is varied. Although the CLEO measurements indicate that the n-body spectrum is dominated by three-body decays, the SLD modelling includes decay modes with multiple pion/kaon production and appears to be slightly softer than the data spectrum. To get a better match to the data, the spectrum is fit to a Gaussian with mean scaled momentum $\langle x_{D_s} \rangle \equiv \langle P_{D_s} \rangle / 4.91\ GeV/c = 0.194$ and then reweighted to a Gaussian with a higher mean, $\langle x_{D_s} \rangle = 0.234$. This reweighted MC is used for the central value of the measurement. The procedure is repeated to vary the distribution within the errors of the measured x_{D_s} distribution: $\Delta\langle x_{D_s} \rangle = \pm 0.03$. These variations, shown in figure 9.9 change not only the boost of the D, but also the prompt charged track multiplicity of the B decay and are thus expected to change the MC predictions for the number and distance distributions of found vertices.

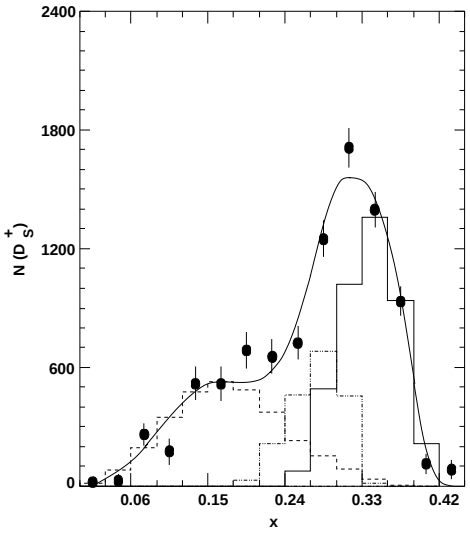

Figure 9.8: The CLEO B decay D_s energy distribution. The solid histogram represents the assumed ${D_s}^{(*)+}\bar{D}^*$ component, the dotted histogram represents the ${D_s}^{(*)+}\bar{D}^{**}$ component, and the dashed histogram is the ${D_s}^{(*)+}\bar{D}^*\pi/\rho$ contribution.

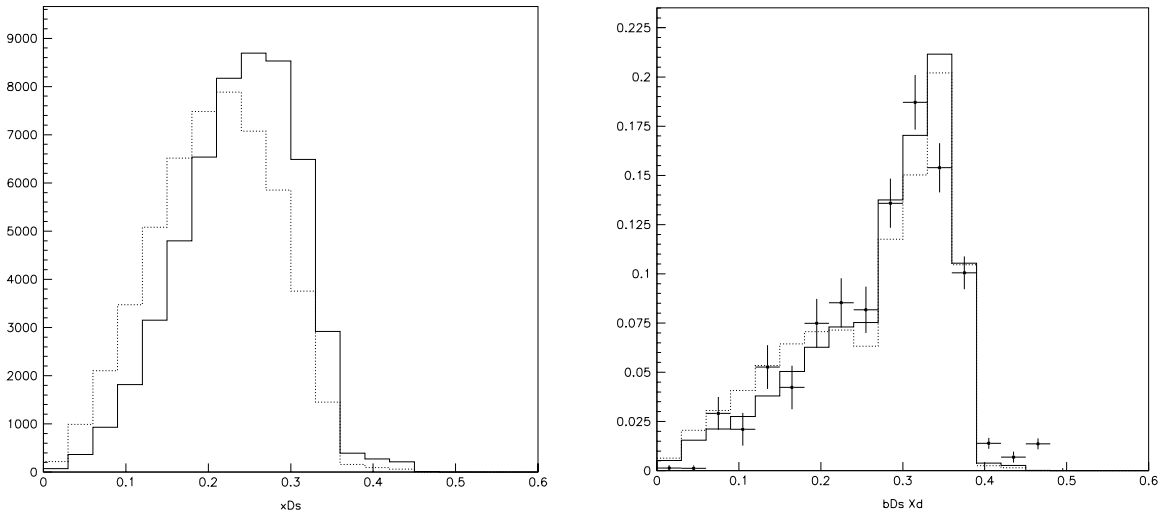

Figure 9.9: Variation of the D_s scaled momentum x=P/4.91 GeV spectrum (B rest frame) for $\geq$ 3-body $B \to D_s X$. The solid histogram represents the model used for the present analysis, and the dotted histogram represents the shape variation. Left: Only the $\geq$ 3-body decays. Right: The effect on the inclusive $B \to D_s X$ decays and comparison to CLEO data points. (Note: the CLEO measurements are in the $\Upsilon(4s)$ rest frame and have a little extra momentum smearing due to the average 340 MeV B momentum.)

Preliminary measurements for the exclusive branching ratios of several of the $B \to D^{(*)}\bar{D}^{(*)}K$ modes have been reported in [38]. These modes, and corresponding modes derived through strong isospin rotation are used for the MC modelling. Additional decay modes producing K^* instead of K are included to make the cumulative wrong sign D branching fraction match the inclusive CLEO measurement [39]. To vary the modelling, the $D\bar{D}K$, $D\bar{D}^*K$, $D^*\bar{D}K$, and $D^*\bar{D}^*K$ modes are each varied within the corresponding CLEO measurement errors. For each measured mode, the other modes derived by charge conjugation or isospin rotation, or by changing the K to a K^* are simultaneously varied by the same relative amount. For example,

when doing a variation of the $D\bar{D}K$ modes, the B^- decays to $D^0\bar{D}^0K^-$, $D^0D^-\bar{K}^0$, $D^0\bar{D}^0K^{*-}$, and $D^0D^-\bar{K}^{*0}$ modes are all simultaneously weighted up or down by the same multiplicative factor along with the corresponding modes for B^+, $\bar{B}^0$, B^0, $\bar{B}_s$, and B_s decays.

The above types of variations within each decay class are each expected to change the predicted charged track multiplicity at the B vertex and affect its visibility. Another possible variation is to change the relative overall magnitudes of the $D_s^{(*)}\bar{D}^{(*)}X$ and $D^{(*)}\bar{D}^{(*)}K^{(*)}$ contributions to the modelled $2D$ category. However, since each of these two decay classes is expected to produce some number of pions (or kaons) in addition to the D mesons, the MC predicted vertex count distributions (figure 9.10) for the two classes are rather similar. While this similarity precludes the possibility of measuring the two classes separately, it also makes the measured BR_{2D} fairly independent of the relative fractions of the two classes used for the modelling. The correlated variation of the overall magnitudes of each class causes smaller systematic effects than the previously discussed variations of the branching ratios within each class. The small systematic error from this source is evaluated by varying the overall branching fractions into each class by the errors in the world measurement averages for wrong sign D_s and wrong sign D production [11]. The systematic uncertainties produced through all of the discussed variations of the $2D$ modelling are small enough that correlations among the variations are ignored.

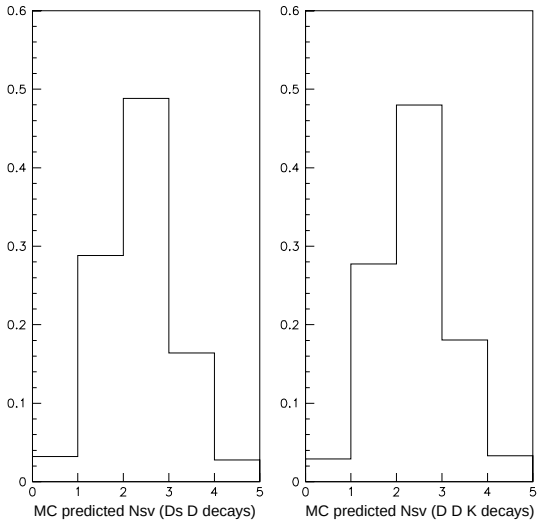

Figure 9.10: MC predicted found secondary vertex count for $B \to D_s^{(*)}\bar{D}^{(*)}X$ (left) and $B \to D^{(*)}\bar{D}^{(*)}K^{(*)}$ (right) decays. Each histogram has been normalized to unit weight.

9.10 Charged particle multiplicity

In order for vertices to be detected, the decays must produce at least one charged daughter particle. For D^0, $D^{\pm}$, and D_s, the multiplicities have been measured by MARKIII [40]. The multiplicity distributions are varied within the errors of these measurements by using the LEP procedure described in [31].

No direct measurements exist of the B prompt charged daughter multiplicity. However, DELPHI has measured the total B decay multiplicity to be 4.97 ± 0.07 charged particles, excluding products of ${K_s}^0$ or Λ decays. The B vertex multiplicity in the $1D$ category is varied in order to reproduce this ± 0.07 track uncertainty. In principle, this variation of the prompt B vertex multiplicity should already be covered by the D energy variations discussed earlier, and might be double counted here.

No direct measurements exist for charm baryon multiplicities either, and so the shape of the distribution is arbitrarily reweighted in order to shift the average by 0.3 tracks.

9.11 Tracking Efficiency Modelling

Small mismatches in the overall track count are observed between data and MC, with typically an excess of tracks found in the MC. Although these differences could be due to improper modelling of quark fragmentation, they could also be due to small errors in the tracking efficiency. To correct for this effect, tracks are binned in regions of solid angle and of momentum. In each bin, found MC tracks are randomly thrown away until the average bin counts match the counts seen in the data.

The entire difference between the measurement results with the tracking corrections turned on and off is taken to be the systematic uncertainty. The procedure may really be correcting a tracking overefficiency in the MC. Alternatively, if the track overcounts were really caused by overproduction of fragmentation tracks, the procedure could be introducing a false underefficiency for finding heavy flavor decay tracks. The systematic error derived from this procedure therefore really is two-sided though probably not distributed as a Gaussian.

9.12 $c\bar{c}$ and $b\bar{b}$ popping

In the jet fragmentation process, $g \to c\bar{c}$ and $g \to b\bar{b}$ processes may lead to production of additional vertices unrelated to the sample of primary B hadron decays being studied. To give an accurate model of this extra vertex contamination, the SLD MC is reweighted to give $g \to c\bar{c}$ and $g \to b\bar{b}$ rates of $2.33\% \pm 0.50\%$ and $0.269\% \pm 0.067\%$ as suggested in [34].

9.13 MC statistics

The analysis uses a MC sample with 25 times as many events as in the data sample. Since the fitting functions are modelled with shapes derived from the MC, the error from having finite MC statistics might be expected to be about a factor of 5 smaller than the data statistical error. To evaluate the MC statistics error, events in the MC sample are numbered and the MC sample is broken up into five subsamples which contain every 5th event. Separate measurements are made on the same data sample using the sets of functions derived from each MC subsample. The RMS of the measurement results gives an estimate of the MC statistics error for a subsample measurement. Since the RMS is poorly determined using only 5 independent measurements, the actual number used is the sum of the RMS and the error in the RMS. Finally, whatever the functional form of the MC statistics error, it must scale as $1/\sqrt{N_{MC}}$ where N_{MC} is the number of MC events. The subsample measurement error is therefore divided by a factor of $\sqrt{5}$ to estimate the error on the measurement made with the full MC sample. The MC statistics error estimated in this way is only

slightly smaller than the data statistcal error. The calculated correlation between the systematic fluctuations of the measurements of BR_{0D} and BR_{2D} is about 0.92, indicating that most of the compensating fluctuations are in BR_{1D}.

Source	Variation	$\delta BR_{0D}(\%)$	$\delta BR_{2D}(\%)$
vertex resolution	track shifts on/off	± 0.08	± 1.70
b energy	$\langle X_b \rangle = 0.710 \pm 0.007$	± 0.12	∓ 0.22
bkgd c energy	$\langle X_c \rangle = 0.485 \pm 0.09$	∓ 0.00	∓ 0.04
$(b \to c)$ energy	$\langle X_{D^0} \rangle = 0.2523 \pm 0.0072$	± 0.08	± 0.09
	$\langle X_{D^\pm} \rangle = 0.2660 \pm 0.0110$	∓ 0.06	± 0.13
	$\langle X_{\Lambda_c} \rangle = 0.1690 \pm 0.0124$	∓ 0.03	∓ 0.03
$B^\pm$ lifetime	1.65 ps $\pm 2.4\%$	∓ 0.05	∓ 0.26
B^0 lifetime	1.55 ps $\pm 2.6\%$	∓ 0.05	∓ 0.32
B_s lifetime	1.57 ps $\pm 4.6\%$	∓ 0.03	∓ 0.13
b baryon lifetime	1.22 ps $\pm 6.5\%$	∓ 0.11	∓ 0.11
D^0 lifetime	0.420 ps $\pm 1.0\%$	± 0.15	∓ 0.21
$D^\pm$ lifetime	1.067 ps $\pm 1.4\%$	± 0.02	∓ 0.08
D_s lifetime	0.450 ps $\pm 3.6\%$	∓ 0.08	∓ 0.24
c baryon lifetime	0.19 ps $\pm 5.8\%$	± 0.31	∓ 0.02
b species	$f_{B_s} = 0.105 \pm 0.018$	∓ 0.02	± 0.10
	$f_{\Lambda_b} = 0.101 \pm 0.039$	∓ 0.84	± 0.45
$g \to c\bar{c}$ rate	$(2.33 \pm 0.50)\%$	± 0.01	∓ 0.16
$g \to b\bar{b}$ rate	$(0.269 \pm 0.067)\%$	∓ 0.01	∓ 0.27

Source	Variation	$\delta BR_{0D}(\%)$	$\delta BR_{2D}(\%)$
$0D$ Model	frac. $b \to u:\quad 0.0 \to 0.5$	∓ 0.20	± 0.60
	frac. $b \to sg:\quad 0.0 \to 0.5$	∓ 0.78	± 0.22
$1D$ Model	$f_{D^\pm}\ \pm 0.0163$	± 0.39	∓ 0.01
	$f_{D_s}\ \pm 0.0187$	± 0.11	± 0.14
	$f_{\Lambda_c} \pm 0.0131$	∓ 0.64	± 0.10
	$BR_{SL} = (10.71 \pm 0.22)\%$	± 0.08	± 0.12
	$BR_{\tau^\pm X} = (2.43 \pm 0.32)\%$	± 0.01	± 0.00
$2D$ Model	n-body $x_{D_s} = 0.234 \pm 0.030$	± 0.24	± 0.36
	$BR(B \to D_s^+ \bar{D}) = (1.10 \pm 0.35)\%$	± 0.09	± 0.19
	$BR(B \to D_s^+ \bar{D}^*) = (1.12 \pm 0.36)\%$	± 0.09	± 0.20
	$BR(B \to D_s^{*+} \bar{D}) = (0.89 \pm 0.31)\%$	± 0.08	± 0.18
	$BR(B \to D_s^{*+} \bar{D}^*) = (2.41 \pm 0.74)\%$	± 0.14	± 0.39
	$BR(B \to D\bar{D}K) = (0.25 \pm 0.25)\%$	∓ 0.13	∓ 0.47
	$BR(B \to D\bar{D}^*K) = (0.50 \pm 0.35)\%$	∓ 0.17	∓ 0.48
	$BR(B \to D^*\bar{D}K) = (0.50 \pm 0.30)\%$	∓ 0.07	∓ 0.21
	$BR(B \to D^*\bar{D}^*K) = (1.50 \pm 0.85)\%$	∓ 0.28	∓ 0.39
	inc. wrong-sign D_s rate $= (9.8 \pm 3.7)\%$	± 0.19	± 0.41
	inc. wrong-sign D rate $= (8.2 \pm 1.3)\%$	∓ 0.11	∓ 0.25

Source	Variation	$\delta BR_{0D}(\%)$	$\delta BR_{2D}(\%)$
B prompt tk mult	4.97 ± 0.07	∓ 0.05	∓ 0.92
D^0 tk mult.	wgt 0-prongs	∓ 0.64	± 0.29
	wgt 4-prongs	∓ 0.03	∓ 0.28
	wgt 6-prongs	∓ 0.17	∓ 0.26
$D^{\pm}$ tk mult.	wgt 1-prongs	± 0.01	± 0.46
	wgt 5-prongs	∓ 0.03	± 0.11
D_s tk mult.	wgt 1-prongs	± 0.03	± 1.47
	wgt 5-prongs	∓ 0.14	± 0.15
c baryon tk mult.	2.269 ± 0.302	∓ 0.96	± 0.79
tracking efficiency	reject excess MC tks	± 0.25	∓ 0.81
MC statistics	using 5 MC subsamples	± 0.70	± 0.86
Total		2.1	3.3

Chapter 10

Discussion of the Results

10.1 The Results

The results of the measurement are:

$$BR(B \to (0D)X) = (3.7 \pm 1.1 \pm 2.1)\% \quad (10.1)$$

$$BR(B \to (2D)X) = (17.9 \pm 1.4 \pm 3.3)\% \quad (10.2)$$

where the first error is statistical and the second is systematic. The correlation coefficients between the two measurements are $C_{0D,2D} = 0.702$ and -0.080 for statistical and systematic errors, respectively. N_c is calculated using a value of $BR_{(c\bar{c})} = (2.3 \pm 0.3)\%$ [11] in equation 1.11:

$$N_c = 1.188 \pm 0.010 \pm 0.040 \pm 0.006. \quad (10.3)$$

Here, the third error is due to the uncertainty in $BR_{c\bar{c}}$. Limits on BR_{rare} may be set using equation 1.12:

$$BR_{rare} = (1.4 \pm 2.4)\%. \tag{10.4}$$

The measured value of N_c is plotted in figure 10.1 and compared with the LEP and CLEO measurement averages discussed in [10] and [11], and with the theoretical region discussed in chapter 1. BR_{rare} is consistent with the theoretical expectation of $(2.6 \pm 1.1)\%$ [3]. Since the fractions add up to unity, figure 10.1 indicates that BR_{2D} is also consistent with theoretical calculations.

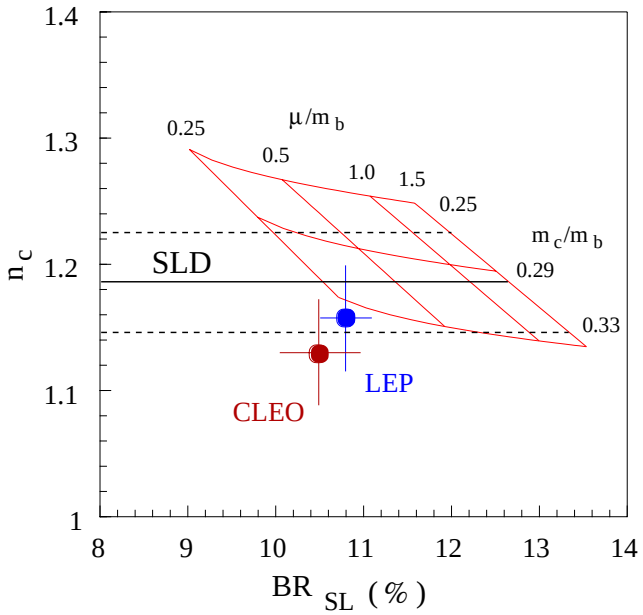

Figure 10.1: The SLD measurement of N_c compared with measurements of N_c and BR_{SL} by LEP and CLEO and with theoretical expectations. Since the SLD BR_{SL} measurement [41] has not been finalized, the SLD N_c result is shown as a horizontal band on this plot.

10.2 Discussion of other measurement techniques

Several techniques have been employed to measure N_c in B decays and a nice summary may be found in [11]. The measurement averages shown below are taken from this reference.

10.2.1 Exclusive reconstruction techniques

The first class of measurements uses exclusive reconstruction of D decay modes to count open charm hadrons. The D count may be supplemented by determinations of $BR_{(c\bar{c})}$ to obtain the charm count. The largest common systematic uncertainty in these analyses is the uncertainty in the branching ratio of the exclusive D decay mode used ($D^0 \to K^-\pi^+$, $D^+ \to K^-\pi^+\pi^+$, $D_s^+ \to \phi\pi^+$, $\phi \to K^+K^-$, etc). The correlated systematic errors account for about half of the total measurement errors. The LEP and CLEO averages for this technique are:

$$N_{c,LEP} = 1.176 \pm 0.039 \pm 0.063 \quad (10.5)$$

$$N_{c,CLEO} = 1.130 \pm 0.041 \pm 0.045 \quad (10.6)$$

where second error indicates the correlated errors from the c-hadron branching fraction uncertainties.

A variant of the exclusive reconstruction technique is to tag the sign of the decaying B hadron using leptons or kaons produced in the decay of the other B hadron in the event. The sign of the exclusively reconstructed D may then be used to deter-

mine the wrong-sign D fraction and hence BR_{2D}. Again these techniques are directly correlated through the uncertainty in the exclusive D decay rates and the charmonia production rate. A further problem is that to calculate N_c via equation 1.11, these BR_{2D} measurements must be supplemented with measurements (or guesses) of either BR_{0D} or BR_{1D}.

To date, the values of N_c determined using wrong-sign D measurements have not calculated using a consistent methodology and are thus not included in the experimental comparison plots, figures 1.2 and 10.1. In reference [11], for example, measurements of

$$r_D \equiv BR(\bar{B} \to \bar{D}\ X)/BR(\bar{B} \to D\ X) \tag{10.7}$$

are used together with measurements of the unsigned open charm count to extract BR_{2D}. The values obtained are:

$$BR_{2D,LEP} = 0.247 \pm 0.039 \pm 0.043 \tag{10.8}$$

$$BR_{2D,CLEO} = 0.174 \pm 0.030 \pm 0.029 \tag{10.9}$$

where the second error again represents the correlated systematics. The measurements of the wrong-sign D rate and the unsigned D rate together are enough to determine BR_{1D} and BR_{0D} as well since the second measurement alone is enough to determine $N_c - BR_{c\bar{c}}$. Instead, the authors arbitrarily ignore this information and calculate N_c using an independently determined smaller experimental value of BR_{0D} (and hence a larger BR_{1D}). This procedure is equivalent to assuming without justification that the efficiency for detecting wrong-sign D's is greater than the efficiency

for detecting correct-sign D's in the measurement of the total D rate. If the correct values for BR_{0D} and BR_{1D} are used, then the calculated N_c would of course coincide with the value calculated using the unsigned D rate measurement alone. The only new information really obtained by combining the two measurements is that the implied BR_{0D} value is anomalously high.

10.2.2 Topological techniques

The second class of measurements uses topological and kinematic information about the B decays in order to make inclusive measurements of the $0D$, $1D$, and $2D$ categories. The present analysis as well as an impact parameter-based measurement by DELPHI [13] are included in this class. Whereas DELPHI's technique relies on the number of D decay tracks found at the impact parameter scale c$\cdot(\tau_B + \tau_D)$ in order to separate $1D$ and $2D$ decays, the SLD analysis actually reconstructs the vertex topology. The SLD measurements are consistent with the DELPHI measurements of

$$BR_{0D,DELPHI} = (3.3 \pm 2.1)\% \tag{10.10}$$

$$BR_{2D,DELPHI} = (13.6 \pm 4.2)\% \tag{10.11}$$

Using the same $BR_{c\bar{c}}$ as above, these measurements give:

$$N_{c,DELPHI} = 1.149 \pm 0.046 \tag{10.12}$$

The common systematics between the SLD and DELPHI measurements include the modelling of the decay categories since most details of the B decay modelling come from common sources. The $BR_{c\bar{c}}$ value must again be used as well to extract N_c from either analysis. However, the largest systematic error in each analysis is the detector resolution uncertainty which is obviously not correlated with the results of any other measurement.

The sizable correlations among the measurement techniques is a little worrisome. However, the dominant systematic uncertainties (exclusive D decay rates, detector resolution) for the two classes of measurements are different so that systematic biases in the measurement averages are ameliorated. Correlations between the topological method and the exclusive reconstruction method appear to be small. For example, the modelling of the $2D$ category in the topological method comes directly from the wrong-sign D^0, $D^{\pm}$, and D_s rates discussed above and so uncertainties in the c-hadron branching fractions can affect the modelling. As shown in chapter 9, the SLD measurement is only mildly dependent on variations of the $2D$ modelling.

10.3 Conclusions

The overall experimental picture shows consistency among the various experiments. The new SLD results for BR_{0D}, BR_{2D}, and N_c are consistent with the previous measurements listed above. However, the central value of the SLD N_c result is slightly higher than that of previous measurements and should pull the world average more into the theoretically preferred region in figure 10.1.

The measurements of N_c and BR_{SL} are in good apparent agreement with the predictions of local quark-hadron duality and the heavy quark effective theory. However, the region of agreement in figure 10.1 still corresponds to an uncomfortably low value of the renormalization scale $\mu/m_b \approx 0.25$. The calculated NLO hadronic rates (figure 1.1) begin to blow up as μ is lowered causing the predicted BR_{SL} to decrease more and more rapidly as μ approaches Λ_{QCD}. This runaway behavior in the calculation as well as the substantial difference between the NLO and the LO calculations shown in this figure suggest that the perturbative calculation has not yet converged. Similar remarks apply to the slightly differrent $r_{\bar{u}d}$ and $r_{\bar{c}s}$ calculations [7] used to generate the theory region in figure 10.1. NNLO calculations are needed before any definite conclusions may be drawn.

As for experiments, future improvements in the measurement of N_c through exclusive reconstructions may be achieved mainly through precision measurements of D decay rates, in particular the rate $BR(D^0 \to K^-\pi^+)$. The current best measurements (by CLEO and ALEPH) are already close to being dominated by systematic errors, and so improvements may be most easily obtained at a future dedicated tau-charm factory.

For the inclusive topological techniques, future improvements will come naturally as measurements of B decay properties from the B-factories become available for MC B decay modelling. Improved detector resolution should also help in reconstructing the decay topologies. Improvements in resolution can increase the analyzing power of the topological measurement by increasing the efficiency to separate vertices at short decay length and thus provide greater differences in the expected $1D$ and $2D$ vertex

count distributions. The greater analyzing power should reduce the susceptibility of the technique to systematic uncertainties in the modelling.

More importantly, the track measurement tails must be under control. Figure 8.1 indicates that tail production of fake vertices is at least a 10-20% effect, causing a large dilution of analyzing power and also a large errors in the analyzing power due to uncertainties in the vertexing resolution. The low momentum track error tails may be reduced by using less detector material which might cause multiple Coulomb scattering. The high momentum track error tails due to local detector misalignments may be reduced by collecting enough data to achieve a very precise alignment. If a detector has such good resolution that the typical distance scale characterizing the tails is still smaller than the decay length scales of interest, then a larger vertex χ-squared cut may be used to make the measurement using the tail resolution rather than the core resolution of high momentum tracks. Such good tail resolution is again only achievable after a precision detector alignment.

Appendix A

Theoretical Background

The Standard Model is the best known description of the strong, weak, and electromagnetic interactions. It is formulated as a strictly Lorentz invariant quantum field theory and thus satisfies the principle of causality and provides a local description of physical phenomena. The structure of a Langrangian field theory such as the Standard Model is completely determined by the symmetry groups describing the interactions, the representations that the fields transform as, and the way the symmetries are broken. The model can then be constructed by writing down the Lagrangian as a sum of the kinetic terms for the fields as well as all possible renormalizable[1] interaction terms allowed by the symmetries and the symmetry breaking mechanism. The strengths of the low energy couplings are not determined by any known principle

[1]The finite set of allowed interaction terms whose coupling constants have positive semi-definite mass dimension are called 'renormalizable' because all divergences in loop integrals can be absorbed into redefinitions of that same set of coupling constants. The infinite set of interactions whose coupling constants have negative mass dimension are deemed 'irrelevant' because by dimensional analysis, their effects at energy k must be suppressed with powers of (k/M) for some presumably large mass scale M. The low-energy effective action then only contains the renormalizable interactions.

(other than the anthropic principle), and can only be measured in experiments.

A.1 The Standard Model

The Standard model has the gauge symmetry group SU(3) × SU(2) × U(1). The field content and representations are:

Spin	Name	Gauge Representation
0	Higgs scalars: (ϕ)	(1, 1, 0) or (1, 2, +1/2)
1/2	left-handed leptons: $(e_L, \nu_e), (\mu_L, \nu_\mu), (\tau_L, \nu_\tau)$	(1, 2, +1/2)
1/2	right-handed charged leptons: e_R, μ_R, τ_R	(1, 1, -1)
1/2	left-handed quarks: $(u_L, d_L), (c_L, s_L), (t_L, b_L)$	(3, 2, -1/6)
1/2	right-handed u-type quarks: u_R, c_R, t_R	(3, 1, 2/3)
1/2	right-handed d-type quarks: d_R, s_R, b_R	(3, 1, -1/3)
1	SU(3) connections (gluons, or g)	(8, 1, 0)
1	SU(2) connections	(1, 3, 0)
1	U(1) connection	(1, 1, 0(adjoint))

In the spontaneous symmetry breaking paradigm, the Higgs potential energy density

$$V(\phi) = -\mu^2 \cdot (\phi \cdot \phi) + \lambda \cdot (\phi \cdot \phi)^2 \tag{A.1}$$

causes the Higgs field(s) to condense in the vacuum as the universe cools to a temperature $T^4 < \mu^4/\lambda$. An emergent vacuum expectation value for any component of

the Higgs field, for example:

$$\langle\phi\rangle = \sqrt{\frac{\mu}{2\lambda}} \tag{A.2}$$

is a non-vanishing order parameter and so a 2nd-order phase transition occurs in which the SU(2) $\times$ U(1) is spontaneously broken to a single U(1) whose generator is a linear combination of the two original Cartan generators. This remaining U(1) describes the electromagnetic force, and its connection is the photon field A^μ. In analogy with the Meissner effect in superconductors, the connections corresponding to the broken symmetries become massive and mediate short-range interactions. The connection corresponding to the broken orthogonal combination of Cartan generators gives the massive Z^0 vector boson which mediates neutral current weak interactions. The connections corresponding to the SU(2) ladder operators become the massive $W^\pm$ vector bosons which mediate the charged current weak interactions. The B hadron sample studied in in this document are created in Z^0 decays and they in turn decay weakly via virtual $W^\pm$ emission.

The quark and lepton matter fields are arranged in three copies or 'generations.' For example, there are three flavors of up-type (SU(2) isospin +1/2) quarks $u'_i \equiv (u', c', t')$ and three flavors of down-type (isospin -1/2) quarks $d'_i \equiv (d', b', t')$. The primes here indicate that these fields are the flavor eigenstates which the $W^\pm$ couples to. The Hamiltonian eigenstates u_i and d_i are expected in general to be superpositions of fields with identical gauge quantum numbers.

$$u_i \equiv (M^{-1})_{ij} \cdot u'_j, \quad d_i \equiv (N^{-1})_{ij} \cdot d_j, \tag{A.3}$$

where M_{ij} and N_{ij} are unitary matrices. The coupling of the $W^{\pm}$ to the quark fields can then be written in terms of the quark mass eigenstates as:

$$\mathcal{L}_{int} \sim \bar{u}_i \cdot M^{\dagger}_{ik} \cdot \gamma^{\mu}(1-\gamma^5) W^{\pm}_{\mu} \cdot N_{kj} \cdot d_j \tag{A.4}$$

$$\sim \bar{u}_i \cdot \gamma^{\mu}(1-\gamma^5) W^{\pm}_{\mu} \cdot V_{ij} \cdot d_j \tag{A.5}$$

where the Cabbibo-Kobayashi-Maskawa (CKM) matrix V_{ij} has been defined as:

$$V_{ij} \equiv M^{\dagger}_{ik} \cdot N_{kj}. \tag{A.6}$$

The CKM matrix parameterizes the observable effects corresponding to the dressing of the flavor eigenstates by the interaction terms. Measurements of V_{ij} indicate that the matrix is mostly diagonal. Furthermore, b-hadrons are seen to primarily decay to c-hadrons, indicating that $b \to u\ W$ transitions are quite rare: $V_{ub} \ll V_{cb}$.

The Standard Model has a total of 19 free parameters to be determined by experiment:

2	symmetry breaking couplings (μ, λ)
6	quark masses
3	lepton masses
3	gauge couplings
3	quark mixing angles in V_{ij}
1	complex phase in V_{ij}
1	angle characterizing the QCD vacuum

In addition, if recent measurements are correct and neutrinos do indeed have mass, this list must be augmented to include the neutrino masses and a lepton mixing matrix as well.

A.2 A conundrum in high energy physics

A great deal of effort has been made on the part of both theoretical and experimental physicists to verify the perturbative predictions of the Standard Model. Through this process, the Standard Model has become recognized as the most accurate model of the relatively low energies that present day experiments are able to probe. Indeed, the current program of high precision measurements is predicated on the assumption that deviations from SM predictions are indicators of new physics present at higher energy scales.

However, the situation is not as clear for phenomena which must be described non-perturbatively in the SM. Particularly troubling is the SU(3) description of the strong force which is asymptotically free at large energy scales but becomes strongly coupled at low energies Λ_{QCD} around the proton mass.[2] This energy scale characterizing the breakdown of perturbation theory may be defined implicitly by $\alpha_s(\Lambda_{QCD}) = 1$, where α_s is the SU(3) coupling constant squared. Attempts to predict non-perturbative phenomena by numerically evaluating path integrals have had some limited success in predicting the energy spectrum of bound states, but there is still no real firm

[2]In order to minimize the chromo-electromagnetic potential energy due to locally isolated color charge, quarks and anti-quarks are confined in color-neutral bound states called hadrons. Since Λ_{QCD} characterizes the typical binding energy, it is reasonable to expect that Λ_{QCD} is approximately the proton mass.

theoretical understanding of basic empirical observations such as the mass gap, quark confinement, and chiral symmetry breaking.

In heavy flavor physics, the computational problem can be simplified by employing the spectator model. In the approximation that the heavy quarks b and c have masses much larger than the QCD scale, the heavy flavor physics decouples from the lower energy QCD effects involving the light quarks. In this limit, the light quarks become independent spectators of whatever is happening to the heavy quarks. Effects from interactions between the heavy and light quarks are presumably suppressed by powers of Λ_{QCD}/M_Q where M_Q is the heavy quark mass scale. Furthermore, in the hadronization process after the weak decay, interactions between the decay products from the W and the spectator quarks are suppressed by a statistical color factor $(1/N_c)^2$, where N_c is the number of colors. Effects due to the spectator quarks are therefore believed to be only refinements to the basic heavy quark decay process. Using this assumption (local quark-hadron duality), the hadronic decay matrix elements needed to predict the physical decay rates may be approximated with quark decay matrix elements. The latter transition probabilities can be calculated using operator product expansions in the heavy quark effective theory.

Within perturbation theory, a persistent problem in heavy quark QCD predictions is the dependence of the calculations on the renormalization scale μ through the running of the strong coupling constant α_s. To obtain a convergent perturbative expansion, μ should be chosen to be around the typical energy scale in the process, in this case the heavy hadron binding energy. Luckily, these binding energies are sufficiently larger than Λ_{QCD} such that QCD interactions may indeed be treated per-

turbatively within this regime. Computations truncated at a given order in α_s have a μ dependence since the precise value of μ influences the magnitude of the higher order terms which are being neglected. Of course, the μ dependence may be reduced by including more higher order terms, but this procedure can be very computationally intensive, involving hundreds of diagrams even at 2-loops. In practice, precise theoretical predictions are rarely possible and even the extraction of useful information from experimentally measureable quantities is often difficult. Nevertheless, hard experimental data can sometimes be used to validate or invalidate certain theoretical assumptions and approximation procedures, and to reduce uncertainties in the experimental inputs to theoretical calculations.

Appendix B

Modelling the Decay Categories

B.1 Issues in modelling the vertex count

The $0D$, $1D$, and $2D$ branching fractions measured in the analysis are defined in terms of the SLD Monte Carlo, in particular by the B decay modelling. Information about the modelling is therefore necessary in order to properly interpret the results. For a vertex counting analysis, the main issues to be considered in the B decay model are the correct rate of production of visible vertices and the correct production of decay length distributions. In order to find a vertex, it first must have detectable charged tracks emanating from it. Vertices with no associated charged particles are an unavoidable inefficiency in the vertex count, and must be accounted for in the modelling. Kinematics also plays a role since vertices with only low P_t particles may not be distinguishable from other vertices elsewhere along the decay chain. More specifically, the resulting low P_t tracks tend to be consistent with more than one true

decay point. For example, the slow pion from a D^* decay is an excellent estimator for the true D flight path and hence it should vertex well with the B vertex as well as the D vertex. Then, about half of the time, it will be captured by the D causing the B vertex to be harder to detect.

An accurate model of the decay kinematics is necessary to predict the efficiency for separating vertices. A feature of the cascade structure of B decays is that the kinematics of the B vertex is somewhat correlated with the kinematics of the D vertex. The higher the energy of the D meson, the less phase space is available to create particles and transverse momentum at the B vertex. The modelling of the momentum spectrum of the various D species should therefore be sufficient to mostly constrain the phase space available to produce direct B daughter particles.

The vertex separation efficiency also depends on the D decay length distributions which are controlled by the B rest frame D momentum distribution 'convolved' with the B boost distribution. The latter distribution is generated through the quark fragmentation model in LUND which is tuned to produce an $\langle x_B \rangle \equiv \langle E_B \rangle / M_{Z^0}$ of 0.700. The generated distribution is reweighted to reproduce the unfolded SLD measured distribution with $\langle x_B \rangle = 0.710$ as shown in figure B.1.

Other data distributions to be matched include the B and D decay lepton spectrum, the charged particle multiplicity distribution, and the production rates of various light hadron species. The B decay model and its reproduction of independently measured data are discussed below.

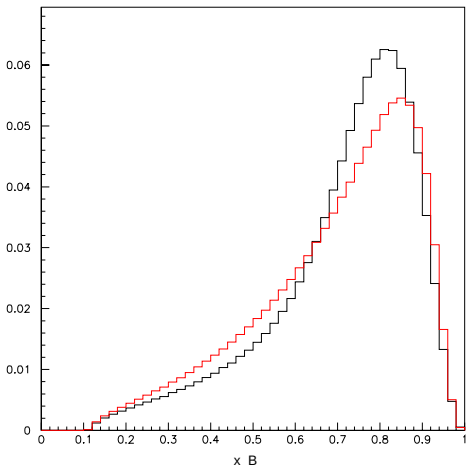

Figure B.1: The LUND raw B scaled energy distribution (dashed histogram) is reweighted to reproduce the sharper SLD measured distribution (solid histogram).

B.2 The SLD B decay model

The SLD B decay model uses a combination of the JETSET [35] and CLEO [43] decay models.[1] The organizational structure of the two models is similar. For each unstable particle, a list of possible decay modes is tabulated, along with the desired branching fraction into each mode. Each decay mode is described using a list of daughter particles produced in the decay as well as some specific instructions on generating the decay kinematics. If no specific instructions are given, then the kinematics are determined using random phase space sampling. In the SLD MC, the CLEO table and associated software is used for B_u, B_d, and B_s meson decay. The JETSET code is used for everything else, including decays of b-baryons and charmed hadrons.

The B meson decay tables are compiled using measured exclusive branching fractions. However, the list of well-measured decays is far from complete, so various

[1]Many thanks to Peter Kim for his help with tuning the SLD version of the CLEO decay table.

theoretically motivated assumptions must be made in constructing the list of exclusive modes. Two common assumptions are factorization and strong isospin symmetry. As mentioned before, factorization is the approximation that the mediating $W^{\pm}$ particle decays and fragments into hadrons independently of the fragmentation of the remaining quarks from the decaying particle. Rates of processes mixing the 'upper vertex' $W^{\pm}$ decay products and the 'lower vertex' decay products are believed to be suppressed by a statistical color factor $1/N_c^2$.

The approximate strong isospin symmetry between bound states containing u quarks and those containing d quarks is then applied separately to the upper vertex and the lower vertex (or to the combined vertex in the color suppressed diagrams). Any combination of hadronic products which require a $g \to u\bar{u}$ popping is isospin rotated to a final state with $g \to d\bar{d}$ popping instead, and vice versa. The branching fraction into the new final state is considered to be the same as that for the original final state. The isospin symmetry of the spectator quark is also used to make the B_u, B_d, and B_s decay tables manifestly isospin symmetric. This procedure of course ignores the different interference effects present for each B species between diagrams which contribute to the same physical process. This kind of error, while in principle correctable, is probably small compared to the errors due to the large fractions of unknown decays which must also be modelled.

Another assumption made is that since vector mesons have three polarizations, the branching fraction to the vector meson is approximately three times the branching fraction for the corresponding pseudoscalar meson since each polarization is approximately equally likely to be produced. In cases where vector meson branching fractions

have not been measured and tabulated, this rule is used to model the appropriate relative rates.

Even after symmetry considerations are applied, the exclusive mode branching fractions sum only to about 60%. The remaining 40% reflects our lack of knowledge of B decay physics, and is one of the primary motivations for the current study of B physics. It is precisely here that we may expect to find possible enhanced signals for $b \rightarrow s\ g$ and $b \rightarrow D\ \bar{D}\ X$. Much of the unknown branching fraction is presumably from untabulated $1D$ modes also. In the B decay modelling, the unknown modes are modelled using three separate 'inclusive' models to produce generic $1D$ decays. The main difference between the models is that they populate different regions of the daughter D momentum spectrum and thus can be used to fit the distributions measured by CLEO.

The first model, referred to as 'Matrix 0' uses the simplest possible assumption– that the B undergoes a random phase space decay to the appropriately charged D and a number of hadrons. $q\bar{q}$ pairs are popped out of the vacuum, hadronized, and given kinetic energy until all of the phase space from the B mass is used up. The rate of producing vector D^* mesons is tuned to match the rates measured by CLEO [15]. Matrix 0 decays typically produce a relatively low D energy, and a large number of low momentum light hadrons.

The second and third models are referred to as 'Matrix 8' and 'Matrix 9' respectively. These models attempt to shift the D meson to higher energies compared to the Matrix 0 decay, thereby producing a better match to the measured $B \rightarrow D$ energy distributions. To force the production of more energetic D mesons, the B is consid-

ered to first decay to a fictitious higher mass resonance which then decays exclusively to 2-body modes like $D\ \pi$ or $D\ K$. The mass of the resonance then controls the produced D energy. The remaining quarks in the B decay are hadronized using the same procedure as in Matrix 0. Matrix 8 and Matrix 9 use slightly different fake resonances, each peaked in a different characteristic region of the D energy distribution with the spreads in D energy determined by the widths of the resonances.

B.3 Comparison with experimental data

In order to compare directly MC with CLEO data, a special sample of B decays generated in a MC simulation of $\Upsilon(4s)$ decays is used. The D momentum distributions measured by CLEO [15] are fit with a combination of Matrix 0, 8, and 9 decays to determine the appropriate branching fractions into each inclusive mode. Thus, the measured distributions are then reproduced in the MC with minimal assumptions. The comparison plots are shown in figure B.2. For the purposes of the current analysis, the main effect of the inclusively modelled modes is to provide an accurate simulation of the $1D$ decay kinematics and the resulting topology.

The D_s and c-baryon production is modelled using mainly tabulated modes. The match in the momentum spectrum to measurements for D_s [32] and Λ_c [33] by CLEO is displayed in figure B.3.

Tracks with high P_t give very good vertexing resolution. These tracks tend to be formed by prompt particles from the B vertex, especially in low multiplicity decays. A large portion of these decays are semileptonic, and so an accurate modelling of the

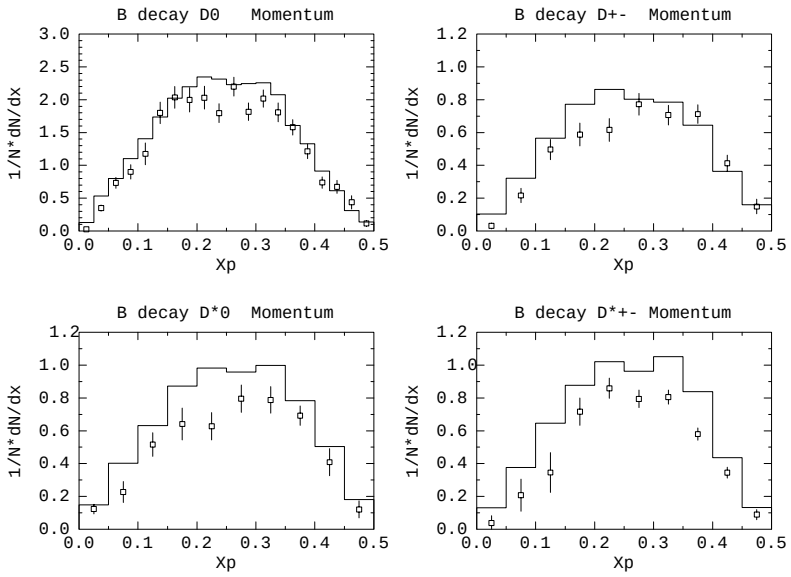

Figure B.2: B decay D momentum distributions. The SLD MC histogram is compared with CLEO data points. The plots are normalized to the number of D's per $\Upsilon(4s)$ decay. The difference in the normalizations reflects the lower value of N_c measured by CLEO.

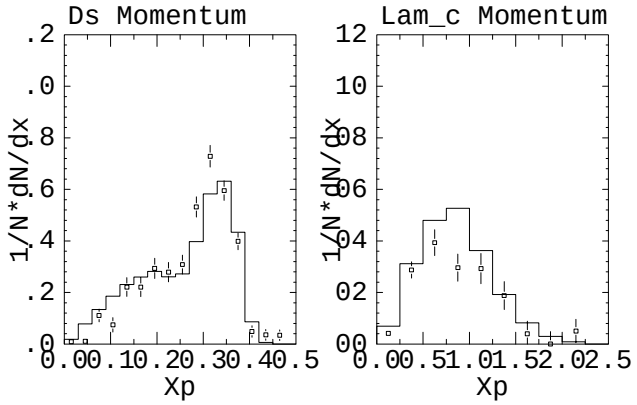

Figure B.3: B decay D_s, Λ_c momentum distributions. The SLD MC histogram is compared with CLEO data points. The plots are normalized to the number of c-hadrons per $\Upsilon(4s)$ decay.

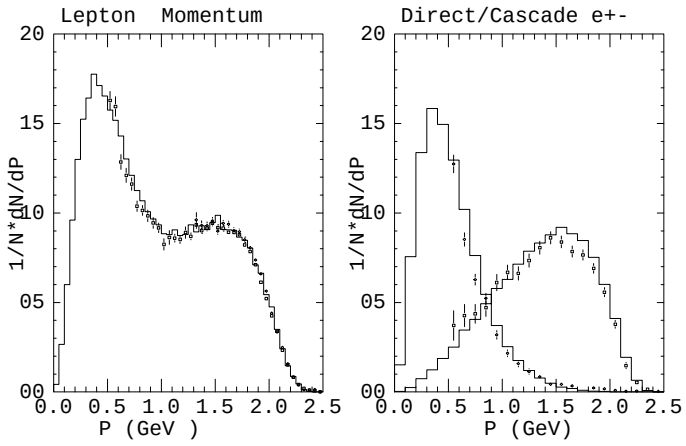

Figure B.4: Left: B decay lepton momentum distribution. Right: B direct and cascade $e^{\pm}$ momentum distribution. The SLD MC histogram is compared with CLEO data points.

semileptonic decays is needed. The SLD/CLEO MC uses the Isgur-Wise model [44] [45] to produce the kinematics of these decays. The results are compared with CLEO data [46] [5] in figure B.4.

The other data distributions to be reproduced include the low momentum $\pi^{\pm}$, $K^{\pm}$, $p^{\pm}$, and K_s^0 distributions from ARGUS [47], and the total B decay charged particle multiplicity distribution measured by CLEO [48]. The results are shown in figures B.5 and B.6. Getting precise matches of these two plots has proven to be difficult and is a recurring problem in many attempts by different experiments to model the B decays. The small mismatches in the modelling of these distributions are accepted as an unavoidable consequence of our lack of knowledge.

For decays of the cascade D's produced in B decays, the LUND decay tables for D mesons are tuned in order to match data from MARK-III [49]. The main concern

for a vertexing analysis is the charged particle multiplicity distributions [50] which determine the visibility of the D vertex. The matching to these distributions is shown in figure B.7.

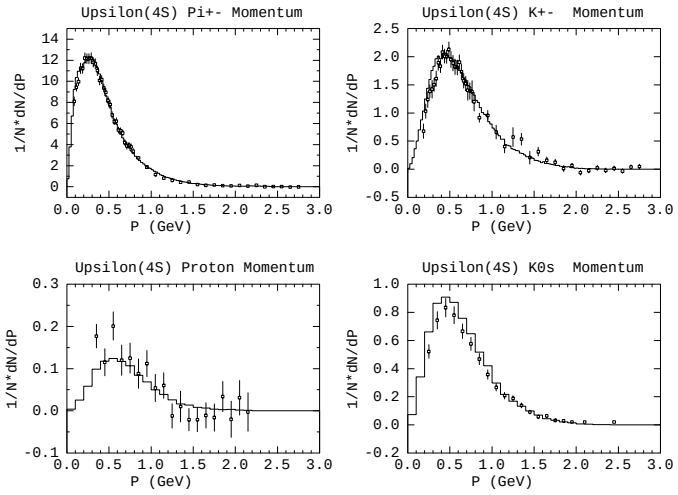

Figure B.5: B decay $\pi^{\pm}$, $K^{\pm}$, $p^{\pm}$, and K_s momentum distributions. The SLD MC histogram is compared with ARGUS data points.

B.4 Definition of the decay categories

To interpret the results of the charm counting analysis, the following assumptions must be examined. While the three topological categories have a physical interpretation, they are actually defined for the purposes of the analysis by the decay modes produced in the SLD B decay MC. The default composition of B hadrons produced is 41% B_u, 41% B_d, 11% B_s, and 7% b baryons but these are reweighted to the world averages as described in chapter 9. The decay categories are defined using the

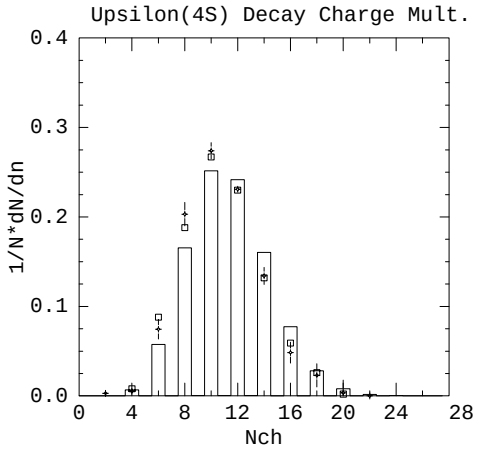

Figure B.6: B decay charged track multiplicity. The SLD MC histogram is compared with data from ARGUS (boxes) and CLEO (data points).

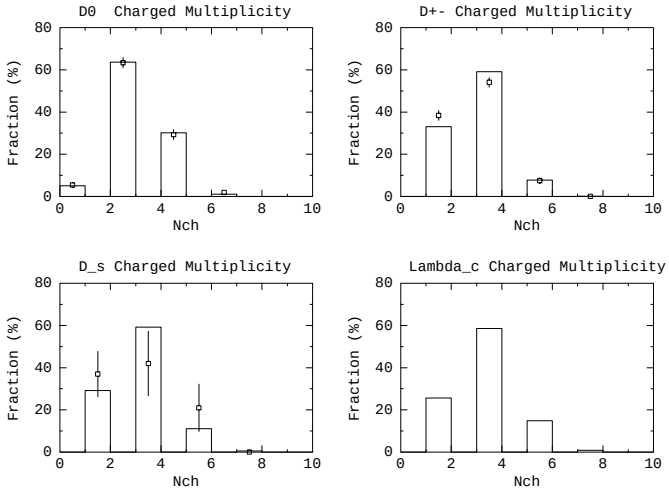

Figure B.7: Charm hadron decay charged track multiplicity. The SLD MC histogram is compared with MARK-III data points. No data exists for the Λ_c decay multiplicity.

reweighted mixture of B hadrons and the modelled decays of each hadron type. For the B meson contributions, the CLEO-based decay modelling is described in more detail below. For the b-baryon contribution, the LUND modelling produces primarily ($\sim$ 75%) correct-sign c-baryons in $1D$ decays although small fractions of the other decay types are also produced. Variations of the following definitions are discussed in chapter 9.

$0D$ decays are defined to be those decays which only produce a B vertex and no D vertices. It is assumed that these decays may be modelled rather generically using just about any decay model as long as a reasonable number of daughter particles are produced. In the analysis, the $0D$ topologies are modelled using decays to charmonia resonances. A LUND $b \to u$ quark decay model and a $b \to sg$ model [12] are used to evaluate systematic uncertainties due to differences in kinematics.

$1D$ decays are defined using the MC modelled decays of B hadrons to D^0, $D^{\pm}$, D_s, and c-baryons shown in table B.1. The meson decays are generated using tabulated measured modes including the Isgur-Wise model for semileptonic decays. Also, the inclusive decay models described above contribute to reproduce the measured B decay kinematics. A large fraction of the c-baryon modes in this category are produced by the LUND-generated decays of b-baryons. The MC default charm hadron composition for $1D$ decays is 56.6% D^0, 19.3% $D^{\pm}$, 9.4% D_s, and 14.8% c baryons.

The $2D$ decays are defined using the tabulated modes indicated in table B.2 in which a rough categorization has been used. Further details are given for the specific example of B^- decays in tables B.3, B.4, B.5, and B.6. Appropriate charge conjugation and strong isospin rotations of the daughter particles can be used to derive

the corresponding tables for the other B mesons. The listed branching fractions are based on the CLEO decay tables which have been tuned to various measurements by CLEO.

Wrong sign D_s production is the main source of D_s in B decays. The decay table (tables B.3 and B.4) has been tuned by CLEO to match to the measured D_s momentum spectrum [32] as shown in figure B.3. Both upper vertex and lower vertex D_s production are included. As discussed in chapter 9, for the current analysis, the n-body decays are reweighted to higher x_{D_s} from the default MC to better reproduce the measured spectrum.

The upper vertex production of non-strange D mesons is modelled using measurements of $BR(B \to D^{(*)}D^{(*)}K)$ based on exclusive reconstructions [38]. These measurements, which favor production of vector mesons over scalar mesons, are tabulated in table B.5. Because the sum of the measured modes does not exhaust the inclusive wrong-sign D branching ratio [39], additional modes producing $K^{(*)}$ are also included in the decay table. The measured upper vertex D^0 and $D^{\pm}$ momentum spectrum is well-modelled by assuming generic three-body phase space for all of these decays so no extra assumptions about the decay matrix elements are necessary. In addition, a small contribution from $W \to (\bar{c}d)$ processes is modelled based on the results reported in [51]. These modes are shown in table B.6. The cumulative branching fraction into all of these modes agrees with the world average of measurements of the wrong-sign D^0 and $D^{\pm}$ production rate [11].

Wrong sign charmed baryon production in B meson decays is expected to be a small effect ($BR(B \to \Lambda_c^+ X) = 0.008 \pm 0.006$ [52]) and is not modelled. Even in the

B Decay Model composition

Category	Decay mode	default BR	reweighted BR
$1D$	BR($B \to D^0$ X)	0.452	0.443
$1D$	BR($B \to D^{\pm}$ X)	0.154	0.151
$1D$	BR($B \to D_s$ X)	0.075	0.072
$2D$	BR($B \to D\ \bar{D}$ X)	0.178	0.173
$1D$	BR($B \to c$ baryon X)	0.118	0.137
$0D$	BR($B \to (c\bar{c})$ X)	0.023	0.023

Table B.1: Inclusive mode composition of the SLD B decay MC. The default composition of the B hadrons is 41% B_u, 41% B_d, 11% B_s, and 7% b baryons. These are reweighted to the world averages of 39.7% B_u, 39.7% B_d, 10.5% B_s, and 10.1% b baryons in order to get the reweighted branching ratios (BR) into each decay mode. The D composition of the $2D$ modes is listed in table B.2.

LUND b-baryon decay modelling, $W^- \to \bar{c}s$ processes primarily yield wrong sign D mesons rather than baryons.

B meson → 2D composition (broad categories)

Mode type	Daughter particles	BR
upper vertex D_s	${D_s}^{(*)}D^{(*)}$	0.0552
	${D_s}^{(*)}D^{(*)}\pi$	0.0246
	${D_s}^{(*)}D^{(*)}\pi\pi$	0.0202
lower vertex D_s	${D_s}^{(*)}{D_s}^{(*)}K$	0.0008
	${D_s}^{(*)}{D_s}^{(*)}K\pi$	0.0004
$W \to (\bar{c}s)$, no D_s	$D^{(*)}D^{(*)}K^{(*)}$	0.0800
$W \to (\bar{c}d)$, no D_s	$D^{(*)}D^{(*)}$	0.0040
	$D^{(*)}D^{(*)}\pi$	0.0012
	$D^{(*)}D^{(*)}\pi\pi$	0.0008

Table B.2: Tabulated B meson $\to 2D$ branching fractions. To avoid an abundance of notation, the charges and anti-particle notations have been omitted. Each entry is to be read as the sum over all possible spin, charge, and particle-antiparticle configurations. For example, for $B^0 \to D^{(*)}D^{(*)}K^{(*)}$, there are 2 charge configurations corresponding to the 2 non-degenerate places the neutral charge could be placed. This should be multiplied by the number of possible spin configurations: 1 (no vector mesons) + 3 (one vector meson) + 3 (two vector mesons) + 1 (three vector mesons), which gives the 16 different tabulated modes in table B.5.

B^- meson → 2D composition (upper vertex D_s)

BR	Daughter particles
0.0110	$D_s^- D^0$
0.0112	$D_s^- D^{*0}$
0.0089	$D_s^{*-} D^0$
0.0241	$D_s^{*-} D^{*0}$
0.0082	$D_s^- D^+ \pi^-$
0.0041	$D_s^- D^0 \pi^0$
0.0082	$D_s^{*-} D^+ \pi^-$
0.0041	$D_s^{*-} D^0 \pi^0$
0.0045	$D_s^- D^+ \pi^- \pi^0$
0.0045	$D_s^- D^0 \pi^- \pi^+$
0.0011	$D_s^- D^0 \pi^0 \pi^0$
0.0045	$D_s^{*-} D^+ \pi^- \pi^0$
0.0045	$D_s^{*-} D^0 \pi^- \pi^+$
0.0011	$D_s^{*-} D^0 \pi^0 \pi^0$

Table B.3: Tabulated decay modes for upper vertex production of D_s in B^- decays.

B^- meson → 2D composition (lower vertex D_s)

BR	Daughter particles
0.0002	$D_s^+ K^- D_s^-$
0.0002	$D_s^+ K^- D_s^{*-}$
0.0002	$D_s^+ K^- D_s^- \pi^0$
0.0002	$D_S^{*+} K^- D_s^-$
0.0002	$D_S^{*+} K^- D_s^{*-}$
0.0002	$D_S^{*+} K^- D_s^- \pi^0$

Table B.4: Tabulated decay modes for color-suppressed lower vertex production of D_s in B^- decays.

B^- meson → 2D composition ($W^- \to \bar{c}s$, no D_s)

BR	Daughter particles
0.0025	$D^0 D^0 K^-$
0.0025	$D^0 D^- \bar{K}^0$
0.0025	$D^0 \bar{D}^0 K^{*-}$
0.0025	$D^0 D^- \bar{K}^{*0}$
0.0050	$D^{*0} \bar{D}^0 K^-$
0.0050	$D^{*0} D^- \bar{K}^0$
0.0050	$D^0 \bar{D}^{*0} K^-$
0.0050	$D^0 D^{*-} \bar{K}^0$
0.0025	$D^{*0} \bar{D}^0 K^{*-}$
0.0025	$D^{*0} D^- \bar{K}^{*0}$
0.0025	$D^0 \bar{D}^{*0} K^{*-}$
0.0025	$D^0 D^{*-} \bar{K}^{*0}$
0.0150	$D^{*0} \bar{D}^{*0} K^-$
0.0150	$D^{*0} D^{*-} \bar{K}^0$
0.0050	$D^{*0} \bar{D}^{*0} K^{*-}$
0.0050	$D^{*0} D^{*-} \bar{K}^{*0}$

Table B.5: Tabulated decay modes for upper vertex production of $\bar{D}^0$ and D^- in B^- decays.

B^- meson $\rightarrow$ 2D composition ($W^- \rightarrow \bar{c}d$)

BR	Daughter particles
0.0010	$D^- D^0$
0.0010	$D^- D^{*0}$
0.0010	$D^{*-} D^0$
0.0010	$D^{*-} D^{*0}$
0.0004	$D^- D^+ \pi^-$
0.0002	$D^- D^0 \pi^0$
0.0004	$D^{*-} D^+ \pi^-$
0.0002	$D^{*-} D^0 \pi^0$
0.0003	$D^- D^+ \pi^- \pi^0$
0.0002	$D^- D^0 \pi^0 \pi^0$
0.0003	$D^- D^0 \pi^- \pi^+$

Table B.6: Tabulated decay modes for $W^- \rightarrow \bar{c}d$ processes in B^- decays.

Appendix C

CDC Track Reconstruction

C.1 Pattern Recognition

To reconstruct the trajectories of charged particles traversing the CDC, the discrete set of hits left by the particles must be grouped together to form helices with helix axes parallel to z. The helix curvature then gives a measurement of the particle momentum. The reconstructed helices are referred to as 'tracks.' To simplify the task, the $\sim$8 hits in each drift cell are first grouped together and fit to straight lines. These groupings are referred to as 'vector hits' because they approximate tangent vectors to the circular $R\phi$ projection of the track helix. Because of the stereo angle, the $R\phi$ positions and directions of vector hits in stereo superlayers are both functions of the assumed z position of the vector hit. Also, the electric fields about each anode wire have a two-fold symmetry, so a drift time measurement could correspond to an ionization signal on either side of the wire. Therefore, each vector hit has a partner

which is its image mirrored across the local anode plane.

In the next step, VXD3 vectors are also formed from 3 hit combinations in the vertex detector. These vectors are similar to axial vector hits since they give unambiguous measurements of the helix tangent vectors in $R\phi$. They also provide a precise measurement of the dip angle for each helix:

$$\tan\lambda \equiv \frac{dz}{ds_t} \tag{C.1}$$

where s_t is the transverse projection of the arclength s along the helix. For the typically large radii of curvature in the SLD magnetic field, s_t may be safely approximated as the distance along the radial cylindrical coordinate R. The $\tan\lambda$ measurement gives very precise information on the expected z position of the extrapolated track, and it can be used to constrain the expected z positions of the stereo hits, as will be shown shortly.

The set of VXD3 vectors is grouped together with the axial vectors, and from this set, primitive circles are formed. The criterion for adding a vector hit to a circle is of course that it is consistent with being a tangent vector to that candidate circle. For example, for a combination of two vector hits, the two positions and one tangent vector define a circle. The second tangent vector can now be required to be consistent with the hypothesized circle. The list of all two-vector-hit combinations may now be sorted to provide 5-vector-hit combinations in which all vector hits are pairwise consistent.

At this stage, the track measurement is basically done. The curvature is measured

by the combination of 4 axial vector hits + 1 VXD3 vector, and the dip angle is measured by the VXD3 vector. To get further precision, stereo vector hits may be added to each circle by shifting them in z to the positions predicted by the extrapolated VXD3 vector and then checking if they are consistent with being tangent vectors to the circle. Ideal combinations of 11 layers = 10 vector hits + 1 VXD3 vector may thus be formed.

After the 11-layer combinations are formed, their vector hits and image vector hits are removed from consideration, and a search begins for 10-layer hits, 9-layer hits, etc.... The only qualitative difference is that if a VXD3 vector is not associated with a given primitive axial vector circle, then a priori, the stereo hits are not constrained in z. The stereo vector hits are allowed to move around freely until they are consistent with the circle, but in doing so, they acquire definite z positions. The z positions of the set of stereo vector hits attached to the circle can then be fit to a line in $R - z$ to ensure that they are consistent with being from the same helix. For three or more stereo vectors, the χ^2 from the linear fit is used as a criterion to select good combinations.

C.2 The track fit

The tracks produced by the pattern recognition algorithm must then be fit to a realistic model of particle propagation, including multiple Coulomb scattering and energy loss. In order to produce a track error matrix close to the interaction region, the fit proceeds from the outermost CDC hit inwards. To fit a track, the track's second

order equation of motion is integrated using as initial conditions the outermost CDC hit position, and the momentum vector derived from the pattern recognition helix. The track is swum to its point of closest approach (POCA) to the next wire layer, and a search begins for nearby hits. The hit most consistent with the track is added, and the track parameters are recalculated for the next integration. Possible Coulomb scatters are incorporated as uncertainties in the track error matrix. The procedure continues inwards all the way to the innermost VXD3 layer. The fitted track is then swum to its POCA to the IP, at which point, the track parameters and error matrix are saved for use in physics analyses.

Bibliography

[1] A. F. Falk, Z. Ligeti, M. Neubert, and Y. Nir, "Heavy quark expansion for the inclusive decay anti-B → tau anti-neutrino X," *Phys. Lett.* **B326** (1994) 145–153, hep-ph/9401226.

[2] V. Barger and R. J. N. Phillips, *Collider Physics*, vol. 71 of *Frontiers in Physics*, p. 82. Addison-Wesley, Redwood City, USA, 1987.

[3] G. Buchalla, I. Dunietz, and H. Yamamoto, "Hadronization of b → c anti-c s," *Phys. Lett.* **B364** (1995) 188–194, hep-ph/9507437.

[4] I. I. Y. Bigi, B. Blok, M. A. Shifman, and A. Vainshtein, "The Baffling semileptonic branching ratio of B mesons," *Phys. Lett.* **B323** (1994) 408–416, hep-ph/9311339.

[5] **CLEO** Collaboration, B. Barish *et al.*, "Measurements of the B semileptonic branching fraction with lepton tags," *Phys. Rev. Lett.* **76** (1996) 1570–1574.

[6] M. Battaglia, "Experimental status of semileptonic B decays: Recent results from LEP and comparisons with Upsilon(4S) experiments," *Nucl. Phys. Proc. Suppl.* **96** (2001) 443–452, hep-ex/0009026.

[7] M. Neubert and C. T. Sachrajda, "Spectator effects in inclusive decays of beauty hadrons," *Nucl. Phys.* **B483** (1997) 339–370, hep-ph/9603202.

[8] E. Bagan, P. Ball, V. M. Braun, and P. Gosdzinsky, "Theoretical update of the semileptonic branching ratio of B mesons," *Phys. Lett.* **B342** (1995) 362–368, hep-ph/9409440. Erratum-ibid.B374:363-364,1996.

[9] E. Bagan, P. Ball, B. Fiol, and P. Gosdzinsky, "Next-to-leading order radiative corrections to the decay $b \to c\bar{c}s$," *Phys. Lett.* **B351** (1995) 546–554, hep-ph/9502338.

[10] H. Yamamoto, "Charm counting and B semileptonic branching fraction," hep-ph/9912308.

[11] ALEPH, CDF, DELPHI, L3, OPAL, SLD, "Combined results on b-hadron production rates and decay properties," CERN-EP/2001-050.

[12] A. L. Kagan and J. Rathsman, "Hints for enhanced $b \to sg$ from charm and kaon counting," hep-ph/9701300.

[13] **DELPHI** Collaboration, P. Abreu *et al.*, "Measurement of the inclusive charmless and double-charm B branching ratios," *Phys. Lett.* **B426** (1998) 193–206.

[14] I. Dunietz, J. Incandela, F. D. Snider, and H. Yamamoto, "Large charmless yield in B decays and inclusive B decay puzzles," *Eur. Phys. J.* **C1** (1998) 211–219, hep-ph/9612421.

[15] **CLEO** Collaboration, L. Gibbons *et al.*, "The inclusive decays $B \to DX$ and $B \to D^*X$," *Phys. Rev.* **D56** (1997) 3783–3802, hep-ex/9703006.

[16] N. Phinney, "Review of SLC performance,". Invited talk given at 15th Inst. Conf. on High Energy Accelerators (HEACC '92), Hamburg, Germany, Jul 20-24, 1992, and at 16th Int. Linac Conf. (LINAC '92), Ottawa, Canada, Aug 24-28, 1992, and at 26th Int. Conf. on High Energy Physics (ICHEP92), Dallas, TX, Aug 6-12, 1992.

[17] K. Abe *et al.*, "Design and performance of the SLD vertex detector, a 307 Mpixel tracking system," *Nucl. Instrum. Meth.* **A400** (1997) 287–343.

[18] M. D. Hildreth *et al.*, "Performance of the SLD central drift chamber," *IEEE Trans. Nucl. Sci.* **42** (1995) 451.

[19] M. J. Fero *et al.*, "Performance of the SLD central drift chamber," *Nucl. Instrum. Meth.* **A367** (1995) 111–114.

[20] D. Axen *et al.*, "The Lead liquid argon sampling calorimeter of the SLD detector," *Nucl. Instrum. Meth.* **A328** (1993) 472–494.

[21] A. C. Benvenuti *et al.*, "The Iron Calorimeter and Muon Identifier For SLD," *Nucl. Instr. Meth.* **A276** (1989) 94.

[22] D. Dong, "Measurement of the b quark fragmentation function in Z0 decays,". SLAC-R-550.

[23] J. A. Quigley, "A Measurement of the Tau Michel Parameters at SLD,". SLAC-R-0506.

[24] D. J. Jackson, "A topological vertex reconstruction algorithm for hadronic jets," *Nucl. Instrum. Meth.* **A388** (1997) 247–253.

[25] **SLD** Collaboration, K. Abe *et al.*, "Time dependent B/s0 - anti-B/s0 mixing using inclusive and semileptonic B decays at SLD," `hep-ex/0012043`.

[26] **SLD** Collaboration, T. Wright *et al.*, "Z quark coupling measurements at SLD,". Presented at the Meeting of the Division of Particles and Fields of the American Physical Society, Columbus, Ohio, August 9-12, 2000. SLAC-PUB-8721.

[27] N. de Groot, "Electroweak results from SLD," `hep-ex/0105058`.

[28] **SLD** Collaboration, K. Abe *et al.*, "Direct measurement of A(b) at the Z0 pole using a lepton tag," `hep-ex/0009064`.

[29] **SLD** Collaboration, K. Abe *et al.*, "Precise measurement of the b-quark fragmentation function in Z0 boson decays," *Phys. Rev. Lett.* **84** (2000) 4300–4304, `hep-ex/9912058`.

[30] **SLD** Collaboration, K. Abe *et al.*, "Improved measurement of the b quark fragmentation function in Z0 decays,". Contributed to 30th International Conference on High-Energy Physics (ICHEP 2000), Osaka, Japan, 27 Jul - 2 Aug 2000.

[31] The LEP Electroweak Working Group, "Presentation of LEP Electroweak Heavy Flavour Results for Summer 1996 Conferences," LEPHF/96-01, http://www.cern.ch/LEPEWWG/heavy/lephf9601.ps.gz.

[32] **CLEO** Collaboration, D. Gibaut *et al.*, "Measurements of B $\rightarrow$ D(s)+ X decays," *Phys. Rev.* **D53** (1996) 4734–4746.

[33] M. M. Zoeller, "Inclusive charmed baryon lambda(c)+ and sigma(c) production in B meson decays,". UMI-94-19745.

[34] The LEP Heavy Flavour Group, "Input Parameters for the LEP/SLD Electroweak Heavy Flavour Results for Summer 1998 Conferences," LEPHF/98-01, http://www.cern.ch/LEPEWWG/heavy/lephf9801.ps.gz.

[35] T. Sjostrand, "PYTHIA 5.7 and JETSET 7.4 physics and manual,". CERN Geneva - TH. 7112 (94/02,rec.Mar.) 310 p. and e: CERN th-7112-93.

[36] **CLEO** Collaboration, G. Crawford *et al.*, "Measurement of baryon production in B meson decay," *Phys. Rev.* **D45** (1992) 752–770.

[37] **ALEPH** Collaboration, R. Barate *et al.*, "Measurements of BR(b –¿ tau- anti-nu/tau X) and BR(b –¿ tau- anti-nu/tau D*+- X) and upper limits on BR(B- –¿ tau- anti-nu/tau) and BR(b –¿ s nu anti-nu)," *Eur. Phys. J.* **C19** (2001) 213–227, `hep-ex/0010022`.

[38] CLEO Collaboration, "Exclusive Reconstruction of $\bar{B} \to D^{(*)}\bar{D}^{(*)}K^{-}$," CLEO CONF 97-26.

[39] **CLEO** Collaboration, T. E. Coan *et al.*, "Flavor-specific inclusive B decays to charm," *Phys. Rev. Lett.* **80** (1998) 1150–1155, `hep-ex/9710028`.

[40] **OPAL** Collaboration, R. Akers *et al.*, "A Measurement of charged particle multiplicity in Z0 → c anti-c and Z0 → b anti-b events," *Phys. Lett.* **B352** (1995) 176–186.

[41] A. Trandafir, "Measurement of inclusive b semileptonic branching fractions at the Z resonance,". SLAC-R-558.

[42] **ALEPH** Collaboration, R. Barate *et al.*, "Observation of doubly-charmed B decays at LEP," *Eur. Phys. J.* **C4** (1998) 387–407.

[43] CLEO Collaboration, "QQ - The CLEO Event Generator," http://www.lns.cornell.edu/public/CLEO/soft/QQ.

[44] N. Isgur and M. B. Wise, "Weak Decays of Heavy Mesons in the Static Quark Approximation," *Phys. Lett.* **B232** (1989) 113.

[45] N. Isgur and M. B. Wise, "Weak Transition Form-factors Between Heavy Mesons," *Phys. Lett.* **B237** (1990) 527.

[46] **CLEO** Collaboration, M. Artuso *et al.*, "Study of the B0 semileptonic decay spectrum at the Upsilon(4S) resonance," *Phys. Lett.* **B399** (1997) 321–328, hep-ex/9702007.

[47] **ARGUS** Collaboration, H. Albrecht *et al.*, "Inclusive Production of Charged Pions, Charged and Neutral Kaons and Anti-protons in e+ e- Annihilation at 10-GeV and in Direct Upsilon Decays," *Z. Phys.* **C44** (1989) 547.

[48] **CLEO** Collaboration, G. Brandenburg *et al.*, "Charged track multiplicity in B meson decay," *Phys. Rev.* **D61** (2000) 072002, hep-ex/9907057.

[49] B. Nemati, "The Inclusive decay properties of charmed mesons,". RX-1302 (WASHINGTON).

[50] **MARK-III** Collaboration, D. Coffman *et al.*, "Measurement of the inclusive decay properties of charmed mesons," *Phys. Lett.* **B263** (1991) 135–140.

[51] **CLEO** Collaboration, E. Lipeles *et al.*, "Study of the decays $B^0 \to D^{(*)+} D^{(*)-}$," *Phys. Rev.* **D62** (2000) 032005, hep-ex/0002065.

[52] **CLEO** Collaboration, R. Ammar *et al.*, "Study of flavor-tagged baryon production in B decay," *Phys. Rev.* **D55** (1997) 13–18.